THE HONG KONG
POLYTECHNIC UNIVERSITY
香港理工大學
Pao Yue-kong Library
包玉剛圖書館

Copyright Undertaking

This thesis is protected by copyright, with all rights reserved.

By reading and using the thesis, the reader understands and agrees to the following terms:

1. The reader will abide by the rules and legal ordinances governing copyright regarding the use of the thesis.
2. The reader will use the thesis for the purpose of research or private study only and not for distribution or further reproduction or any other purpose.
3. The reader agrees to indemnify and hold the University harmless from and against any loss, damage, cost, liability or expenses arising from copyright infringement or unauthorized usage.

IMPORTANT

If you have reasons to believe that any materials in this thesis are deemed not suitable to be distributed in this form, or a copyright owner having difficulty with the material being included in our database, please contact lbsys@polyu.edu.hk providing details. The Library will look into your claim and consider taking remedial action upon receipt of the written requests.

Pao Yue-kong Library, The Hong Kong Polytechnic University, Hung Hom, Kowloon, Hong Kong

http://www.lib.polyu.edu.hk

DISTRIBUTED DYNAMIC OPTICAL FIBER SENSING SYSTEMS BASED ON LIGHT SCATTERING TECHNIQUES

JIN CHAO

PhD

The Hong Kong Polytechnic University

2019

The Hong Kong Polytechnic University
Department of Electronic and Information Engineering

DISTRIBUTED DYNAMIC OPTICAL FIBER SENSING SYSTEMS BASED ON LIGHT SCATTERING TECHNIQUES

JIN CHAO

A thesis submitted in partial fulfillment of the requirements for the
degree of Doctor of Philosophy

April 2019

Certificate of Originality

I hereby declare that this thesis is my own work and that, to the best of my knowledge and belief, it reproduces no material previously published or written, nor material that has been accepted for the award of any other degree or diploma, except where due acknowledgement has been made in the text.

………………………………………………. (Signed)

金超

………………………………………………. (Name of student)

Dedicated

To my Families

Abstract

Distributed optical fiber sensing (DOFS) techniques provide many unique advantages comparing with other alternative sensing techniques and have found many applications in different application areas. Majority of the research effort has been on the measurement of quasi-static process like temperature variation or applied strain at the beginning. In recent decades, the dynamic optical sensor techniques have developed rapidly for the purpose of providing dynamic information of non-static scenarios involving pipeline security monitoring, infrastructure health monitoring, etc. Motivated by demands for lower respond time applications, several advanced distributed fiber-optic sensing schemes for such dynamic measurements have been proposed and investigated. This thesis focuses on the studies of systems based on various kind of optical scatterings including the Rayleigh scattering based phase-sensitive optical time domain reflectometer (OTDR) system and Brillouin scattering based Brillouin optical time domain analysis (BOTDA) system.

First, an integrated telecommunication system and phase sensitive-OTDR sensing system with shared optical bandwidth is studied. The incorporation of the sensing system into the communication system can potentially ensure the reliable operation of a communication system by detecting events that may result in disruption to the operation of a communication link. Optical Orthogonal Frequency Division Multiplexing (OFDM) modulation technique is used in modern telecommunication networks. In the proposed system, 16QAM-OFDM signal at 112Gbit/s data rate is transmitted over 20km single mode fiber (SSMF). Meanwhile, distributed phase sensitive-OTDR system is deployed to monitor the environmental vibration along the fiber. Experimental results show that about

1 dB optical signal-to-noise ratio (OSNR) penalty of bit-error-rate (BER) performance is observed in the communication link through the incorporation of the sensing signal. On the other hand, the influence of communication signal on sensing system is almost negligible as the power reflected by OFDM signal is extremely weak (more than 30 dBm lower than reflected phase-OTDR signal). 20 m spatial resolution with SNR of location information as high as 8.4 dB is obtained with 20 km fiber length. Detection of 1kHz vibration applied by Piezo-ceramic transducers (PZT) is successfully demonstrated.

In addition, a digitally generated optical frequency comb is proposed to realize ultra-fine and fast optical spectral analysis without frequency scanning and thus can be potentially used to realize a fast BOTDA. A fast BOTDA based on the digital optical frequency comb (DOFC) has been studied, which can locate the Brillouin frequency shift (BFS) without frequency scanning. The scanning-free BOTDA system has been demonstrated experimentally with 51m spatial resolution over 10km standard single mode fiber. The resolution and range are 1.5°C and 30°C for temperature measurement respectively. The resolution and range are 43.3με and 900με for strain measurement respectively.

Finally, a single-measurement BOTDA based on coherent detection of the phase of DOFC probe signal without any averaging and frequency scanning process is investigated. The phase shift of each frequency component of DOFC probe, after transmitting through the fiber under test (FUT) is directly mapped by coherent demodulation in a single data acquisition without any averaging, leading to a sensing speed only limited by the sensing range. Compared with the previous techniques proposed, the measurement time is reduced by eliminating the need for averaging. Brillouin phase shift (BPS) detection instead of Brillouin gain spectrum (BGS) has enabled better measurement accuracy. The performance of our scheme is analyzed through simulation and experiment. Distributed temperature

sensing over 10km FUT has been demonstrated by using the proposed single-measurement BOTDA with a BFS uncertainty of 1.5 MHz and spatial resolution of 51.2 m. With the advantage of high speed offered by the proposed scheme, dynamic measurement up to 1 kHz vibration frequency has been demonstrated.

Acknowledgements

Until now, I realize that I am going to reach the destination of my study. Hereby, I want to thank a number of people during my Ph.D. studies. First, I am deeply indebted to Prof. LU Chao. He not only provided me the opportunity to join his group at the Hong Kong Polytechnic University, but also gave me patient guidance and continuous support on my research.

I am greatly indebted to Prof. Hwa-Yaw TAM and his research group members, including Dr. Wenghong CHUNG, Dr. Zhenyong LIU, and Dr. Jie WANG, with whom I worked during my doctoral studies. I am also very thankful for their generous help, valuable advice, and patiently supports. Without their contribution, the work in this thesis could not be completed.

Especially, I want to thank Dr. Yuan MAO, Dr. Dong Zhenhua, Dr. Liqing Gan, Dr. Nan Guo, Dr. Kuanglu YU, Dr. Yuliang GAO, Dr. Jie LIU, Dr. Kangping ZHONG, Dr. Zhe KANG, Dr. Faisal Nadeem KHAN, Dr. Liang WANG, Dr. Abul Kalam AZAD, Dr. Huan WU, Dr. Tao GUI, Mr. Fengze Tan, and Mr. Biwei WANG. They offered me numerous practical and constructive suggestions, indeed, which contributed a lot to my studies. My thanks are also extended to other colleagues at the Photonics Research Centre and Department of Electronic and Information Engineering. I am also appreciative of the support from the staffs of the Department and the Research Office.

I would also want to thank my teammates from Polytechnic university soccer team. Especially Dr. Yang Liu, Dr. Linbin Yang, Dr. Yanjie Bao, Dr. TianTian He, Dr. Peng Xue, Dr. Junwei Liu, Mr Haobin Wu, Mr Zhonglei Gu, and Mr. Xueyuan Shui. With them, I have enjoyed pleasant soccer time and established friendships.

Finally, I can never thank enough my beloved parents for their unwavering love best wishes and encouragement. The support from my family have encouraged me overcome all the difficulties faced in the past, present and future.

March, 2019

Contents

List of abbreviations

A		
	AOM	Acoustic optical modulator
	ASE	Amplified spontaneous emission
	AWG	Arbitrary waveform generator
	AWGN	Additive white Gaussian noise
B		
	BER	Bit-error-rate
	BFS	Brillouin frequency shift
	BGS	Brillouin gain spectrum
	BPS	Brillouin phase-shift spectrum
	BOTDA	Brillouin optical time domain analysis
	BOTDR	Brillouin optical time domain reflectometry
C		
	CP	Cyclic prefix
	CW	Continuous-wave
D		
	DAS	Distributed acoustic sensing
	DC	Direct current
	DEFC	Digital electrical frequency comb
	DFB	Distributed feedback laser
	DOFC	Digital optical frequency comb
	DOFS	Distributed optical fiber sensing
	DSP	Digital signal processing
E		
	EDFA	Erbium-doped fiber amplifier
	EM	Electromagnetic
	EMI	Electromagnetic interference
	EOM	Electro-optic modulator
	ER	Extinction ratio
F		
	FBG	Fiber Bragg grating

	F-BOTDA	Fast- Brillouin optical time domain analysis
	FFT	Fast Fourier transform
	FUT	Fiber under test
	FWHM	Full-width at half-maximum
G		
	GI	Guard Interval
	GVD	Group-velocity dispersion
I		
	IF	Intermediate frequency
	IFFT	Inverse fast Fourier transform
	IM	intensity modulator
	ISI	Inter-symbol interference
L		
	LCF	Lorentzian curve fitting
	LC-FBG	linearly chirped fiber Bragg grating
	LMSCF	least mean square curving fitting
	LO	Local oscillator
M		
	MI	Modulation instability
	MZI	Mach–Zehnder interferometer
	MZM	Mach–Zehnder modulator
O		
	OFDM	Orthogonal frequency division multiplexing
	OFS	Optical fiber sensor
	OSC	Oscilloscope
	OSNR	Optical signal-to-noise ratio
	OTDR	Optical time domain reflectometry
P		
	PAPR	Peak-to-average power ratio
	PBS	Polarizing beam splitter
	PBC	Polarizing beam combiner
	PC	Polarization controller
	PD	Photonic detector
	PZT	Piezo-ceramic transducer
R		
	RF	Radio frequency
	RS	Rayleigh scattering

S

SA-BOTDA	Slope-assisted Brillouin optical time domain analysis
SBS	Stimulated Brillouin scattering
SF-BOTDA	Sweep-free Brillouin optical time domain analysis
SPM	Self-phase modulation
SSMF	Standard single-mode fiber
SNR	Signal-to-noise ratio
SOP	State of polarization

List of major notations

$\boldsymbol{V}$	Volume of medium
$\boldsymbol{E}$	Electric field of optical wave
c	Velocity of light in vacuum
μ_0	Vacuum magnetic permeability
$\boldsymbol{P}$	Polarization field of medium
ε_0	Dielectric vacuum constant or Vacuum permittivity
ε	Dielectric tensor of medium
χ	Dielectric susceptibility or Electric susceptibility
ρ	Density of medium
T	Temperature
γ_e	Electrostrictive coefficient
p	Pressure inside of medium
Γ'	Acoustic damping parameter
υ_A	Acoustic velocity in medium
C	Compressibility of medium
K	Bulk modulus of medium
η_s, η_b	Shear and bulk viscosity coefficients of medium
κ	Thermal conductivity of medium
γ_a	Adiabatic index of medium
Q	Normalized amplitude of density fluctuation
q, $\mathbf{q}$	Wave number/wave vector of density fluctuation
$\boldsymbol{\Omega}$	Frequency (angular) of density fluctuation
α_A	Acoustic absorption coefficient
Γ	Phonon decay rate
τ_p	Phonon lifetime
k, $\mathbf{k}$	Wave number/wave vector of optical field

ω	Frequency (angular) of optical wave
n	Refractive index
λ	Optical wavelength
ν	Frequency of optical wave
ν_B	Brillouin frequency shift
$\Delta\nu_\mathrm{B}$	Brillouin linewidth
u	Field energy density
w	Work
p_st	Strictive pressure
$\boldsymbol{f}$	Electrostrictive force
$\boldsymbol{\Omega}_\mathrm{B}$	Brillouin frequency
$\mathbf{e}$	Normalized polarization vector of optical field
F	Space distribution of optical/acoustic wave mode in optical fiber
A	Normalized amplitude of optical field
α	Attenuation coefficient of optical fiber
γ	Nonlinear parameter of optical fiber
A_eff	Effective mode area of optical fiber
g_1, g_2	Coupling coefficients of SBS effect
$\Delta\nu$	Frequency offset between the pump and Stokes waves
P	Power of optical field
g_B	SBS gain coefficient
η_SBS	Polarization efficiency of SBS effect
g_B0	Peak value of SBS gain factor
f_A	Acoustic overlap factor of SBS effect
L_eff	Effective length of optical fiber
P_cr	Critical/Threshold power
$\mathbf{s}$	Unit SOP vector on Poincaré sphere
g_R	SRS gain coefficient
E_Y	Young’s modulus of optical fiber

ζ	Poisson’s ratio of optical fiber
C_S	Strain dependent coefficient of BFS value
C_T	Temperature dependent coefficient of BFS value
$\Delta\tau$	Pulse width
Δz	Spatial resolution
ΔT	Period of pulsed pump
L	Fiber length
υ_{g}	Group velocity
σ_ν	BFS error/uncertainty
σ	Normalized amplitude error (Normalized noise level)

List of Figures

Equation Chapter (Next) Section 1

1 Introduction

In this chapter, the development of distributed dynamic optical fiber sensing techniques is reviewed first. The techniques used in these systems including optical Rayleigh/Brillouin scattering based dynamic optical fiber sensor are discussed subsequently. Afterwards, research motivations and outlines of the thesis are given. Finally, the publications during the Ph.D. period are listed.

1.1 Overview

The principle of total internal reflection which makes optical fiber possible was first demonstrated by Daniel Colladon and Jacques Babinet in Paris in the early 1840s [1]. However, the fibers fabricated with glass at the beginning were extremely lossy with an attenuation of approximately 1000dB/km. This is mainly caused by the impurities of the materials. According to Charles K. Kao and George A. Hockham of the British company Standard Telephones and Cables (STC), the attenuation of fiber is possibly reduced to 20dB/km with high purity Silica glasses and cladded structure waveguide [2]. Following the proposed method, the loss of silica fibers was reduced dramatically [3]. Due to the significant effort by researchers around the world, attenuation of modern fibers in the wavelength region of interest has been reduced to less than 0.16dB/km and has been deployed extensively. It has formed the foundation of our modern information society [4], [5].

The availability of low-loss silica fibers launches the era of optical fiber communication and information age. Nowadays, 99% the world data traffic is transported over a global network of optical fibers. Silica fibers is not only a medium for information transmission but also a perfect instrument for sensing with its unique advantage of small size, light weight, high sensitivity, tolerance to chemical environments, and immunity to electromagnetic interference (EMI).

In recent decades, optical sensors play an increasingly important role in various aspects of modern society. The diversity of sensing requirements in different application areas has motivated the research to investigate techniques for realizing long range, distributed, high spatial resolution and high-speed optical fiber sensing systems. Up to now, the majority of optical fiber sensors (OFSs) developed can be categorized into two types:

single-point sensor or distributed sensor according to the sensing region along the fiber. For single-point sensor, typically a section of fiber is monitored with ultra-high accuracy and stability. Unlike single point OFS, distributed optical fiber sensors (DOFSs) allow for distribute measurement of external physical parameters along the sensing fiber with a given spatial resolution. Therefore, the DOFS system only need a single set of measurement devices to interrogate and provide spatially resolved information about the characteristics of measurands along the sensing fiber.

For more than two decades, the focuses in the research area have been on the static and absolute measurement including temperature and pressure monitoring. The investigation of DOFS is focused on the measurement accuracy, spatial resolution and measurement range while relatively little attention is paid to improve the measurement speed of sensing system. Among them, Rayleigh, Brillouin and Raman scattering based distributed sensing system stand out as prominent candidates for long-range quasi-static measurement tools with high accuracy, long sensing range and high spatial resolution. In recent years, researchers have gradually paid more attention to the realization of dynamic distributed sensors which is capable of monitoring vibration with fast response time. The driving force behind the trend is that in the sensing areas the measurement speed has become a more and more important parameter for various applications including pipeline security monitoring, infrastructure health monitoring, etc.

1.2 Parameters for evaluating the performance of DOFS systems

The following listed parameters are typically used to evaluate the performance of a DOFS system including measurement accuracy, sensitivity, spatial resolution, sensing range and measurement speed.

1. Measurement accuracy: represents the difference between measurement result and true value of measurand.
2. Sensitivity: express the minimum change value of measurand that can be detected by the sensing system.
3. Spatial resolution: define the minimum distance that the sensing system could indicate the transition of measurand.
4. Sensing range: maximum achieved sensing fiber length that could be measured with acceptable performance requirements (usually, spatial resolution or measurement accuracy).
5. Measurement speed: the total time needed to perform a complete sensing process.

1.3 Research objectives

The research objectives of this thesis are to investigate performance of optical scattering-based dynamic distributed DOFS system with emphasize on dynamic characteristics of different sensing schemes. Several novel optical scattering based sensing techniques are proposed and studied to improve the sensing performance. Specifically, the study aims to:

A. Study the performance of Phase sensitive-OTDR and its application

The Phase Sensitive-Optical Time Domain Reflectometer (OTDR) has been demonstrated as a suitable candidate for dynamic distributed sensing with meter-scale spatial resolution and ultra-fast responding time of several milliseconds. The limiting factor for its measurement time is limited by the fiber length and the number of traces used for averaging to improve the obtained SNR. Since there is a strong incentive to use existing fiber deployed for optical communication systems, we study the dynamic monitoring performance by constructing an integrated communication and sensing system and analyze the mutual influence between the systems. This will not only enable the use of existing optical communication link to provide additional functionality, but also enable the monitoring of optical communication links to ensure reliable operation of the communication systems. The ability of dynamic detection of vibration by Phase sensitive-OTDR system is investigate in practical application scenario.

B. Advanced DSP based modulation & de-modulation algorithm for BOTDA sensing systems and Scanning-free BOTDA system

The advanced modulation & de-modulation algorithms developed in the field of optical communications are introduced to improve the sensing speed of Brillouin-scattering based sensing systems. By using the proposed method, an optical frequency comb can be formed in a single shot and can be used as a probe signal for the sensing system. This helps to reduce the frequency scanning requirement of the probe signal and increases the sensing speed as a result. The performance of the proposed method is investigated, and a significant measurement speed improvement is observed. A digitally generated optical frequency comb is proposed to realize ultra-fine and fast optical spectral analysis without frequency scanning and thus can be potentially used to realize a fast Brillouin optical time domain analysis (BOTDA). The concept is to replace the single-tone probe signal with a digital optical frequency comb (DOFC) which can locate the BFS without frequency scanning. In this way, the sensing speed can be improved by at least two orders.

C. Single-measurement BOTDA system

Single-measurement BOTDA based on coherent detection of the phase of DOFC probe signal without any averaging and frequency scanning process has also been studied. The phase shift of each frequency component of DOFC probe, after transmitting through the FUT is directly mapped by coherent demodulation in a single data acquisition without any averaging, leading to a sensing speed only limited by the sensing range.

1.4 Organization of the thesis

This thesis contains 6 chapters.

Chapter 1 presents the backgrounds and development of dynamic DOFS techniques in general.

In chapter 2, optical scattering in fiber is discussed including the elastic scattering and inelastic scattering. The frequency spectrum as well as the scattering characteristics is presented. The transmission characteristics of the phenomenon is described in mathematical equations derived from Maxwell's equation. Then, basic principle of optical sensing system based on Rayleigh scattering phenomenon is discussed in depth together with its performance in terms of SNR, measurement accuracy and spatial resolution. After that, the operating principle of optical fiber sensing systems based on Brillouin scattering is also presented. Two types of optical sensing system based on Brillouin scattering are discussed including Brillouin optical time domain reflectometer (BOTDR) and Brillouin optical time domain analyzer (BOTDA). In particular, the operation principle of BOTDA is explained in detail with its dynamic sensing performance, obtained SNR and processing method.

In chapter 3, an integrated telecommunication system and phase sensitive -OTDR sensing system with shared optical bandwidth is investigated. Optical Orthogonal Frequency Division Multiplexing (OFDM) modulation format is selected and applied in the communication system as it is widely recognized as one of the prevailing techniques for modern optical communication networks. In our system, 16QAM-OFDM signal at 112Gbit/s is transmitted over 20km stand single mode fiber (SSMF). Meanwhile distributed phase sensitive-OTDR system is deployed to monitor the environmental change along the fiber. 20 m spatial resolution is obtained with a SNR 6.5 dB 20 km fiber length. Dynamic measurement of vibration is demonstrated successfully by applying 1KHz vibration using Piezo-ceramic transducers (PZT).

In chapter 4, the principle of scanning-free BOTDA sensor is elaborated in detail. The progress of dynamic BOTDA system is reviewed first. Then the operation principle of the proposed scanning-free BOTDA based on DOFS is discussed together with the modulation and demodulation method. Characterization of the SBS induced gain and phase shift profile based on the DOFC probe signal is presented along with the detection and DSP procedures of DOFC signal. Sensing performance of proposed system is analyzed in the last part.

In chapter 5, ultra-fast BOTDA system based on direct detection of DOFC is proposed and demonstrated experimentally. The frequency spacing and coverage bandwidth of the DOFC employed is 1.95-MHz and 2-GHz, respectively. The DOFC can be used to reconstruct the Brillouin gain spectrum (BGS) and locate the Brillouin frequency shift (BFS) without frequency scanning and thus can improve the measurement speed about 100 times compared with the conventional BOTDA. This scanning-free BOTDA system has also been demonstrated experimentally with 51.2-m spatial resolution over 10-km standard single mode fiber (SSMF) and with resolution of 1.4 ℃ for temperature and 43.3 $\mu\varepsilon$ for strain measurement.

In chapter 6, a single-measurement BOTDA based on coherent detection of the phase of DOFC probe signal without any averaging and frequency scanning process is reported. The phase shift of each frequency component of DOFC probe, after transmitting through the FUT is directly mapped by coherent demodulation in a single data acquisition without any averaging, leading to a sensing speed only limited by the sensing range.

Compared with the technique discussed in Chapter 5, the measurement time is further reduced by eliminating the need for averaging. The dynamic property of the proposed system is demonstrated with a 1kHz vibration measurement.

Finally, chapter 7 summarizes the works of this thesis, and suggests possible future works of the research area.

1.5 Publications

A number of publications arose during the course of this research work and most of which contribute to this thesis. A list of my research publications is given below.

Journal articles

1. **C. Jin**, N. Guo, Y. Feng et al., “Scanning-free BOTDA based on ultra-fine digital optical frequency comb,” Opt. Express. (2015), 23(4): 5277-5284.

2. **C. Jin**, L. Wang, Y. Chen et al., “Single-measurement digital optical frequency comb based phase-detection Brillouin optical time domain analyzer,” Opt. Express. (2017), 25(8): 9213-9224.

3. L. Wang, N. Guo, **C. Jin*** et al., “Coherent BOTDA using Phase- and Polarization-diversity Heterodyne Detection and Embedded Digital Signal Processing” IEEE Sens. J. (2017), 17(12).

4. Q. Chen, **C. Jin** et al., “A distributed fiber vibration sensor utilizing dispersion induced walk-off effect in a unidirectional Mach-Zehnder interferometer,” Opt. Express. (2013), 22(3): 2167-2173.

5. N. Guo, L. Wang, J. Wang, **C. Jin** et al., “Bi-Directional Brillouin Optical Time Domain Analyzer System for Long Range Distributed Sensing,” Sensors, 16(12), (2016).

6. N. Guo, L. Wang, H. Wu, **C. Jin** et al., “Enhanced Coherent BOTDA System without Trace Averaging,” J. Lightwave Technology, 99, (2017).

7. T. Gui, Q. Yang, X. Xiao, L. Meng, X. W. Yi, **C. Jin**, and Z. H. Li, “Auto bias control technique for optical OFDM transmitter with bias dithering,” Opt. Express, 21(5), 5833-5841 (2013).

Conference papers

1. **C. Jin**, L. Wang, Y. Chen et al., “BOTDA sensor utilizing digital optical frequency comb

based phase spectrum measurement," S2028, in the Opto-Electronics and Communications Conference, Singapore, 2017.

2. **C. Jin**, Z. Li, C. Yu et al., "Multi-dimensional Optical Information Transmission and Processing," in International Conference on Transparent Optical Networks 2017 (invited talk).

3. N. Guo, L. Wang, J. Wang, **C. Jin** et al., "Distributed sensing using Bi-Directional BOTDA System," In Proceedings of Asia Communications and Photonics Conference, Hong Kong, China, 19–23 November 2015.

4. N. Guo, L. Wang, J. Wang, **C. Jin** et al., "Coherent-detection-assisted BOTDA system without averaging using single-sideband modulated local oscillator signal," OFS100-260 (2017)

5. L. Wang, N. Guo, K. Zhong, X. Zhou, **C. Jin** et al., "Enhanced BOTDA Performance by Using Commercial Optical Coherent Receiver and Digital Signal Processor," in Asia Communications and Photonics Conference 2015, OSA Technical Digest (online) (Optical Society of America, 2015), paper ASu2A.151.

Equation Chapter (Next) Section 1

2 Scattering of light and DOFS systems based on Rayleigh and Brillouin scattering

In chapter 2, the molecular origination of optical scattering is first explained along with the qualitative description of the three typical scattering process e.g. Rayleigh scattering, Brillouin scattering and Raman scattering. After that, the wave propagation equation for each scattering process is derived from the Maxwell's Wave Equations. Then, the difference between spontaneous and simulated scattering is discussed. In the second section, the progress of dynamic distributed optical sensing system based on Rayleigh scattering highlighting the breakthroughs made in past decades is first reviewed. Then the operation principles of phase sensitive-OTDR is described along with detection and signal processing techniques for the system. Factors limiting the performance of the sensing system is analyzed in depth. In the last section, the operation principle of different kinds of Brillouin scattering based optical fiber sensors is introduced. Then the analytical model along with the SNR performance, detection accuracy and sensitivity are discussed. Finally, the parameters influencing sensing performance including spatial resolution, SNR and measurement speed are analyzed.

2.1 Spontaneous and stimulated scattering of light

2.1.1 Molecular scattering of light

The scattering of light generally arises as a result of the nonuniform physical properties of the propagation medium [6]. When propagating in the scattering medium, the optical light -as electromagnetic wave (EM) in essence, interacts with the molecular structure of the materiel through the excitation of electron cloud oscillation. Induced periodical charge by incident EM field which referred as dipole moment become a secondary radiation source. As shown in Fig. 2.1, the scattering process could happen in all directions if the physical properties of medium are inhomogeneous. Otherwise, only forward transmission direction is allowed due to the phase relationship [7].

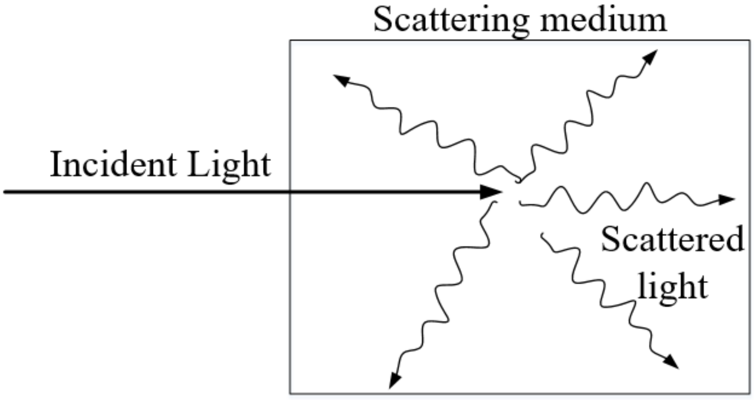

Fig. 2.1: Illustration of the scattering of incident light [7].

Optical scattering fall into two categories according to the frequency component of the backscattered light e.g. elastic scattering and non-elastic scattering. In elastic scattering, scattered photons are emitted at identical frequency with the injected light as there is no energy exchange during the process. While for non-elastic scattering, frequency shift is observed for backscattered optical light due to the energy exchange between incident light and transmitting medium. Well known examples of scattering are Rayleigh scattering, Brillouin scattering and Raman scattering.

The characteristic of frequency spectrum of scattering light is shown in Fig. 2.2. The frequency components of Rayleigh, Raman and Brillouin scattering distribute symmetrically around central line from 0 to ~13Thz. By definition, the lower frequency band is named as Stokes components while the higher counterpart is named as anti-Stokes components. Rayleigh scattering process is recognized as elastic scattering process as the frequency of backscattered photon is the same as the incident light. While the other two process are classified as non-elastic scattering phenomenon for the frequency shift induced during the scattering process.

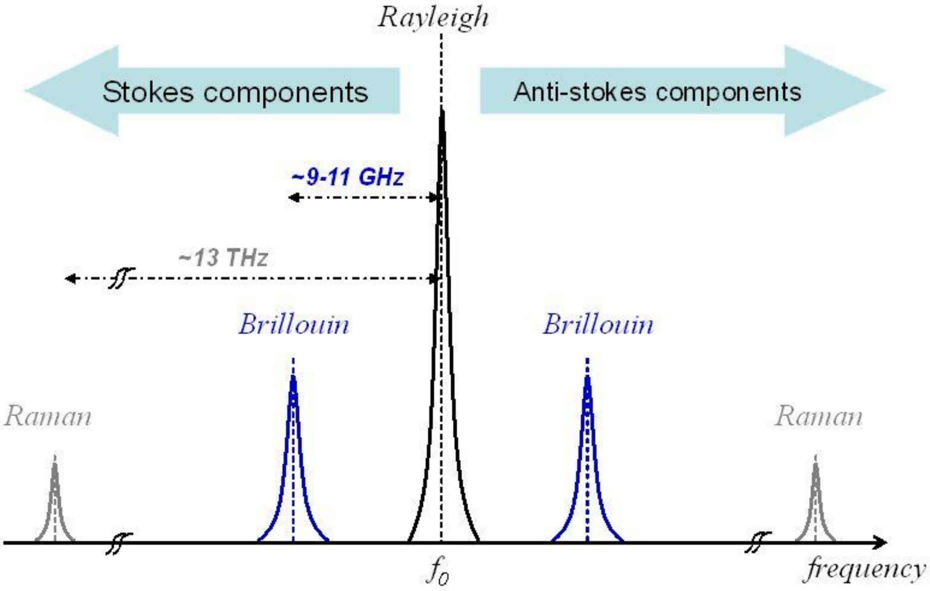

Fig. 2.2: The characteristic of frequency spectrum of spontaneous scattering light [8].

Rayleigh scattering

Rayleigh scattering is a linear process caused by local density fluctuations and resulted reflective index change. Scattered photons are emitted at identical frequency with the injected light as there is no energy exchange during the process of Rayleigh scattering, so called elastic scattering. Intensity of scattered light is proportional to ${}^{1}/_{\lambda^2}$. Where λ is the optical wavelength of the incident light.

Brillouin scattering

Spontaneous Brillouin scattering

Brillouin scattering which is predicted theoretically in the thesis by Léon Brillouin originates from light interaction with thermally excited propagating acoustic waves (or acoustical phonons) [9]. Thermally excited acoustic waves produce propagating density fluctuation along the fiber and modulate the refractive index (RI) of fiber. The incident pump light is then backscattered by moving grating and generate Stokes and anti-Stokes frequency components. Similar to Rayleigh scattering, the amount of scattering is proportional to the incident intensity.

Stimulated Brillouin scattering

A significant increase in the Brillouin scattering could be observed if the pump light intensity is further increased. As high-power incident pump could generate more intense acoustic waves due to the phenomenon of electrostriction which enhance the Brillouin scattering. In this regime the light scattering is known as ***stimulated***. As a result, this reflective index grating induced by the introduced pump signal produces back-scattered light by Bragg diffraction. As the energy and momentum conservation laws must be obeyed in the scattering process, frequency of backscattered signal is downshifted (Stokes field) as the reflective index grating is moving at the acoustic velocity.

Raman scattering

Spontaneous Raman scattering

Raman scattering is induced by the interaction between the molecular of medium and intense optical light which excite a relatively large frequency shift dependent on the resonance of molecular. The spatial vibration of molecular would scatter the incident light by several hundred to several thousand wavenumbers (cm^{-1}).

Stimulated Raman scattering

While far more intense process e.g. stimulated Raman scattering is evoked with intense incident optical light beam. During the SRS process, typically as high as 10% or more of the incident energy could be transferred to the shifted stokes and anti-stokes field.

Table 2.1 Typical values of the parameters for each scattering process [7].

Scattering process	Frequency shift $v = \omega/2\pi$ (Hz)	Linewidth $\Delta v\ (Hz)$	Gain Coefficient $g\ (MW/cm)$	Lifetime $\tau(s)$
Rayleigh	0	5×10^{-4}	10^{-5}	-
Brillouin	10^{10}	10^{8}	10^{-2}	10^{-9}
Raman	10^{13}	10^{11}	5×10^{-3}	10^{-12}

Typical value of the physical parameters for each scattering process are listed in table 2.1 which roughly represent the relative intensity of the interaction. In general, the frequency shift of Raman scattering is much larger than the remaining scattering process with a more efficient energy transfer mechanism. However, the gain of Rayleigh scattering is quite weak compared with other process with merely 10^{-5} which is about 3 orders lower than the Brillouin scattering.

2.1.2 Stimulated scattering process

The origin of optical scattering is the inhomogeneous properties of the propagation material as explained in section 2.1. Up to now, two different kinds of scattering mechanisms is investigated and applied e.g. spontaneous scattering and stimulated scattering. The scattering process is defined as spontaneous when the fluctuation of medium properties is induced by internal thermal motion or quantum chemical zero-point effects. On the other hand, the stimulated scattering featured an extra intense optical light which could excite inhomogeneities in fiber. as a result, the Stimulated light scattering is more efficient than spontaneous light scattering.

- **Physical Process**

The process of stimulated Brillouin scattering (SBS) can be modeled as a three-wave interaction among backscattered Stokes field, pump wave and acoustic photon. The pump signal excites a propagating acoustic photon through electrostriction[10]. The generated acoustic wave would propagate alone the fiber with a velocity of v_A. Meanwhile, the refractive index is changed periodically and scatter back the incident pump light. According to the Doppler shift theorem, the frequency of backscattered light is downshifted with the same frequency of v_A. The SBS process can also be regarded as a quantum-mechanically process: annihilation of a pump photon generates a Stokes photon and an acoustic phonon simultaneously. During the process both the energy and the momentum must be conserved.

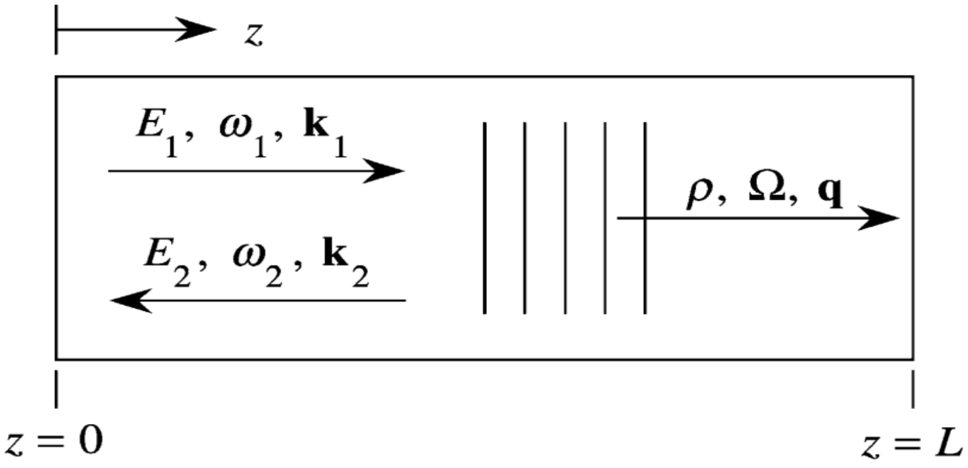

Fig. 2.3: Schematic representation of the stimulated Brillouin scattering [10].

Then the frequencies and the wave vectors of the three waves are deduced as:

$$\Omega_B = \omega_p - \omega_s\,, \boldsymbol{k_A} = \boldsymbol{k_p} - \boldsymbol{k_s} \tag{2.1}$$

Where ω_s and ω_p are the angular frequency of pump and Stokes wave. $\boldsymbol{k_s}$ and $\boldsymbol{k_p}$ are the wave vectors.

- **Wave equation and nonlinear polarization**

The detailed behavior the stimulate Brillouin scattering process can be analyzed through incorporating the propagation equation in fiber and the nonlinear response of materials. The involved optical waves, the incident light and the backscattered light, are considered separately and expressed as:

$$E(z,t) = E_1(z,t) + E_2(z,t) \tag{2.2}$$

Where,

$$E_1(z,t) = A_1(z,t)e^{i(k_1 z - \omega_1 t)} + c.c. \tag{2.3}$$

And

$$E_2(z,t) = A_2(z,t)e^{i(k_2 z - \omega_2 t)} + c.c. \tag{2.4}$$

According to the Maxwell's equation, the evolution of incident and backscattering light can be expressed as:

$$\frac{\partial^2 E_i}{\partial z^2} - \frac{1}{({}^{c}/_{n})^2}\frac{\partial^2 E}{\partial t^2} = \frac{1}{\varepsilon_0 c^2}\frac{\partial^2 P}{\partial t^2}, i = 1,2 \tag{2.5}$$

The total nonlinear polarization, which gives rise to the source term in this equation, is given by:

$$P = \varepsilon_0 \Delta\chi E = \varepsilon_0 \Delta\varepsilon E \tag{2.6}$$

Introduce Eq. (2.3) and Eq. (2.4) into the wave Eq. (2.5) along with Eq. (2.6), and obtain the equations:

$$\frac{dA_1}{dz} = \frac{i\varepsilon_0 \omega q^2 \gamma_e^2}{2nc\rho_0}\frac{|A_2|^2 A_1}{\Omega_B^2 - \Omega^2 - i\Omega\Gamma_B} \tag{2.7}$$

$$\frac{dA_2}{dz} = \frac{i\varepsilon_0 \omega q^2 \gamma_e^2}{2nc\rho_0}\frac{|A_1|^2 2}{\Omega_B^2 - \Omega^2 - i\Omega\Gamma_B} \tag{2.8}$$

Defining the intensities as $I_i = 2n\varepsilon_0 c A_i A_i^*$, we find from Eq. (2.31) that

$$\frac{dI_1}{dz} = -gI_1 I_2 \tag{2.9}$$

$$\frac{dI_2}{dz} = -gI_1I_2 \tag{2.10}$$

Where g is the local SBS gain coefficient, which an approximation expression is given by:

$$g = g_0 \frac{({}^{\Gamma_B}/_2)^2}{(\Omega_B-\Omega)^2+({}^{\Gamma_B}/_2)} \tag{2.11}$$

Where, g_0 is the local gain coefficient dependent on the fiber materials and Γ_B is the Brillouin linewidth. At the central frequency, where $\Omega_B = \Omega$ the Brillouin gain reach its maximum.

2.2 Dynamic optical fiber sensor based on Rayleigh scattering

2.2.1 Overview of phase-sensitive OTDR based on Rayleigh light scatterings

As discussed, there are three different scattering mechanisms that originate from the inhomogeneous physical properties of optical fiber, namely: Rayleigh, Raman and Brillouin scattering. The measurement principle for Rayleigh scattering based sensor is relatively straightforward. Various optical sensing systems based on Rayleigh scattering mechanism including OTDR, phase-OTDR and optical frequency domain reflectometry (OFDR) prevail in both research and industry area. The sensing principle can be generalized as that external environment would have an influence on the physical property of optical fiber which in turn changes optical characteristics of backscattered Rayleigh signal including intensity, phase interference pattern and polarization state. This means that all these parameters could be exploited for high-sensitive measurement with comparatively convenient and cost-effective realization scheme.

Primary implementation of OTDR

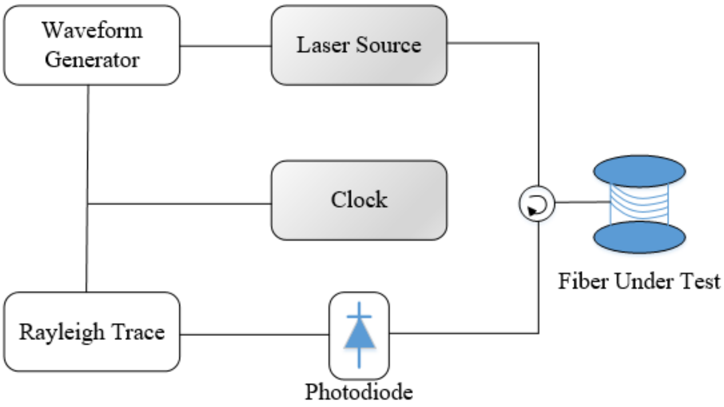

Fig. 2.4: Schematic setup of a generic optical time domain reflectometer [12].

The idea of utilizing Rayleigh scattering signal as sensing components can be traced back to 1960s' [11] . In the beginning, OTDR is proposed for monitoring the fiber attenuation and fault location for telecommunication optical cable [13]. Primary implementation scheme of OTDR is based on optical intensity measurement. As illustrated in Fig. 2.4, the basic implementation setup of OTDR is composed of a light source, optical pulse modulator, Erbium doped fiber amplifier (EDFA), circulator, reel of fiber and a photo detector. It should be mentioned that broadband light source is generally used in the conventional OTDR systems to reduce power fluctuation due to interference. High extinction-ratio optical pulses are generated by modulation and injected into the fiber to guarantee more 'clear' backscattered trace. Then the Rayleigh traces are recorded in chronological order. As Rayleigh scattering is quite weak, large acquisition times are necessary to obtain a distinct observation of the intensity trace distribution. Changes of the obtained trace represent the discontinuities of the transmission medium which reveal the external environment. While the location is acquired by calculating the round-trip time of optical pulse.

Phase-sensitive OTDR

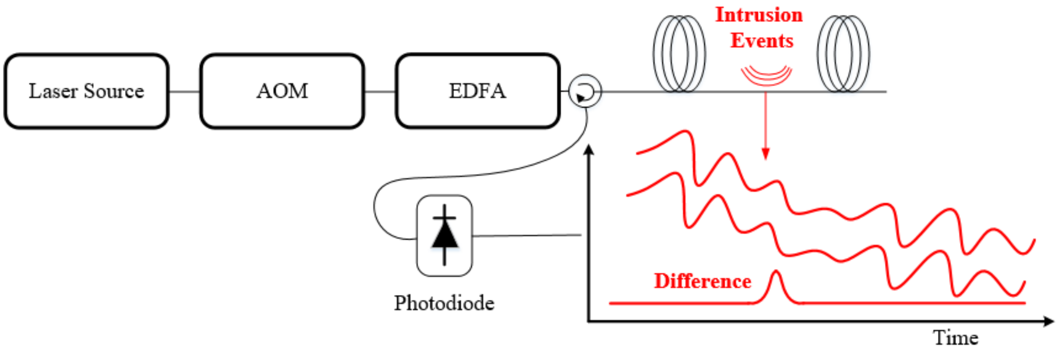

Fig. 2.5: Schematic setup of phase-sensitive OTDR system [13].

For phase-sensitive OTDR (ϕ-OTDR), the laser source with a narrow-linewidth is essential to guarantee the coherent relations between adjacent reflecting scatters. Highly coherent optical pulses are injected into the FUT periodically and the backscattered Rayleigh traces of each pulse are recorded. Generally, the sensing fiber is modeled as multiple random scattering elements each with a small reflectivity coefficient. When reaching the adjacent scatters, optical pulse is reflected independently, and a virtual interferometer is constructed within the optical pulse duration. This process is modeled as summation of multiple coherent Rayleigh traces. As a result, the speckle pattern is formed at the receiver due to the coherence of laser source. The temporal profile of each measurement should remain unchanged if sensing fiber is free from external perturbation. This is the so called 'fiber fingerprint' which is inherent to a specified fiber. On the contrary, the stable coherent interference pattern is distorted as external perturbation is applied. The difference of reflected Rayleigh trace represents the external perturbations.

Phase detection of phase-sensitive OTDR

Distributed dynamic sensing using the phase-sensitive OTDR system by measuring the amplitude have been reported in several literatures [14]-[16]. In the reported systems the frequency of the intrusion events is analyzed according to the detected intensity variation. Obtained result is partial and inaccurate under some conditions. When strong vibration is applied, severe high-order harmonics in the detected amplitude trace along measurement times is caused due to the fact that the monotonic interval of the phase-amplitude transfer function is limited in the range of 2π [17]. That means the amplitude of interference pattern would not direct represent the applied external changes.

To overcome the mentioned drawbacks several advanced schemes are proposed to analyze the phase distribution (e.g. the continuous phase distribution of the interference pattern) in addition to the amplitude [18]-[22]. The principle and basic configuration are quite similar to the common intensity measurement base schemes except that detection end has to be modified to enable detection of phase information. With the help of coherent detection method or interferometer interrogation structure, phase information is recovered which is linearly proportional to the applied strain. In this way, the applied vibration is easily demodulated and accurately converted.

2.2.2 Basic operation principle of dynamic sensing in Phase sensitive - OTDR

Dynamic Measurement principle

Various sensing systems using phase-sensitive OTDR have been proposed to monitor static or dynamic events including temperature, strain or vibrations. The operation principle to implement phase-sensitive OTDR is based on measurement of coherent Rayleigh backscattering trace from FUT. The environment changes to be monitored is analyze through local Rayleigh scattering change along time axis.

As shown in Fig. 2.6, when optical pulse encounter scattering element, part of incident signal is backscattered. The reflected trace from sensing fiber is the summation of N independent traces $T_1, T_2 \ldots T_N$ each with a different scattering coefficient r_i and different phase shift ϕ_i [23]. The scattered light within the duration of pulse length is independent while phase-related due to the coherence of laser source. Therefore, coherent interference is formed at the receiver. Generated optical light of laser source can be expressed as:

$$E(t) = E_0(t)e^{j\omega_0 t} \tag{2.12}$$

where $E_0(t) = \sqrt{I_s} exp\{j\varphi(t)\}$ represent the complex amplitude of optical field operating at central frequency ω_0 with an intensity of I_s and inherent phase noise of laser source $\varphi(t)$. it is worth noted that the magnitude of the phase noise is directly proportional to the linewidth of used laser diode. Reflected optical signal from a single scattering point is:

$$E_{r_i} = E_0(t)e^{-2\alpha z}e^{j\omega_0 t}r_i e^{j\phi_i} \tag{2.13}$$

Where α is the optical attenuation coefficient, r_i is the reflectivity for the i_{th} scattering event. The term ϕ_i account for the total phase change including the accumulated optical field round-trip transmission and phase variation induced by the reflector. z is the distance between the launch end and scattering position. While the backscattered signal at the receiver end is the superposition of the reflected signals within the optical pulse duration period which is expressed as:

$$E(t)_{z=0} = E_0(t)e^{-2\alpha\bar{z}}e^{j\omega t}\sum_{i=1}^{N} r_i e^{j\phi_i} rect(\tfrac{t-\tau_i}{W}) \tag{2.14}$$

Where N is the number of scatters within the pulse duration, W is the width of the optical pulse and τ_i is the time delay for i_{th} scattering event.

$$\tau_i = \frac{z}{c/n} \tag{2.15}$$

$$rect\left(\frac{t-\tau_i}{W}\right) = \left\{\begin{matrix} 1, & 0 \le t - \tau_i \le 1 \\ 0, & otherwise \end{matrix}\right\} \tag{2.16}$$

As the used light source is coherent, reflected optical components would interfere with each other at the receiver end. Optical power of the reflected signal is given by

$$p(t) = |E(t)|^2 \tag{2.17}$$

As can be seen from Eq. (2.25) the resulted power can be divided into two parts

$$p_1(t) = \sum_{i=1}^{N}\{|E_0(t)e^{-2\alpha z}e^{j\omega t}r_i|\}^2 \tag{2.18}$$

$$p_2(t) = 2\sum_{i=1}^{N}\sum_{j=i+1}^{N}\{E_0(t)e^{-2\alpha z}r_iE_0(t)e^{-2\alpha z}r_j\}e^{j(\phi_i-\phi_j)}rect\left(\frac{t-\tau_i}{W}\right)rect\left(\frac{t-\tau_j}{W}\right) \tag{2.19}$$

In which the subtotal $p_1(t)$ is the direct current (DC) component that is composed of N independently scattered light energy only dependent on the incident optical light energy and the reflectivity index. On the other hand, the subtotal term $p_2(t)$ represents the coherent interference pattern of the reflected Rayleigh signal which is composed of the N reflected traces and formed the "jagged appearance". In $p_2(t)$, the cosine function $\phi_{i,j}$ is the phase difference and proportional to laser source frequency ν, scatter space $s_{ij} = z_i - z_j$, the refractive index n.

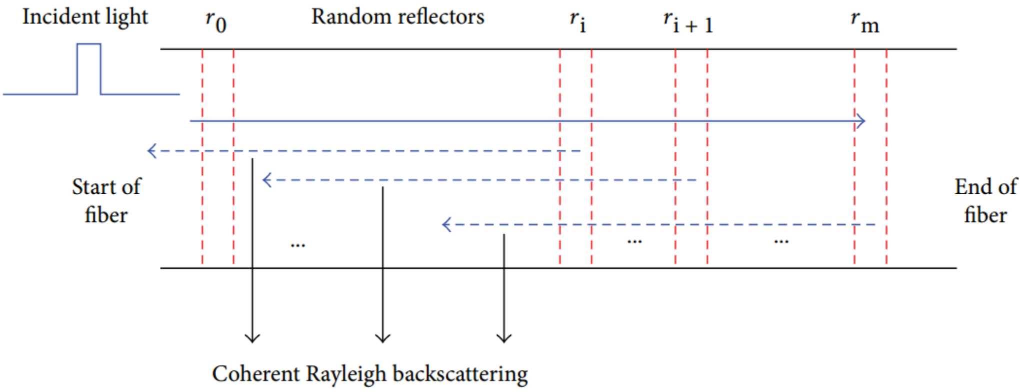

Fig. 2.6: Coherent Rayleigh backscattering in the FUT modeled as a set of randomly distributed scattering elements [23].

Basic implementation setup for phase sensitive-OTDR

The basic schematic diagram for coherent detection phase-sensitive OTDR is illustrated in Fig. 2.7. Typically, a narrow-linewidth laser source like fiber laser is used which is quite

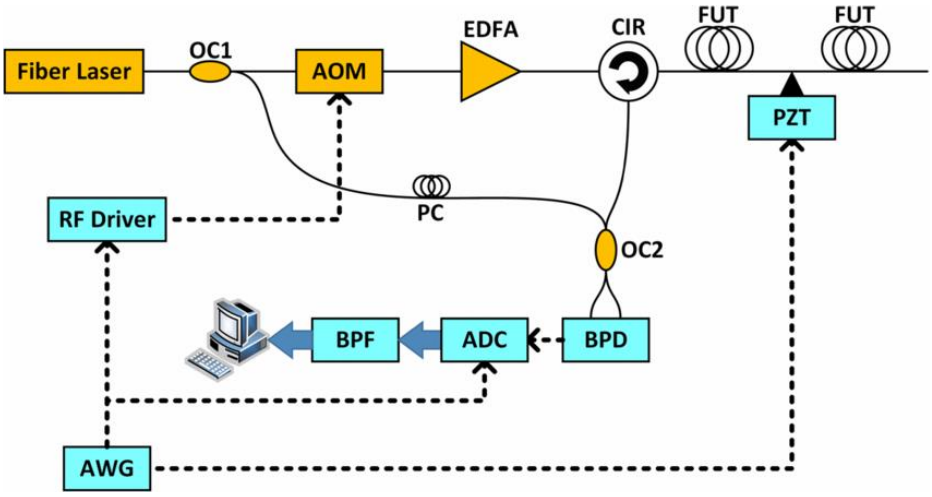

Fig. 2.7: Simplified experimental setup for coherent phase-sensitive OTDR, AOM: acoustic optical modulator; PC: polarization controller; EDFA: Erbium-doped Optical Fiber Amplifier; CIR: Circulator; LPF: low pass filter; FUT: fiber under test; DAQ: data acquisition card. BPD: balance Photo-diode; AWG: arbitrary waveform generator.

cost-effective for distributed fiber sensing system. The output wavelength of the laser source is set at ~1550nm. The CW light is split by a 3-dB coupler into two identical power outputs. The pulse repetition rate is dependent on the fiber length and the pulse width is chosen according to the spatial resolution, and several hundred Mega Hertz frequency shift (typically less than 300MHz) is introduced through an Acousto-optic Modulator (AOM). Power of generated waveform is boosted using an EDFA. Amplified spontaneous emission (ASE) noise is subsequently eliminated by optical filtering typically using fiber Bragg grating (FBG). Afterwards, the optical pulse signal is launched into FUT by a circulator. Another 50% of source light functions as the LO and combined with the reflected Rayleigh signal from FUT before detection. By employing the balanced detection of the beating signal between the Rayleigh signal and LO, a 3-dB improvement could be guaranteed in terms of SNR. Finally, the collected signal at the coherent receiver goes through a RF demodulator which is constructed by mixing with a sine waveform at the same frequency with the AOM modulator driving signal. In this way, the Rayleigh signal is recovered. Collected Rayleigh signal is subsequently processed using an FPGA in practical application or offline in experimental studies with the processing algorithm to be discussed in the following section.

Signal processing methods

In theory, the interference pattern of Rayleigh scattering for a specific sensing fiber remains unchanged if no external vibration is applied. However, in real applications, the obtained Rayleigh trace is influenced by random noise including laser source phase noise, polarization noise, optical noise during transmission in sensing fiber and shot noise upon detection. Accumulated noise would severely distort or even totally change the 'jagged appearance' at far end of sensing fiber. Various DSP methods are proposed to suppress the influence of noise and improve the SNR.

1) Separating averaging method

The most straightforward way to improve the SNR is using average. Normally, we can get an averaged trace by N trace average, so called separating averaging method. The larger the number of traces N used for the average the better the obtained SNR. However, the drawbacks are also obvious. First, it will dramatically reduce the measurement speed. For example, it is easy to know from this averaging method, the larger the average number, the lower the frequency response. Besides, the Rayleigh trace which contain the information of dynamic events varies for each measurement. Taking average for N measured traces inevitably deteriorate the measurement accuracy.

2) Moving averaging and moving differential method

The moving averaging and moving differential method are proposed to alleviate the sensing measurement restriction and improve accuracy. The principle is that there are N raw traces set $r = \{r_1, r_2 \dots r_N\}$, where r_i is the i_{th} raw trace. M moving averaging number is assumed, the averaged traces set is $R = \{R_1, R \dots R_K\}$, $K = N - M + 1$; and

$$R_i = \frac{1}{M}\sum_{l=i}^{l=i+M-1} r_l, \quad l \in [1, N], i \in [1, N - M + 1] \tag{2.20}$$

As the adjacent traces is measured with very short time interval, the variation of reflected intensity is tiny and nearly impossible to figure out applied vibration. Then the differential traces could be obtained by following scheme:

$$\Delta R = \{\Delta R_1, \Delta R_2, \dots \Delta R_J\} \tag{2.21}$$

Where $J = K - 1 = N - M$ and $\Delta R_i = R_i - R_r$, while the value of r which determines the distance between R_i and R_r is set according to the frequency of measurement events. Using this moving differential method, a moving differential window is applied along the obtained traces which merely reduces the effective traces from N to $N - M$ while maintain the maximum detectable frequency and improve the measurement frequency N times compared with the separating average method.

3) Phase demodulation method based quantitative measurement

The algorithms discussed above mainly focused on the amplitude analysis of Rayleigh scattering traces. As previously explained, interference pattern of Rayleigh trace is formed by coherent beating of multiple reflected optical signals. In other words, the intensity distribution is not a direct reflection of measurand. External perturbations first change local reflective index and then introduce phase shift to reflected signals and is then transformed to amplitude fluctuations. However, the linear range of the transformation is limited within $\pi/4$ to $3\pi/4$ if cosine function is considered. In order to achieve quantitative measurement, several processing methods have been developed to demodulate the phase distribution of Rayleigh trace.

- Phase demodulation based on 3×3 coupler

A simple method to extract the phase information of the phase sensitive-OTDR system is based on a 3×3 coupler. The basic operation principle of phase sensitive-OTDR is based on the coherent interference of coherent Rayleigh scattering from neighboring points of the sensing fiber. The signal is therefore the summation of light emanating from two regions of fiber and its magnitude is dependent on their relative phases difference. To avoid signal beating fading, the differential and cross-multiply phase demodulation system is used in which a three port MZI and three detectors are used.

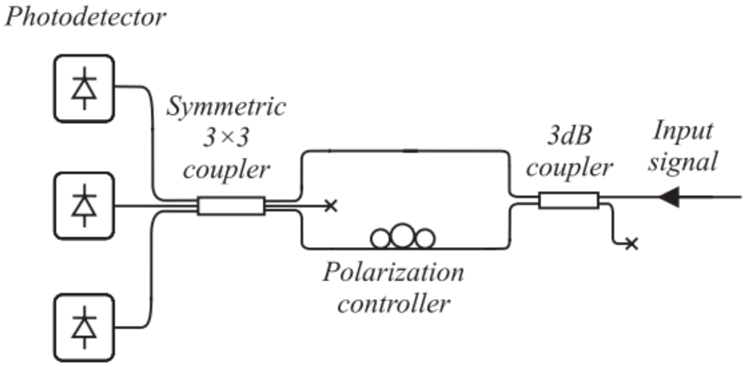

Fig. 2.8 Schematic of the setup used to eliminate signal fading in interferometer by using a symmetric 3 × 3 coupler at the output of the interferometer [24].

In this setup, a three-port coupler and MZI is constructed (Fig. 2.8) with each port introduce different phase shift. The output signal at each port of the 3×3 coupler can be expressed as:

$$I_1 = I_0[M + Ncos(\varphi)] \tag{2.22}$$

$$I_2 = I_0\left[M + Ncos(\varphi + \tfrac{2\pi}{3})\right] \tag{2.23}$$

$$I_3 = I_0\left[M + Ncos(\varphi - \tfrac{2\pi}{3})\right] \tag{2.24}$$

where M and N are constant, φ is the phase difference of the Rayleigh signal. I_0 is the intensity of the input signal. The demodulation method is proposed in [10] which uses the differentiate and cross-multiply method. By introducing an extra 3×3 optical coupler and MZI structure, the phase difference can be measured directly. The output voltage v_{ph} is directly proportional to the phase:

$$v_{ph} = \sqrt{3\varphi} \tag{2.25}$$

- Phase demodulation using I/Q demodulation

Fig. 2.9 shows the general block diagram of I/Q demodulation used in our scheme. Assuming the light source for sensing system described as [21]:

$$A_s exp[i\omega_s t + i\varphi(t) + i\varphi_s] \tag{2.26}$$

Where A_s, ω_s, φ_s are the complex-valued amplitude, the angular frequency and inherent phase noise of laser source, respectively. $\varphi(t)$ is the phase change induced during the propagation in the sensing fiber.

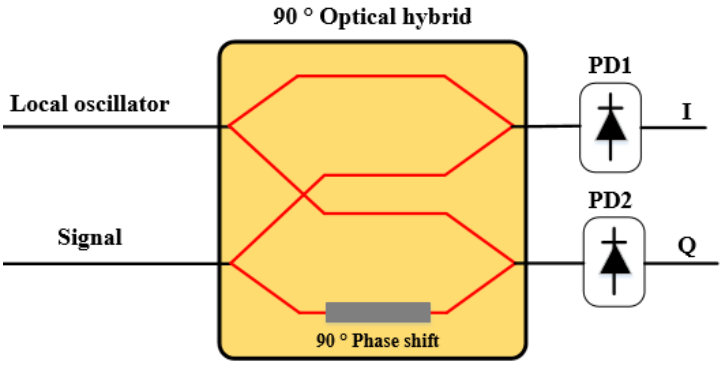

Fig. 2.9: A general block diagram of I/Q demodulation using 90° hybrid [21].

The signal and LO is recombined by the hybrid, and the accurate 90° phase shift is induced in one beam of the signal yield the following optical light field:

$$A_s exp[i\omega_s t + i\varphi(t) + i\varphi_s + i({}^{\pi}/_{2}] \tag{2.27}$$

The LO can be described as

$$A_0 exp(i\omega_0 t + i\varphi_0) \tag{2.28}$$

Where A_0, ω_0, φ_0 are the complex-valued amplitude, the angular frequency and initial phase of LO respectively. The AC components of the photocurrents are:

$$I_{AC} = \frac{1}{2} \cdot R \cdot A_s \cdot A_0 \cdot cos\{(\omega_s - \omega_0)t + \varphi(t) + \varphi_s - \varphi_0\} \tag{2.29}$$

$$Q_{AC} = \frac{1}{2} \cdot R \cdot A_s \cdot A_0 \cdot sin\{(\omega_s - \omega_0)t + \varphi(t) + \varphi_s - \varphi_0\} \tag{2.30}$$

In the setup, the signal and the LO come from the same laser, and no frequency different is present, so $\omega_s - \omega_0 = 0$, $\varphi_s - \varphi_0 = \varphi_d$. φ_d is the difference between the initial phases of the LO and the signal, and we assume that it is a constant. Then we have:

$$I_{AC} = \frac{1}{2} \cdot R \cdot A_s \cdot A_0 \cdot cos\{\varphi(t) + \varphi_d\} \tag{2.31}$$

$$Q_{AC} = \frac{1}{2} \cdot R \cdot A_s \cdot A_0 \cdot sin\{\varphi(t) + \varphi_d\} \tag{2.32}$$

The amplitude and the phase of the RS light can then be obtained:

$$A_s \propto \sqrt{I_{AC}^2 + Q_{AC}^2} \tag{2.33}$$

$$\varphi(t) \approx \arctan\left(\frac{Q_{AC}}{I_{AC}}\right) - \varphi_d \tag{2.34}$$

Here, the value of the arctan function is from ${}^{-\pi}/_{2}$ to ${}^{\pi}/_{2}$. The range of the demodulated phase can extend from negative infinite to positive infinite by using the phase unwrapping algorithm.

2.2.3 Performance analyses of Phase sensitive-OTDR

In phase sensitive-OTDR based sensing schemes, a highly coherent and high peak power optical pulse is injected into the sensing fiber. The backscattered Rayleigh intensity trace is produced by the coherent interference between the neighboring reflectors due to the inhomogeneities of medium in the fiber. As a result, the jagged appearance is formed with a stable pattern.

SNR of phase-OTDR sensing system

As discussed, the obtained SNR in the phase sensitive-OTDR measurement is limited by the optical power and the noise power level in the optical detection. It is important to analyze the noise source during the transmission in optical fibers. Mainly, two types of noise sources are considered in the phase-OTDR measurement: firstly, electrical noises introduced by electrical circuits during the photodetection process (such as shot-noise), secondly, the optical leakage noise due to the finite extinction ratio (ER) and the ASE noise induced by the devices used in the system [25]. We first consider the ER of optical pulse. the peak power of incident optical signal is defined as P_1 and the leakage power is P_2. Then ER is defined as the ratio $\frac{P_1}{P_2}$. It is obvious that higher ER means lower optical noise with the same peak power. Considering an incoherent type of noise then: Intra-band $SNR \propto ER(L_{Pulse}/L_{Fiber})$ where L_{Pulse} and $L_{Fiber}$are respectively the length of the fiber and of the pulse in the fiber. Considering usual parameters ($P_1 L_{Pulse} \gg P_2 L_{Fiber}$) the SNR will therefore be [26]:

$$SNR \propto \sqrt{ER(L_{Pulse}/L_{Fiber})} \tag{2.35}$$

In summary, the increase of the incident optical pulse power will increase the measurement range and SNR of a phase sensitive -OTDR. According to the analysis, we can get better SNR performance in two ways, either improve the peak power of optical pulse P_1 or the resulted ER value. However, the increase of SNR is limited due to the onset of nonlinear effects when P_1 is increased and the increase the optical width L_{Pulse} will reduce the spatial resolution of the system. The increase of ER is often limited by the optical modulator used in the system.

Trade-off among measurement accuracy, spatial resolution, sensing range and SNR

SNR is the most important factor to determine the performance of a phase sensitive-OTDR sensing system. To be specific, both measurement accuracy and sensing range of the system is dependent on the SNR of obtained trace. According to Equation (2.34), the obtained SNR is proportional to the ER of optical pulse and the duration length of the probe pulse. There exist two ways to improve the overall SNR e.g. increase ER or extend the probe pulse length L_{Pulse}. However, the optical probe pulse width is directly related to the spatial resolution. We can extend or narrow down the pulse duration according to the required spatial resolution. In other words, SNR can be improved at the cost of spatial resolution. Another approach is to increase ER of probe pulse including boost the peak power or reduce leakage power level. Under ideal assumptions, the peak power could be boosted to as high as possible to achieve sufficient SNR without compromise the spatial resolution. However, this combination would inevitably lead to severe nonlinearities such as modulation instabilities. These nonlinear impairments impose a maximum power limit to the achievable optical pulses, which in turn reduce the optical power of reflected traces as well as SNR.

Modulation instability-induced pulse fading

To achieve reliable vibration measurements, it is indispensable to have a good SNR in the measured trace. As explained, the sensing range, spatial resolution and obtained SNR are closely inter-related parameters. For a given optical pulse length, no other option is possible if we need to increase the SNR and sensing range except for increasing the peak power of optical light. However, the nonlinear effects in fibers impose the upper limit for the peak power as described in [27]. Among these nonlinear limitations, the first effect to arise in usual conditions for phase sensitive- OTDR is modulation instability (MI). MI in fibers results from the interplay between the Kerr effect and anomalous dispersion [28]. The gain spectrum of modulation instability is given by

$$g(\Omega) = |\beta_2\Omega|(\Omega_c^2 - \Omega^2)^{1/2} \tag{2.36}$$

Fig.2.10 shows the gain spectra for three values of the nonlinear length with given parameters. The gain becomes maximum at two frequencies given by:

$$\Omega_{max} = \pm\frac{\Omega_c}{2} = \pm(\frac{2\gamma P_0}{|\beta_2|})^{1/2} \tag{2.37}$$

When the peak power of the pulsed pump lightwave reaches the threshold of modulation instability, the intensity of the pulsed pump shall be strongly depleted, and side lobes in the frequency domain are stimulated. The peak power distribution of the pulsed pump along the FUT no longer decreases approximately exponentially but drops sharply after propagating over a certain distance. Hence, the received Brillouin signal is significantly distorted as shown in Fig. 2.11. Therefore, the peak power of the pulsed pump lightwave employed in a phase-OTDR system shall be lower than both the thresholds of

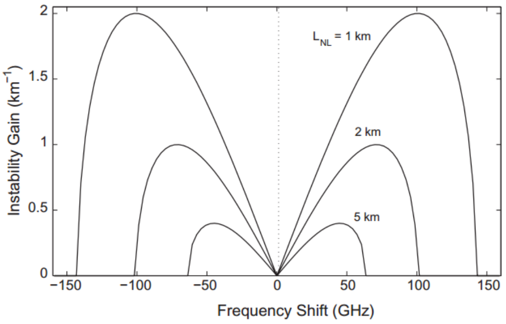

Fig. 2.10: Gain Spectra of modulation instability for three values of the nonlinear length, $L_{NL} = (\gamma P_0)^{-1}$ when a CW beam with power P_0 is launched into a fiber with $\beta_2 = -5ps^2/km$.

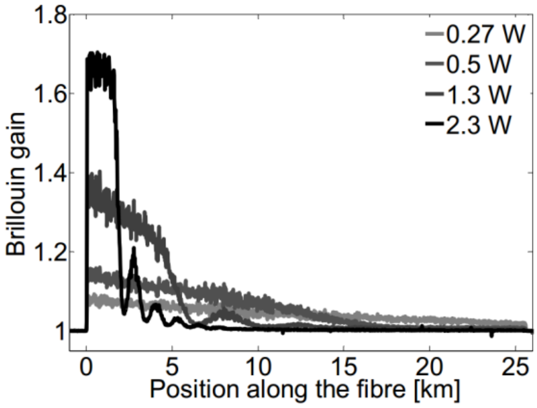

Fig. 2.11: Brillouin gain signals along a 25.5 km SMF fiber showing the pump depletion due to MI after a critical distance depending on the pump peak power [29].

MI and SRS.

Sensitivity

In distributed acoustic sensing (DAS) systems, the measurement of sensitivity is key to the comparison of the performances of individual systems. The sensitivity is defined using the following relationship [30],[31] :

$$\sigma_{min} = \sqrt{\frac{z_p}{2SNR}} \tag{2.38}$$

Where σ_{min} is the standard deviation of the dynamic phase signal which also determines the minimum measurable amplitude, z_p is a dimensionless parameter obtained from the Rayleigh distribution, and SNRs is the static SNR obtained from a single measurement of backscattering signal at the receiver.

2.3 Distributed Optical Fiber Sensing Systems based on Brillouin Scattering

2.3.1 Overview of distributed optical sensing system based on Brillouin scattering

Distributed optical fiber sensors based on the process of nonlinear Brillouin scattering have been investigated for several decades due to their unique advantages over the pointed or other distributed systems. As described above, the phenomenon of Brillouin scattering originates from the acoustic modulation of the dielectric permittivity of transmission medium. The emitted Stokes frequency signal downshifted according to the Doppler shift effect of propagating reflective index grating generated by acoustic wave. Distinguished advantages, such as high sensitivity, quantitative measurement and high accuracy have attracted considerable research interests and a variety of sensor schemes based on Brillouin scattering have been proposed. In recent decades, Brillouin scattering based distributed sensors have been applied extensively in a wide application field.

As reviewed in previous chapter, the optical frequency of Brillouin scattering is directly related to the magnitude of change in surrounding environment. Distributed monitoring of measurand is possible if we can measure the frequency shift of probe signal along the fiber. Therefore, the key of Brillouin scattering based sensing is the measurement of the frequency shift of scattered signal. Several schemes have been proposed towards this end including BOTDR and BOTDA. In BOTDR system, the frequency shift is directly obtained by mixing backscattered signal with a local oscillator to measure the frequency components. In BOTDA system, frequency sweeping method is introduced to control the frequency gap between probe and pump signal to determine the Brillouin amplification profile. Different from the time-resolved schemes like BOTDA or BOTDR, in Brillouin Optical Correlation Domain Analysis/Reflectometry (BOCDA/BOCDR) system, the frequency of the continuous light wave used is varied through modulation method for locating the position and measurement of BFS.

Brillouin optical time domain reflectometer

BOTDR is first proposed in 1980 for measuring strain [32]. Measurement principle and implementation structure are quite similar to phase sensitive OTDR except that the frequency component is analyzed instead of intensity interference pattern. In BOTDR system, the Brillouin pulses are introduced in single end of FUT and the reflect Brillouin scattering traces are collected [33]-[36]. Pulse pump signal with frequency ν is injected into the sensing fiber to generate spontaneous Brillouin scattering. Frequency of backscattered light is shifted by $\Delta\nu$ due to the reflective index modulation effect of acoustic wave. Generally, heterodyne detection technique is used for BOTDR system to improve the sensitivity and SNR. $\Delta\nu$ is measured by mixing the Brillouin scattering traces with a reference LO before detected by a balanced photo detector (PD). Then, detected electrical signal is analyzed with post-processing algorithms to obtain the frequency composition. Since the frequency shift is linearly proportional to both the temperature and strain with a fixed coefficient, the measurand is easily determined.

BOTDA

Though quite simple, BOTDR did not prevail both in the research and application area. Main drawback of the scheme is the sensing range of the system is limited by the intrinsic nature of spontaneous scattering which is an order lower than the stimulated one. In BOTDA, the backscattered optical light is stimulated by high power pump signal with a much higher power transfer efficiency [37]-[43]. This mechanism guarantees better sensing range with higher SNR. In BOTDA sensor, Brillouin gain (or loss) profile is measured with a pulsed-optical wave (or pump) and a counterpropagating CW light (or probe), transmitting in the sensing fiber in opposite directions. When the frequency mismatch $\Delta\nu = \nu - \nu_B$ between pump and probe signal is tuned to the Brillouin frequency shift ν_B of the fiber, the probe signal will be amplified through SBS. Therefore, the increasement of probe signal along the sensing fiber is recorded as a function of time.

2.3.2 Operation Principe of BOTDA

Analytical model of BOTDA

The simplified analytical model of BOTDA system is illustrated in Fig. 2.12 [44]. Pulsed pump signal is introduced into the FUT from location $z = 0$ while the continuous wave probe signal is injected from the other direction from $z = L$. Where L is the total length of the FUT. The frequency difference ν between pump and probe signal is tuned continuously to find the resonance point which the optical scattering between pump and probe maximize, known as the BFS. The pump and probe signal can be described as:

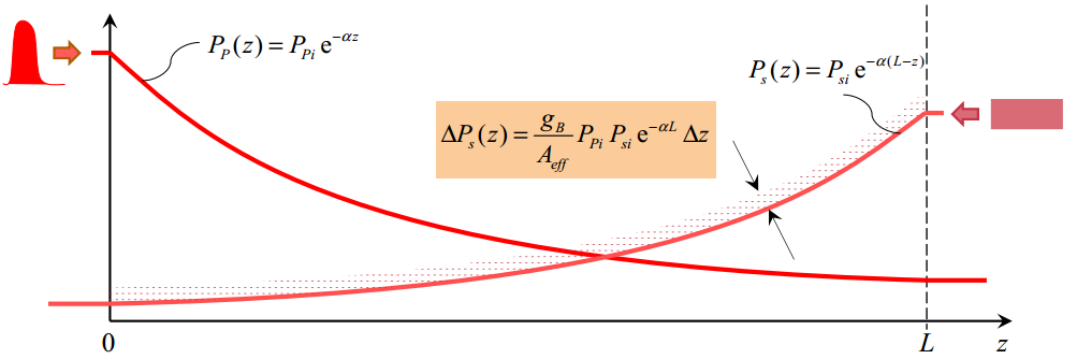

Fig.2.12: The diagram of the pump-probe configuration for conventional BOTDA. At each position z, the local Brillouin gain is proportional to the product of probe power, pump power and the gain coefficient. [44].

$$P_p(z) = P_{pi}exp(-\alpha z) \tag{2.39}$$

$$P_s(z) = P_{si}exp\{-\alpha(L-z)\} \tag{2.40}$$

Where P_{pi} and P_{si} are the optical power of pump and probe signal. α is the fiber attenuation coefficient. The energy transferred between pump and probe signal is described as:

$$\Delta P_s(z) = \frac{g_B(z)}{A_{eff}}P_p(z)P_s(z)\Delta z \tag{2.41}$$

Where $g_B(z)$ is the Brillouin gain coefficient which is dependent on the material, A_{eff} is the nonlinear effective area of the guided mode and Δz is interaction region of pump and probe signal which is dependent on duration length of pump signal. g_B take the shape of Lorentzian spectrum described by the formula [10]:

$$g_B(\nu) = g_p\frac{({}^{\Gamma_B}/_2)^2}{(\nu-\nu_B)^2+({}^{\Gamma_B}/_2)^2} \tag{2.42}$$

Where g_p represents the peak power of the Brillouin gain when the frequency ν is tuned at the resonance frequency ν_B which is called BFS. Γ_B is related to the photo lifetime $\tau = \Gamma_B^{-1}$. In principle, the pulse width must be longer than the acoustic lifetime $\tau = 10ns$.

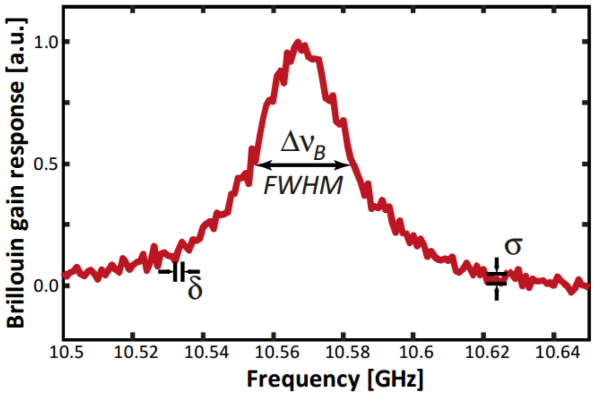

Fig.2.13: Typical local Brillouin gain spectral response after normalization[44].

$\Delta P_s(z)$ is the increasement of probe signal power. BOTDA sensor commonly operates in small gain regime, i.e. $\Delta P_s(z) / P_s(z) \ll 0.1$ which means the pump depletion is negligible. For simplicity, we ignore the extra power loss of pump signal in the SBS process. Considering Equation (2.38) and (2.39) the expression of Equation (2.40) can be rewritten as:

$$\Delta P_s(z) = \frac{g_B(z)}{A_{eff}} P_{pi} P_{si} \exp(-\alpha L) \Delta z \tag{2.43}$$

Equation (2.42) describes the local power increasement for probe signal. It is easy to find that the energy transfer between pump and probe signal is only dependent on the input energy of pump and probe signal while irrelevant to location z.

However, the local gain is measured at location $z = 0$. It implies that the probe signal as well as the stimulated Brillouin gain will experience an exponential attenuation as transmitting from $z = L$ to $z = 0$ in the fiber. Hence, the local sensor response measured at the near end is:

$$\Delta P_s^0(z) = \Delta P_s(z)exp(-\alpha_s z) = \frac{g_B(z)}{A_{eff}} P_{pi} exp(-\alpha z) P_{si} exp(-\alpha L)\Delta z \qquad (2.44)$$

This expression corresponds to the local sensor response measured at the near end of fiber. Therefore, the measured gain for probe signal is obtained by dividing Equation (2.43) with the input probe power:

$$Gain(z) = \frac{\Delta P_s^0(z)}{P_{si} exp(-\alpha_s L)} = \frac{g_B(z)}{A_{eff}} P_{pi} exp(-\alpha z)\Delta z \qquad (2.45)$$

As depicted in Fig. 2.12, the local gain for probe signal is proportional to the product of probe power, pump power and the gain coefficient. If the gain coefficient is assumed uniform along sensing fiber for simplicity, the profile of the amplification trace would show exponential decrease in accordance with the fiber attenuation.

Sensing principle

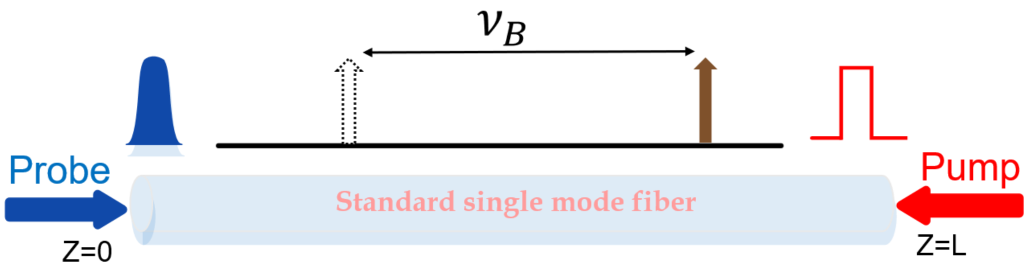

Fig. 2.14: the sensing principle of BOTDA.

Conventionally, the pump-probe configuration is used to map the BFS distribution along the FUT. In BOTDA, the pulse pump wave is injected from one end of the fiber interact with CW probe signal introduced from the opposite direction. As shown in Fig. 2.14, by scanning the frequency ν detuning between probe and pump around Stokes frequency (~ 11GHz @ 1500nm) at a step of $\Delta\nu$ and record the probe power at the output of fiber under test, the gain spectrum of probe signal at different frequency detuning is then analyzed to find the location of its peak and thus deduce the BFS ν_B.

Spatially resolved BFS distribution is linearly proportional to the surrounding environments including the temperature and applied strain. The coefficient of temperature and strain is about 1℃/MHz and 20 με/MHz, respectively. By calculating the variation of BFS at each location, the measurand is thereby determined. Therefore, the scanning step Δv define frequency resolution of BGS corresponding to the minimum distinguishable magnitude of measurand. While the scanning range is the maximum detectable range of change for applied measurand. The position of the hot spot is measured according to the round-trip time of the optical pump pulse.

Measurand dependence of Brillouin frequency shift

The BFS in the optical fiber is given as $\nu_B = 2n\nu_A/\lambda$. According the expressing, the value is dependent on the RI n of fiber, the acoustic velocity ν_A and optical wavelength λ . When the wavelength of the lightwave is given, the dependence of BFS value on the measurand can be expressed as:

$$\partial\nu_B = \nu_B\{\frac{\partial n}{n} + \frac{\partial\nu_A}{\nu_A}\} \tag{2.46}$$

The refractive index n is determined by the relative dielectric constant ε and the relative magnetic permeability μ, which can be expressed as:

$$n = \sqrt{\varepsilon\mu} = \sqrt{\varepsilon} \tag{2.47}$$

where μ is the effectively unity for nonmagnetic substances [45]. The acoustic velocity ν_A is given in [46]:

$$\nu_A = \sqrt{\frac{K}{\rho}} = \sqrt{\frac{E_Y(1-\zeta)}{(1+\zeta)(1-2\zeta)\rho}} \tag{2.48}$$

where K is the bulk modulus, ρ is the density, E_Y is the Young's modulus, and ζ is the Poisson's ratio of fused silica fiber.

Strain and temperature dependence of Brillouin spectrum

While the strain dependence on BFS can be expressed as:

$$C_s = \frac{\partial\nu_B}{\partial s} = \nu_B\{\frac{1}{n}\frac{\partial n}{\partial s} + \frac{1}{V_A}\frac{\partial V_A}{\partial s}\} \tag{2.49}$$

The strain dependence of n and υ_A can be analyzed by the model of the elastic-optic effect [47] and the theory of elasticity [46]. As shown in Fig. 2.15, the BFS value corresponding to different temperature/strain values clearly indicates the linear dependence.

Similarly, the variation of the temperature shall affect the refractive index and the acoustic velocity in the fiber as well. The temperature dependence coefficient C_T can be written as:

$$C_T = \frac{\partial \nu_B}{\partial T} = \nu_B \{ \frac{1}{n}\frac{\partial n}{\partial T} + \frac{1}{V_A}\frac{\partial V_A}{\partial T} \} \tag{2.50}$$

The temperature dependence of Brillouin spectrum is much more complicated, though the Brillouin frequency shift is generally regarded to be linearly increasing with the ambient temperature with a slope of about 1 MHz/°C. However, both the refractive index and the elastic constants do not always change linearly with the ambient temperature [48], [49]. Researches have been found that there exist linear limits for temperature measurement [50], [51]. To avoid ambiguity, the experiment discussed in the following is within the linear part of temperature variation.

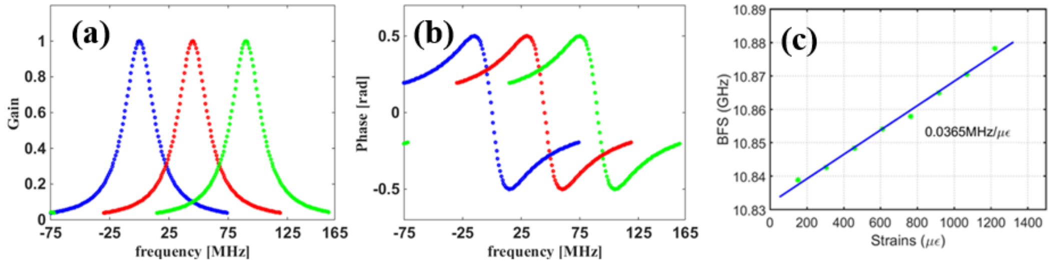

Fig. 2.15: Dependence of (a) Brillouin gain spectrum and (b) Brillouin frequency shift with applied tensile strain.

2.3.3 Performance of BOTDA

SNR

The SNR for BOTDA sensor is defined as the ratio between maximum amplification power and the average noise power. As discussed, the local gain for probe signal is proportional to the product of probe power P_{si}, pump power P_{pi} and the gain coefficient$g_B(z)$. As the probe wave is amplified by pump pulse during travelling in the sensing fiber from opposite direction. The increasement of probe power is detected at the receiver end and the average noise power is also calculated. The maximum power gain of probe signals after SBS amplification can be expressed as:

$$\Delta P_s(\nu_B) = \frac{g_P}{A_{eff}} P_{pi} P_{si} exp(-2\alpha L) \Delta z \tag{2.51}$$

The detected current by photodetection is:

$$I_s = R_D \Delta P_s(\nu_B) \tag{2.52}$$

Where R_D is the responsivity of photodetector, the signal to noise ratio of a conventional BOTDA setup is:

$$SNR = \frac{\Delta P_s^2(\nu_B)}{\sigma_D^2} \tag{2.53}$$

Where σ_D^2 is average accumulated optical noise power of the system.

Power limitations of probe signal

The power of the probe signal is limited by non-local effect [52]. This phenomenon is mainly caused by the continuous energy transfer between pump signal and probe signal. During the propagation in the FUT, the power of pump is gradually depleted by the SBS process which is cumulative for the pump signal. As shown in Fig. 2.16, the obtained BGS is biased with depleted pump power resulting in systematic measurement error.

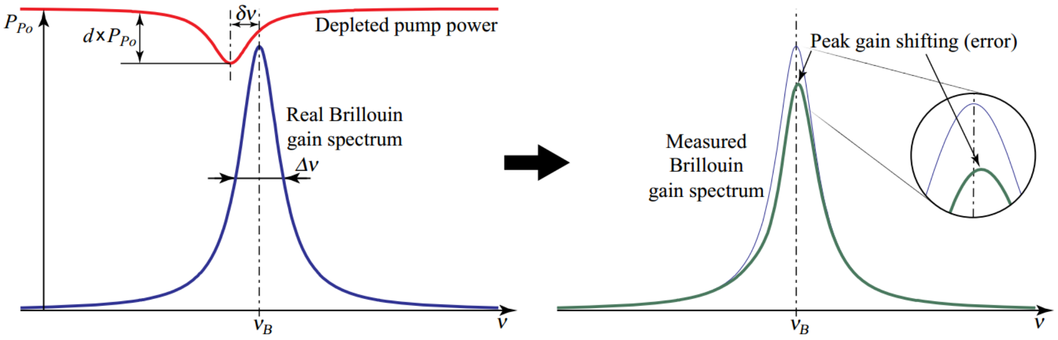

Fig. 2.16: Non-local effect due to the accumulative power depletion of pump signal [52].

Power limitations of pump signal

Increasing the peak power of the pulsed pump lightwave may also lead to the pump depletion. As discussed, modulation instability results from the Kerr effect and anomalous dispersion gives rise to the soliton self-building process. When the peak power of the pulsed pump lightwave reaches the threshold of modulation instability, the intensity of the pulsed pump shall be strongly depleted and transferred to side lobes in the frequency.

Measurement speed

Measurement time is an important factor that restricts the application of BOTDA system. A complete implementation of BOTDA measurement process is comprised of the following steps: scanning the frequency shift between pump and probe signal, recording the probe amplification trace and repeating trace measurement to required average times. Therefore, the factors limiting the measurement speed for commonly investigated DOFS systems can be summarized as [53]:

1) **Time of flight** T : depending on the sensing fiber length. The time interval between two interrogation pulses need to be larger than the round-trip time of pump signal. The repetition rate of the pump pulses should not exceed ${}^{1}/_{T_{round\_trip}} = {}^{2L}/_{v_g}$, where v_g is the group velocity speed and L is the sensing fiber length. This factor depends on fiber length and thus can not be improved.
2) **Averaging time** N: the optical scattering process is usually quite weak. Therefore, sensing systems based on optical scattering mechanism commonly requires hundreds of averages for the detected signal to improve the obtained signal-to-noise ratio (SNR) especially over long fibers.
3) **Frequency scanning time** N_f: for Brillouin scattering based DOFS system, the frequency sweep is inevitable in order to characterize the Brillouin amplification(loss) profile which is directly related to the measurand. Typically, several hundreds of sweeping is needed with scanning step of ~MHz and scanning range of several hundred MHz.
4) **Optical frequency switching speed** T_s: for the electrical devices like synthesizer or polarization scrambler, the stabilization time should be considered depending on the actual implementations which usually on the order of milliseconds.

In summary, the total time need for a BOTDA measurement can be expressed as:

$$(T + T_s) \cdot N \cdot N_f \tag{2.54}$$

Equation Chapter (Next) Section 1

3 Application of Phase sensitive - OTDR system for dynamic measurement of telecommunication system

In this chapter, an integrated telecommunication system and phase sensitive-OTDR sensing system with shared optical bandwidth is reported. The dynamic measurement of telecommunication system using Phase sensitive-OTDR sensing technology is investigated. OFDM modulation technique is selected and applied in our communication system as it is widely recognized as one of the major transmission techniques of modern telecommunication networks with many advantages. In our system, 16QAM-OFDM signal at 112Gbit/s is transmitted over 20km SSMF. Meanwhile distributed phase sensitive-OTDR system is deployed to monitor the environmental variation along the fiber.

3.1 Introduction

Fiber-optics communications technologies have developed rapidly in recent decades with advanced modulation formats, amplification mechanism and high sensitivity optical receivers to meet the explosive capacity demands of internet service [54]. In telecommunication systems, optical fiber is utilized as the transmission medium with the outstanding characteristics of high capacity and low attenuation. Over 10Tbit/s transmission have been demonstrated with normal single mode fiber. Optical fiber network which forms the infrastructure of information technology have been deployed widely connecting cities, towns, highways and links countries.

However, the optical fibers used in the telecommunication cables are vulnerable and susceptible to external perturbations such as earthquake, building construction or extreme weather conditions. Several cases have been reported and they have all caused great loss with significant interruption to internet services [55],[56] . Therefore, monitoring of the transmission system to enable early detection of these external perturbations is vital to ensure stable operation of communication network.

Various distributed optical fiber sensor techniques have been proposed and investigated in depth for different application scenarios [57]-[60]. Among them, the Phase-OTDR has been demonstrated as a suitable candidate for distributed sensing with meter-scale spatial resolution and ultra-fast responding time of several milliseconds [61]-[63].

In phase sensitive-OTDR system, highly-coherent optical pulses are transmitted into the FUT periodically and the Rayleigh backscattering optical signal of each pulse is recorded. Generally, the sensing fiber is modeled as multiple random scattering elements each with a small reflectivity coefficient. Virtual interferometer is constructed by neighboring reflectors within the optical pulse duration. As a result, the speckle pattern is formed at the receiver due to the phase difference between massive reflected optical signals. The temporal profile of each measurement should keep constant if sensing fiber is free from intrusion. Otherwise, the feature of the intrusion is readily extracted by monitoring the change of recorded trace for successive optical pulses. Phase sensitive-OTDR system is extremely sensitive as the phase change of light induced by external intrusions could be directly obtained.

In this chapter, the study on an integrated telecommunication system and phase sensitive-OTDR sensing system with shared optical bandwidth is described. OFDM modulation technique is selected and applied in our communication system as it is widely recognized as one of the major transmission techniques of modern telecommunication systems with numerous advantages. In our system, 16QAM-OFDM signal at 112Gbit/s is transmitted over 20km SSMF. Meanwhile distributed phase sensitive-OTDR system is deployed to monitor the external vibration along the fiber. It should be noted that these two systems share the same optical source before being modulated and launched into the FUT. Hence, the mutual influence is inevitable. Experimental results for the communication system show that, compared with unaffected OFDM frames, about 1 dB OSNR penalty to bit-error-rate (BER) performance is observed in the affected frames by the high-power optical pulse used in sensing configuration. On the other hand, the influence of communication signal on sensing system is almost negligible as the reflected power of the OFDM signal is extremely weak (more than 30 dBm lower than reflected phase-OTDR signal). 20 m spatial resolution and SNR of location information as high as 6.5 dB is obtained with 20 km fiber length. Detection of 1kHz vibration applied by PZT is also successfully demonstrated.

3.2 Operation principle, experimental setup and signal processing

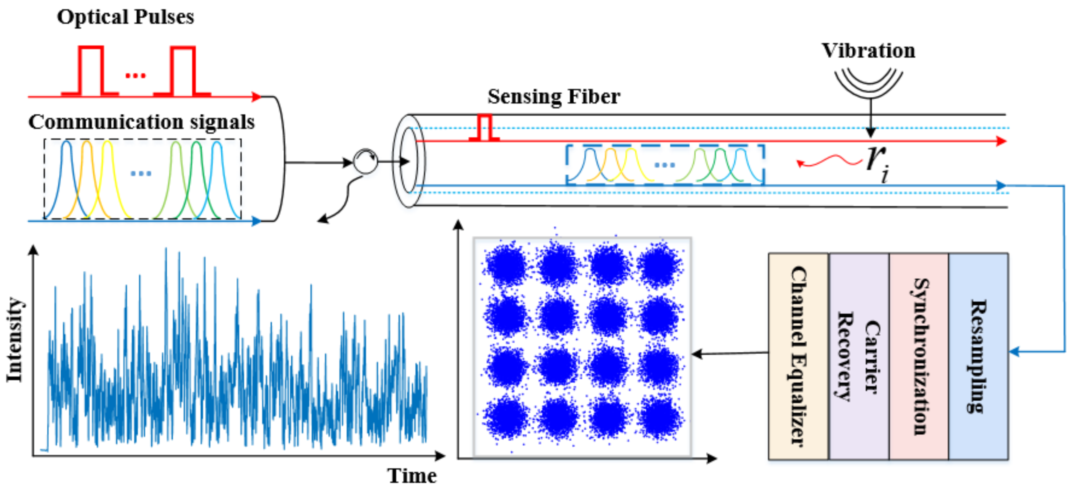

Fig. 3.1: Illustration of operation principle of integrated telecommunication system and phase-OTDR.

Fig. 3.1 illustrates the operation principle of the integrated optical communication system and phase-OTDR sensing system. The optical communication signal is launched into the telecommunication link accompanied by lower repetition rate optical pulses. These signals are multiplexed in the frequency domain and transmitted in fiber simultaneously. In general, optical systems occupy the frequency range up to several gigahertz. Especially for OFDM techniques, the frequency band occupied is easily selected by controlling the frequency tones used for loading of data.

In our systems, 16QAM-OFDM signal is used for data transmission. Sequence of bit is first mapped onto complex-valued 16-QAM format. Generated 16QAM serial symbols are assigned to 80 subcarriers out of 256 orthogonal frequency tones which subsequently are transformed to the temporal OFDM frames with inverse fast Fourier transform (IFFT) [64],[65]. The expression for OFDM frame can be described as:

$$E(t) = \sum_{k=-N/2+2}^{N/2} c_k \, exp(j2\pi\nu_k t) \quad 0 \le t \le T \qquad (3.1)$$

Where N is the number of carriers, c_k represents complex-value 16-QAM signals, T is the frame length and ν_k is the frequency for the k^{th} carrier. A complete OFDM frame used for data transmission is composed of 5 groups of OFDM blocks. Cyclic prefix (CP) is inserted between each block to eliminate the inter-symbol interference (ISI). And in front of the frame, the pre-defined synchronization head is inserted. In the end, 20 percent clipping is applied to reduce the peak-to-average power ratio (PAPR) and improve efficiency of modulation and amplification. A pilot tone is added to the temporal OFDM frames to measure carrier frequency offset. While with the (arbitrary waveform generator) AWG operating at a sampling rate of 90Ghz, the resulted bandwidth of obtained OFDM signal is from ~300MHz to 28.125GHz.

At the receiver, reflected Rayleigh signals is detected with a coherent receiver. As explained, the distortions from OFDM signal is negligible as it is easily filtered out with offline processing method. Then obtained Rayleigh traces are analyzed with moving differential method to locate the intensity fluctuation position e.g. the vibration point [59]. Then I/Q demodulation method is adopted to analyze the phase variation at specified location[66].

While for the communication signals, the optical OFDM temporal frames is also detected with coherent receiver and collected with a high bandwidth oscilloscope. As we can tell from the figure, only a small portion of the OFDM frames -200ns duration length to be exactly- are distorted by high power optical pulses while left the others unaffected. This part is therefore referred as ‘affected’ frames. The incoming frames are first resampled due to the sampling rate mismatch between AWG and oscilloscope. Afterwards, inserted synchronization head is found using correlation algorithm to locate and process OFDM frames separately. Carrier frequency drift is compensated by pilot tone. For each OFDM frame, the first data block is used as training symbols to calculate the channel response including amplitude and phase change. Then remaining blocks are totally compensated with the obtained channel response [67],[68].

However, for the ‘affected’ frames the demodulation process is quite different. Apart from OFDM signals, an additional optical pulse is introduced and mixed with LO at the receiver. It must be emphasized that the optical pulses functions as a 'second' LO in the coherent detection process rather than merely an additive intensity pulse. The output current is written as:

$$E(t) = Re \cdot \{E_{LO} + E_{Pulse} + E_s\}$$
$$= Re \cdot \{A_{LO} \exp(j\omega_0 t + \varphi_{LO}) + A_p \exp(j\omega_0 t + \varphi_P) + \textstyle\sum_{k=-N/2+1}^{N/2} c_k \, exp(j2\pi v_k t) \tag{3.2}$$

Where A_{LO} is the complex amplitude, ω_0 and φ_{LO} the angular frequency and phase of LO respectively. A_p and φ_P are the complex amplitude and phase of LO. The electrical field of the detect signal can be expressed as:

$$I(t) \propto |A_{LO} + A_P|^2 \textstyle\sum_{k=-N/2+1}^{N/2} c_k \exp(j2\pi v_k t + \theta) \tag{3.3}$$

As indicated in Equation (3.3), an extra phase rotation term θ and amplitude distortion is induced by optical pulse. The DC component is easily eliminated with a high-pass filter. θ can be estimated by calculating the phase change of pilot tone within the pulse duration length.

3.3 Experimental setups

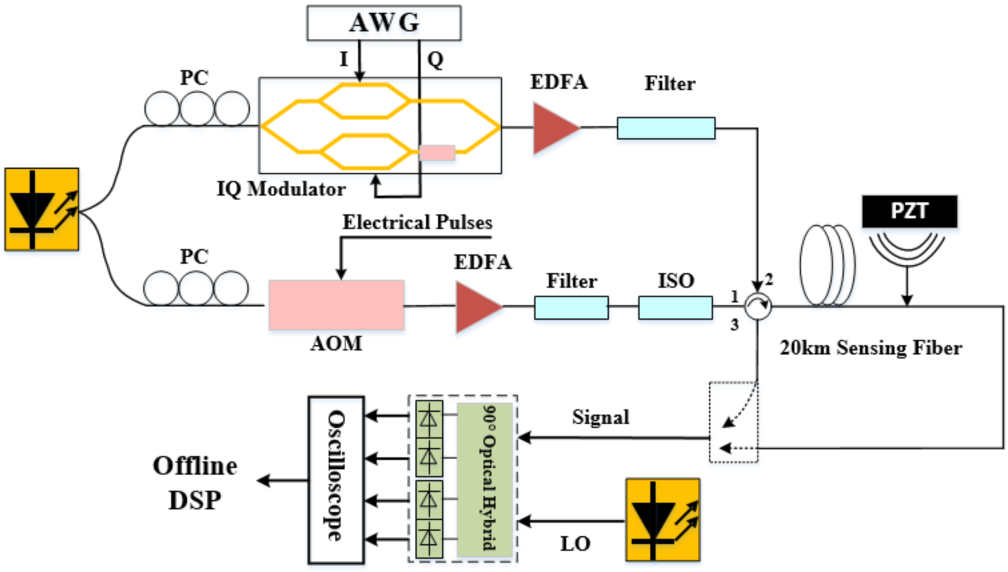

Fig. 3.2: Experimental Setup of proposed system. PC: polarization controller; I: in-phase; Q: quadrature; EDFA: erbium-doped fiber amplifier; ISO: isolator; AOM: Acoustic Optic Modulator; AWG: arbitrary waveform generator; PZT: Piezo-ceramic Transducers; LO: local oscillator; DSP: digital signal processing.

The structure of the integrated fiber communication and optical sensing system is shown in Fig. 3.2. The laser source is a highly coherent narrowband laser with a linewidth of 100Hz. Output wavelength is 1551 nm with the maximum power of 16dBm.

The CW light is split by a 50/50 coupler. 50 percent of the optical signal is transmitted into the IQ modulator which is driven by two identical electrical amplifiers. The modulator is biased at null point by an auto bias-controller. The delivered 256-point fast Fourier transform (FFT) size 16QAM-OFDM signals are generated in MATLAB before used to program the AWG with a sampling rate of 90GHz. As described in the principle, 80 subcarriers occupy 28GHz bandwidth is used for data transmission. A pilot of

15GHz frequency is inserted into the OFDM signal. The time duration for a complete data package which is composed of 640 frames in total is $1\mu s$. In-Phase and Quadrature part of the OFDM signal generated by AWG are modulated onto the corresponding orthogonal optical carriers through an IQ modulator. An EDFA is inserted before transmitting the modulated signal into the fiber under test to ensure the suitable launch power. An optical isolator is placed in front of the circulator to prevent high power optical reflection noise.

At the receiver, ASE noise generator is used to control the obtained OSNR. Coherent receiver is employed to detect the full field of the transmitted complex signal. OFDM signal is mixed with a LO through an optical hybrid and detected by balance detectors. The two outputs representing the real and imaginary part of OFDM waveform are subsequently collected by an oscilloscope operating at 80GHz sampling rate. The collected samples are further processed in the software to analyze the BER performance.

While for phase sensitive-OTDR system, a high-extinction ration AOM modulator is used to generate the high extinction ration optical pulses. Periodical electrical pulse signal and duration length of 200ns is applied to the radio frequency (RF) port of modulator. Repetition rate is 10kHz based on the fiber length. Extinction ratio of about 40dB is achieved. The generated optical pulse is amplified by an EDFA to an average power of 0dBm. Afterwards, OFDM signal and optical pulsed are combined with an optical coupler and launched into the 20km fiber through an optical circulator. 20 meters of fiber near the end of the FUT is wound around a PZT which is controlled by a signal generator. In this way, deformation is applied with arbitrary waveform. Backscattered Rayleigh signal is first amplified by an EDFA to meet the detection limitation of coherent receiver. After that, narrow band optical filter centered at 1551nm is used to eliminate amplified spontaneous emission noise. The Backscattered Rayleigh signal is then converted to electrical signal and sampled by an oscilloscope.

3.4 Experimental results

To investigate the mutual influence between communication and sensing signal of the integrated system, the performance of optical communication system in the absence of sensing system is evaluated first.

Evaluation of the optical OFDM system

In our experiment, the launch power of optical OFDM signal is 5dBm. The OSNR of obtained optical OFDM signal at the output of 20km fiber is analyzed with optical spectrum analyzer (OSA). By controlling the injected ASW noise power, obtained OSNR from 18 to 24dBm with a step of 0.5dBm is easily guaranteed. For each OSNR value, the corresponding OFDM signal is recorded by high sample rate oscilloscope. The obtained OFDM signals are presented in Fig. 3.3. A high-power optical pulse is inserted into the temporal wave of detected OFDM signals. The detected OFDM signal with different OSNR is processed following the described algorithm to obtain the BER.

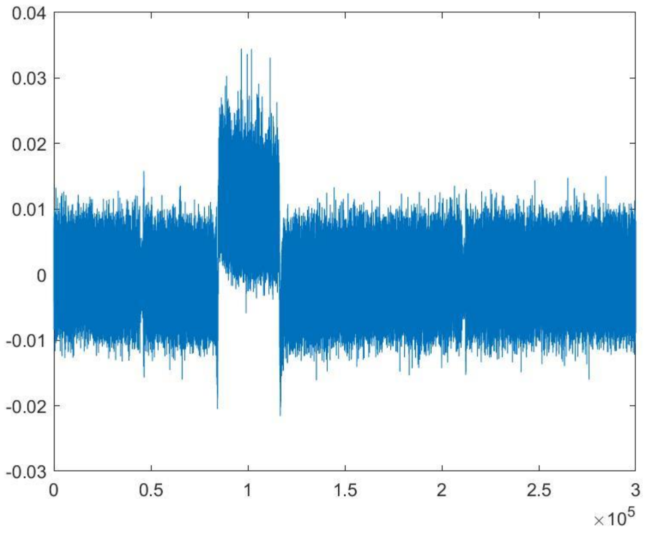

Fig. 3.3: OFDM signals distorted by optical pulses.

In the experiment, pilot tone of 15GHz frequency is inserted to evaluate the frequency offset Δf between laser source and LO. As indicated in Fig. 3.4, the frequency band occupied by OFDM signal distributes between -20GHz to 20GHz which is not influenced by pilot tone. Then, frequency mismatch Δf is accurately estimated by calculating the frequency of pilot tone.

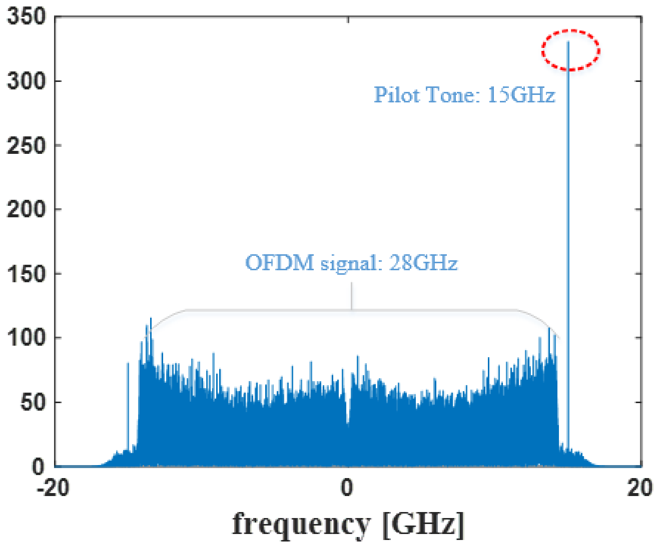

Fig. 3.4: Frequency offset estimation with pilot tone.

After frequency offset compensation, synchronization algorithm is applied to locate the position of OFDM frame by calculating the correlation between synchronization head

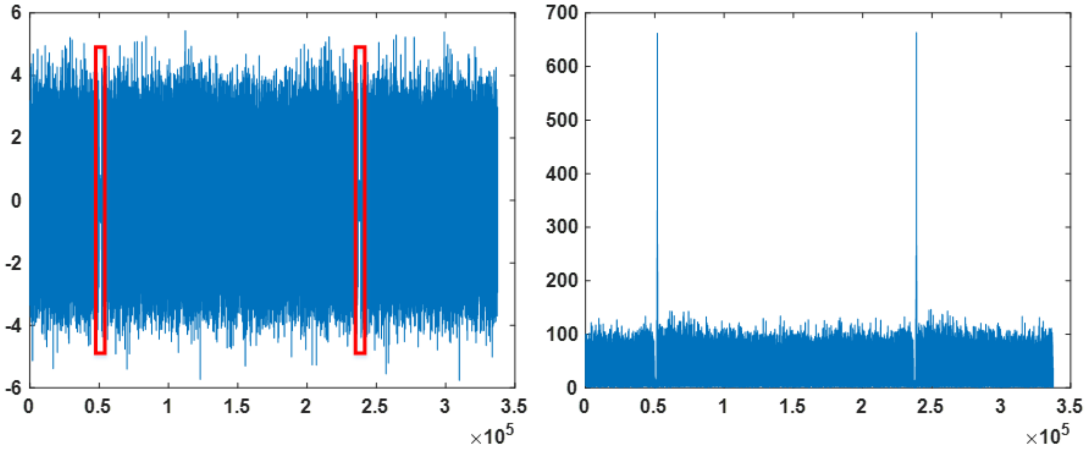

Fig. 3.5: Received OFDM samples and correlation value of synchronization algorithm.

and received OFDM signal. Peak of correlation value indicate the starting sample of received OFDM frame.

Followed by serial to parallel conversion, the channel response of training symbols is obtained first. 128 blocks are used for the measurement of complex channel response value including amplitude and phase responses $\{H_1, H_2 \ldots H_{128}\}$. Taking the average of the 128 groups of measurement result, the accurate estimation H is acquired which is subsequently used for frame recovery. The BER value for each OSNR value is obtained at the last step.

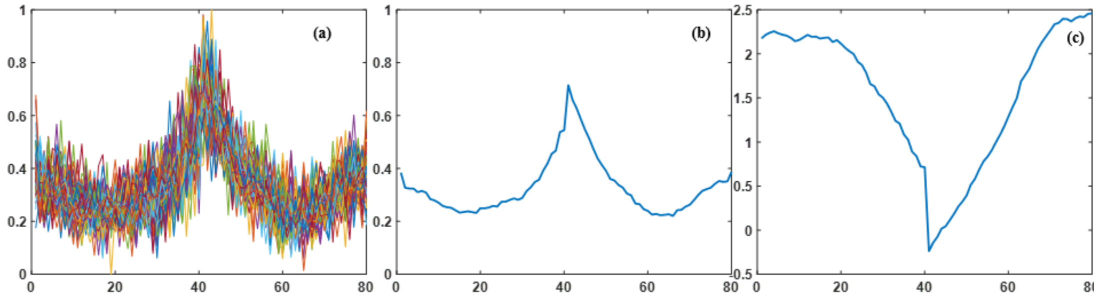

Fig. 3.6: The measured channel response using training symbols. (a) 128 channel response measurement results. (b) Amplitude response of the average channel response measurement. (b) Phase response of the average channel response measurement.

To draw a comparison, the simulation is also conducted using the ‘BerAWGN’ tools provided by MATLAB. In the simulation, Additive white Gaussian noise (AWGN) channel is assumed for the optical OFDM transmission. Taking the modulation format (16QAM) and bandwidth used in the transmission into account, the measured BER performance in experiment is consistent with the theoretical curve with acceptable degradation. As shown in Fig. 3.7, a maximum of 1dB degrade is observed between simulation and experiment results.

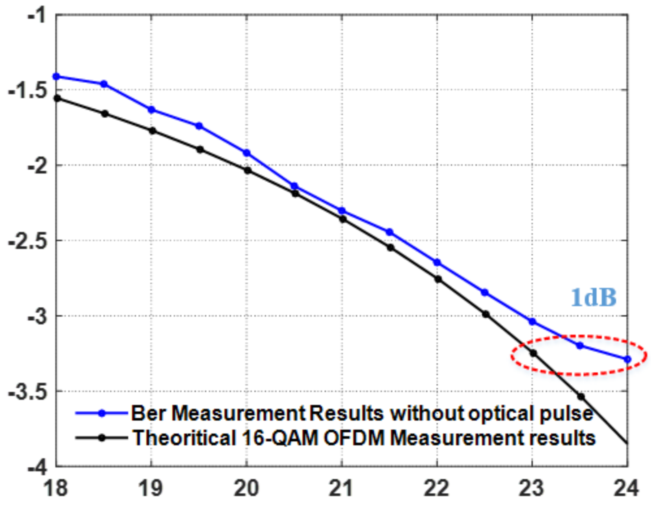

Fig. 3.7: OSNR versus BER for the 16-QAM OFDM transmission system over AWGN channel under simulation and experimental environment.

After that, the measurement is repeated in the presence of optical pulses. As explained above, additional phase rotation and intensity distortion would be introduced by the high-power optical pulse in the 'affected' frames. As illustrated in Fig. 3.8, the phase transition induced by high-power optical pulse is obtained by measuring phase distribution of pilot tone. About 0.8 rad is introduced within the optical pulse. Therefore, a phase compensation and low-pass filtering modules are required in addition to the conventional algorithms. However, it is quite difficult to estimate the phase noise influence during the transition edge. During the rising and falling time which is about 12ns each used in our experiment, optical power and the resulted phase and intensity noise are unstable and difficult to estimate which cause large amount of detection error.

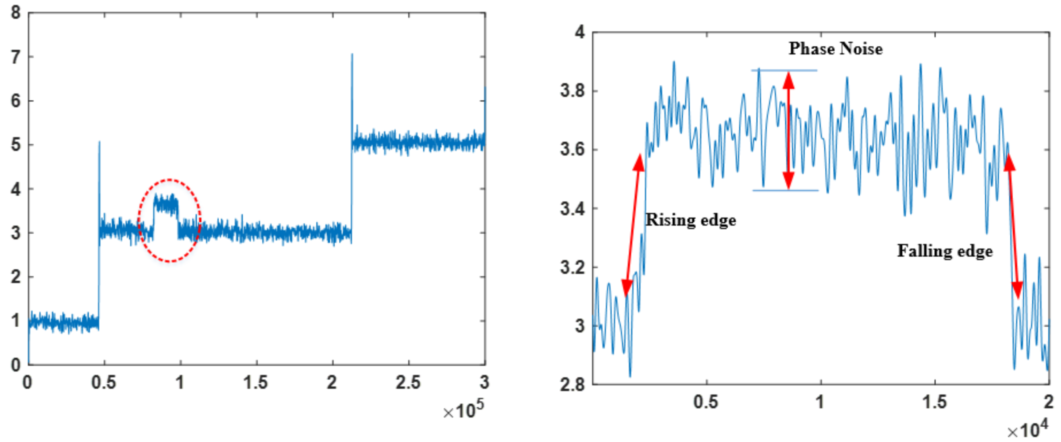

Fig. 3.8: Phase distribution of pilot tone and the influence of transition edge of optical pulse.

The OSNR verses BER of the measurement is shown as the blue curve in Fig.3.9. A BER of 3e-3 is obtained with OSNR of 22.5. The measurement is repeated in the presence of optical pulses used in sensing system under the same OSNR condition and the results is shown as the red curve in the figure. As explained above, additional phase rotation and intensity distortion would be introduced by the high-power optical pulse in the ‘affected’ frames. About 1 dB OSNR penalty is observed which could be ascribed to the inaccurate phase estimation in the top flat of affected frames as well as the influence of rising and falling edges of the sensing pulse.

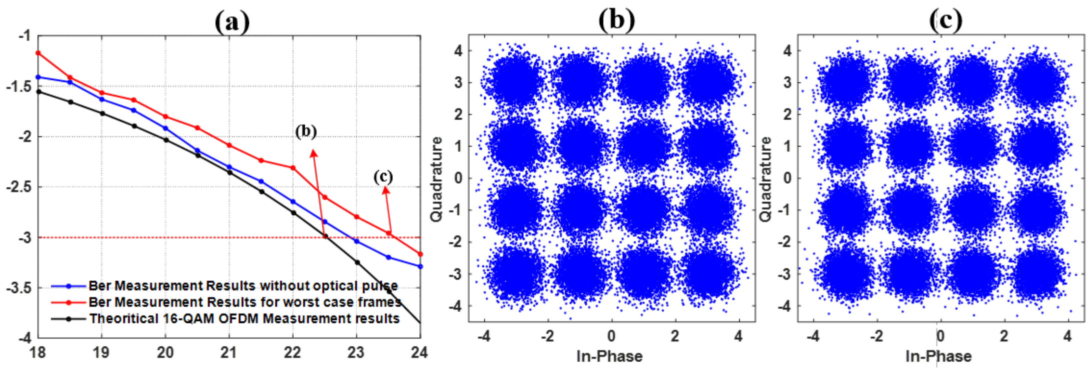

Fig. 3.9: OSNR versus BER for the 16-QAM OFDM transmission system over AWGN channel

Similarly, the influence of backscattered OFDM signal on the performance of the phase sensitive-OTDR system is also investigated. In the experiment, the reflected OFDM signal is merely -50dBm which is over 30dBm lower than the backscattered Rayleigh signal. therefore, the influence is negligible.

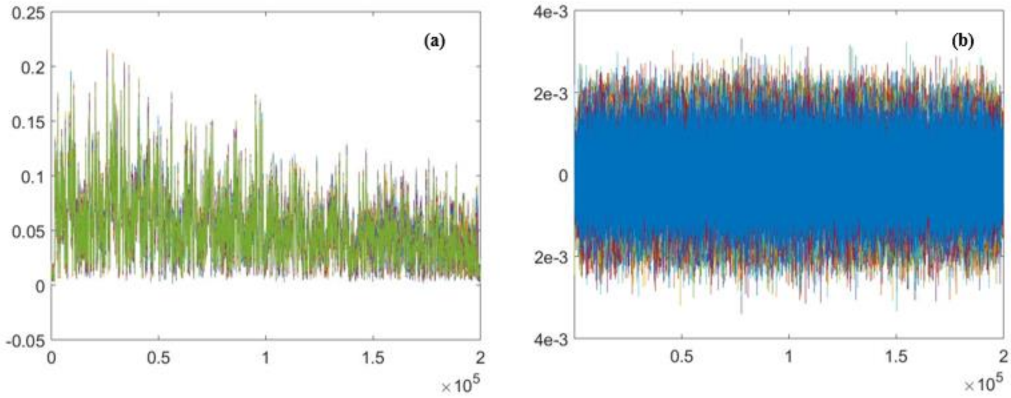

Fig. 3.10: (a) Superposition of the backscattered Rayleigh trace without applied vibration signal. (b) Differential signal of detected backscattered Rayleigh trace.

In phase-sensitive OTDR, the pulse width of used optical pulse is 200ns with a peak power of 18dBm. 250 traces of backscattered Rayleigh signal are recorded for each measurement. The collected measurement results are shown in Fig. 3.10. The differential signal is obtained by subtracting the adjacent traces. The intensity fluctuation of Rayleigh trace is about $2mv$ which could be largely eliminated using average.

At the end of FUT, 20 meters of fiber is wound around a PZT to apply vibration signal. In the experiment, 100 Hz sinusoidal signal is applied to stretch the fiber. Vibration measurement results are show in Fig. 3.11.

Moving differential method is used to analyze vibration signal i.e. comparing neighboring trace to analyze the variation. SNR is enhanced by using 10 times moving averaging on the successive differential traces. The location of vibration is clearly observed and SNR at the end of the fiber is about 6.5dB.

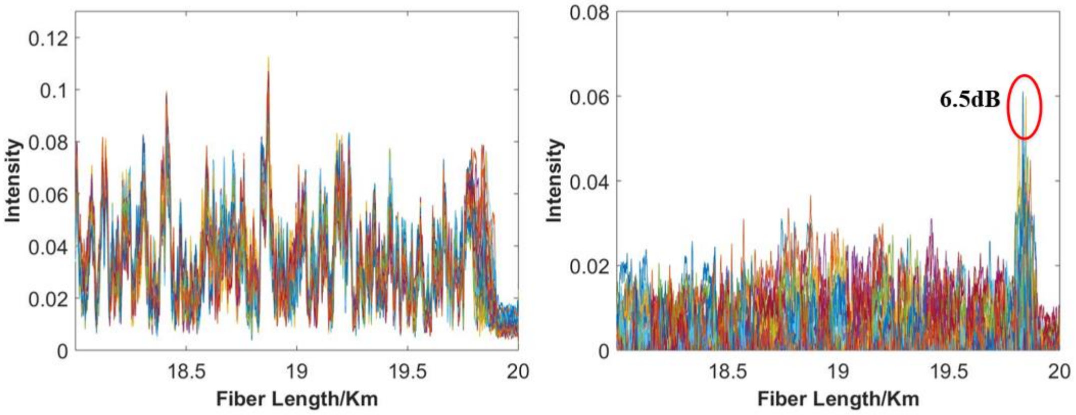

Fig. 3.11: (a) Superposition of the backscattered Rayleigh trace with 100hz sinusoidal vibration signal.

(b) Moving differential signal of detected backscattered Rayleigh trace.

In addition, the frequency response is analyzed to evaluate the detection range of the vibration signal frequency. The waveform of applied vibration is analyzed with I/Q demodulation method with the help of phase unwrapping. Detected traces at the located vibration point is analyzed by FFT. As displayed in Fig. 3.12(b), a frequency peak at 100 Hz is successfully observed which agrees with the applied signal.

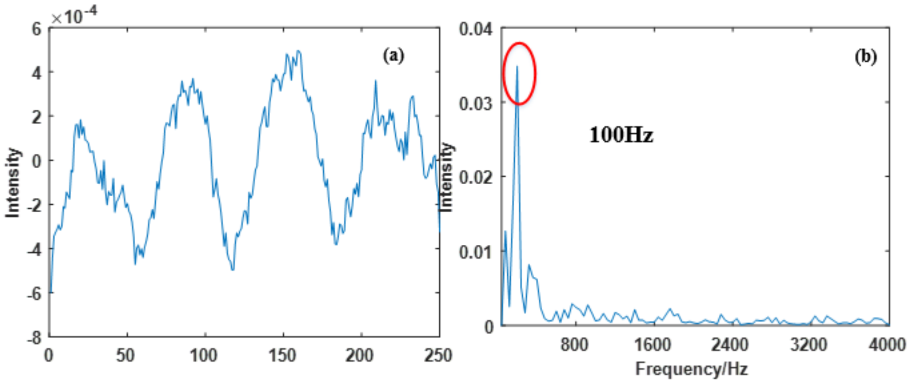

Fig. 3.12: the detected time-domain signal of PZT vibration (d) frequency component of the detected vibration signal.

3.5 Conclusions

In this chapter, an integrated communication and phase-OTDR sensing system with shared optical bandwidth is reported. OFDM modulation technique is selected and applied in our communication system as it is widely recognized as one of the major transmission techniques in optical communication systems with numerous advantages. In the system studied, 16QAM-OFDM signal at 112Gbit/s is transmitted over 20km SSMF. Meanwhile distributed phase sensitive-OTDR system is deployed to monitor the environmental variation along the fiber.

Equation Chapter (Next) Section 1

4 Scanning-free BOTDA based on Digital Optical Frequency Comb

In this chapter, the principle of scanning-free BOTDA based on digital optical frequency comb (DOFC) is described. The current progress of dynamic BOTDA sensor is reviewed first. Then, the principle of the proposed scanning-free BOTDA sensor system is discussed while the generation and demodulation algorithm of DOFC is given. Finally, the performance is analyzed in detail especially the measurement time.

4.1 State-of-the-art progress of dynamic BOTDA measurement

As discussed in chapter 2, the measurement time of conventional BOTDA is composed of four parts: time of flight of pump pulse, frequency scanning time, time of averages, frequency switch speed. The measurement time of BOTDA is normally in the order of few minutes, mainly owing to the requirement of scanning the probe frequency in Brillouin gain spectrum in order to locate the Brillouin frequency shift induced by temperature or strain along the fiber, which is time consuming and thus can not meet the requirement in the case of fast distributed monitoring system [69],[70]. So, BOTDA systems can only be used in slow analysis and static measurement till now. On the other hand, the possibility to extend the distributed optical fiber sensors to dynamic measurements would be of special interest in some application fields, such as measurement of vibrations in civil or aeronautic structures which require a monitoring response in the range of seconds or even less.

To alleviate mentioned limitations, several novel techniques have been investigated to improve the sensing speed of conventional BOTDA recently. Among them, the slope-assisted BOTDA manage to transfer the BFS variation to intensity fluctuation with simplified setup [71]-[73]. It provides convenience as well as efficiency without the need for frequency-sweep by compromising sensing range. Besides, a sophisticated sweep-free method is also proposed with a complicated configuration [74]-[76]. In this method, multiple probe and pump signal is launched in opposite direction simultaneously to detect each component of BGS. Fast-BOTDA (F-BOTDA) is also investigated with ultimately fast devices to eliminate the frequency switch time [77]-[79].

Slope-assisted BOTDA

Some of the adaptations to conventional BOTDA setup are proposed to realize fast BOTDA

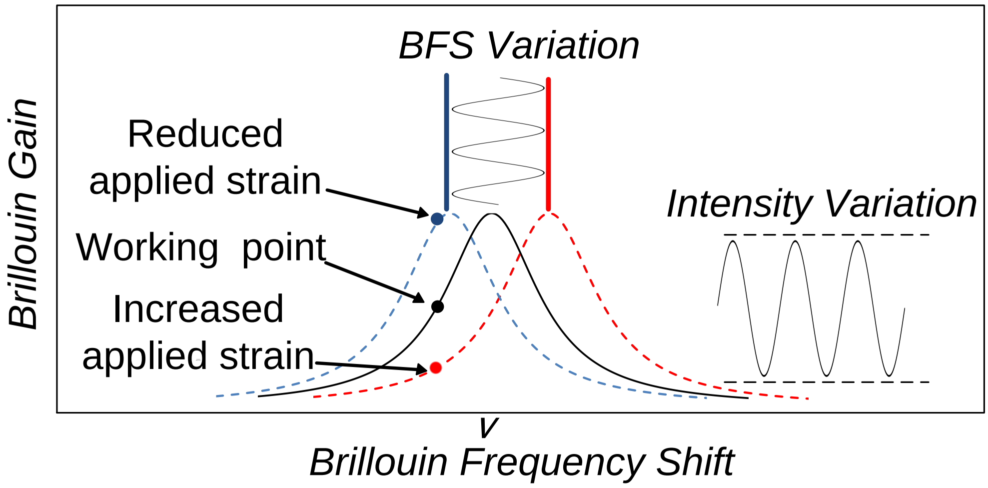

Fig. 4.1: The transfer of BFS variation to intensity fluctuation by BGS Slope-assisted BOTDA sensor.

by avoiding frequency sweep. One of these schemes is called slope-assisted BOTDA (SA-BOTDA). Rather than scanning a wide range of frequency to find the peak of BGS, a fixed probe-pump frequency difference is sitting at the skirt of BGS, was proposed in [71]. In this way, the shift of local Stokes frequency will be translated to the intensity variation of probe signal linearly. This intensity variation will reproduce faithfully the dynamic characteristics of vibration/temperature. By pulsing the co-propagating probe and pump waves, the interaction length is limited in the overlap area of both pulses. Distributed sensing can be achieved by properly adjusting the time delay between both pulses. Vibration frequency up to 98 Hz is successfully demonstrated by experiment with the proposed method.

A fully distributed SA-BOTDA capable of extracting intensity variation along the whole sensing distance with arbitrary Brillouin profile is proposed by replacing the pulsed probe with a CW [72]. Instead of using a fixed pump-probe frequency difference, the CW probe frequency is intentionally tailored according to the BFS distribution along the fiber to ensure that the optical frequency sits at the middle of the slope of the BGS at any position.

The first demonstration of this technique successfully measured a few hundreds of vibrations sensing at separate locations of an 85m fiber simultaneously with 1.5m spatial resolution.

Sweep-free BOTDA

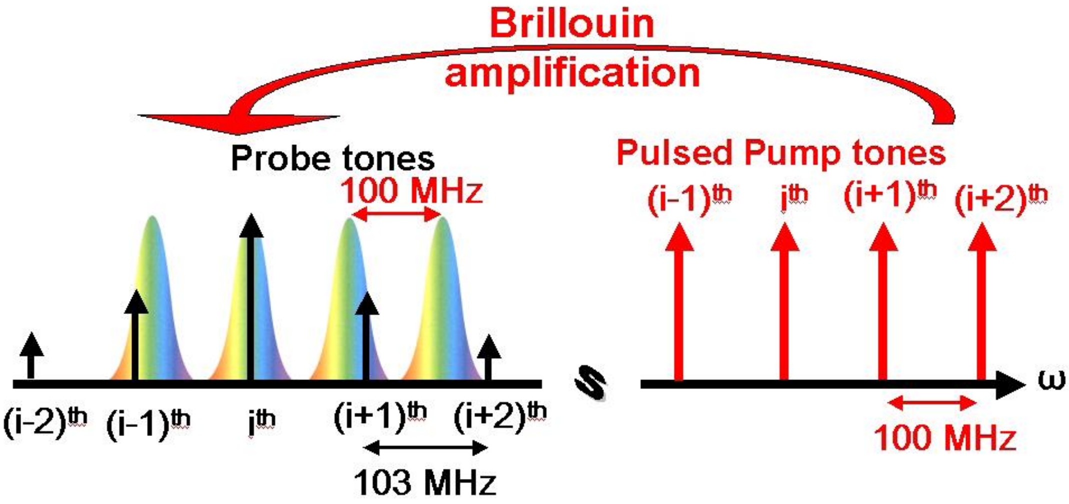

Fig. 4.2: Brillouin amplification using sweep-free concept using multiple pump and probe tones.

Sensing speed is enhanced by sophisticated sweep-free method. Here, multiple probe and pump signal is launched in opposite direction simultaneously [74]-[76]. The frequency difference of each probe-pump pair is arranged in a manner that each pair interrogate different part of BGS. In principle, the pump tones are pulsed as the classical implementation without compromising the spatial resolution. Once the individual gain experience by each probe tone amplified by corresponding pump is recorded simultaneously, the BGS can be recorded with a single acquisition. The number of probe-pump pairs and the frequency spacing between each pair jointly determine the frequency resolution and sensing range of BGS. Thus, the measurement speed of sweep-free distributed Brillouin time-domain analyzer (SF-BOTDA) is improved by a factor compared with conventional BOTDA, which can be as high as the number of pairs used in the scheme.

A SF-BOTDA of 63 MHz covering range and 3 MHz resolution using 21 probe-pump pairs is demonstrated experimentally, corresponding to a 21 times speed improvement compared with the frequency-sweep scheme.

The proposed method is improved by introducing the sequentially lunched pump tones. To alleviate the inter-tone modulation effects [76]. Strain variations with frequency up to 400 Hz are analyzed, achieving stain sensitivity of 1 micro strain.

Fast BOTDA

In addition to avoiding frequency sweep, various configurations are investigated to deal with other limiting factors. Recently, a fast-BOTDA (F-BOTDA) technique is introduced based on use an arbitrary waveform generator (AWG) which enable fast switch among 100 scanning frequencies. Compared with relatively slow electronic synthesizer, whose stabilization time is in the order of 1 ms per frequency, AWG with pre-programmed frequency signal can achieve a literally continuous frequency switch. By minimizing the switching time of frequency, a dynamic measurement with sampling rate of ~10 KHz is achieved limited only by fiber length and frequency granularity [77].

4.2 Scanning-free BOTDA based on DOFC

As analyzed in previous sections, majority of the measurement time consumed is the process of frequency scanning which is typically several hundreds of scanning steps. In order to improve the response time of conventional BOTDA sensor, we propose to use digitally generated optical frequency comb to realize ultra-fast Brillouin gain spectral analysis without frequency scanning and thus can be potentially used to realize a dynamic BOTDA. In our scheme, the conventional CW signal used to probe the BGS/BPS is replaced with a multi-carrier DOFC signal. In this way, we could fully map the complete

Brillouin profile in a single measurement.

4.2.1 Generation and demodulation algorithm of DOFC

The generation of DOFC

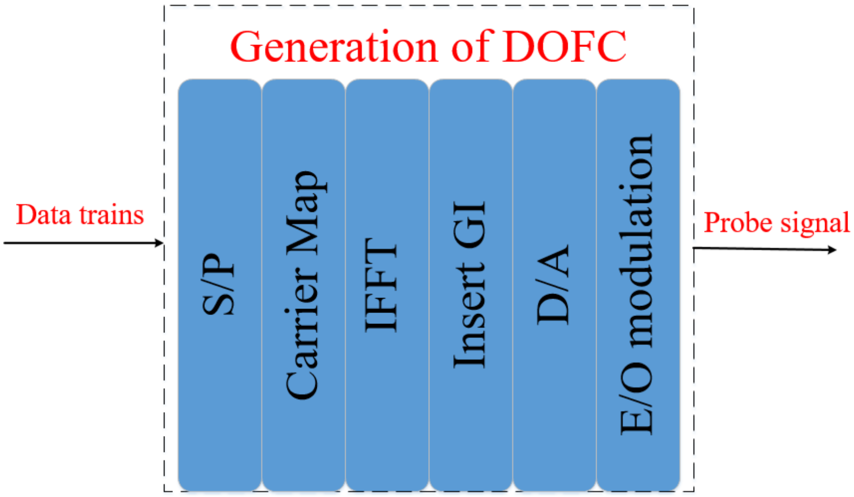

Fig. 4.3: Generation process of digital optical frequency comb. S/P: serial to parallel transition; IFFT: Inverse fast Fourier Transform; GI: Guard Interval; D/A: digital to analog conversion; E/O modulation: electrical to optical modulation;

The generation process of DOFS is shown in Fig. 4.3. A complex-value symbol train is generated in the software follow the criteria that the amplitude of each signal keeps constant while the angle of each symbol is random. It is achieved by defining a number of units and multiplied with randomly generated phase rotation term.

$$a_1, a_2 \ldots a_N = I \cdot \{\exp(j\varphi_1), \exp(j\varphi_2) \ldots \exp(j\varphi_N)\} \tag{4.1}$$

The purpose of this procedure is to avoid DC component as well as severe time domain signal intensity fluctuation after Inverse Fast Fourier transform (IFFT) which is referred as peak to average power ratio (PAPR). While higher PAPR value would deteriorate the amplification characteristics of electrical driver. Apart from that, the E/O modulation efficiency would also be affected as the liner transition part of optical modulator is limited.

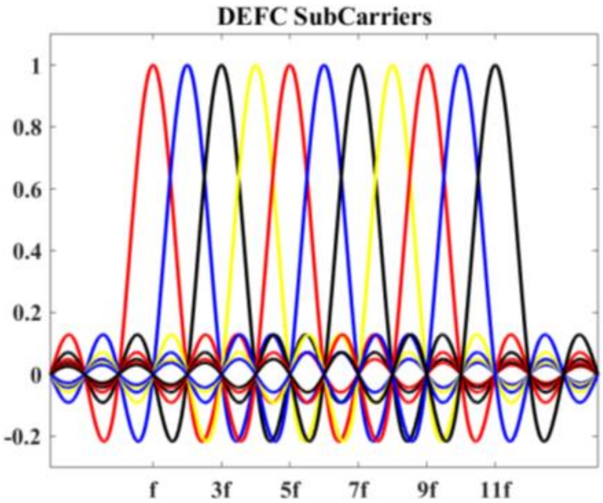

Fig. 4.4: Generated electrical frequency comb.

Then serial generated complex data train is converted to a parallel N block. N is the size of a parallel data block and must be 2^M . Then, the data block is mapped onto selected orthogonal carriers. As represented in Fig. 4.4, f is the frequency of of the fundamental carrier as well as the frequency resolution of frequency comb, while other frequency tones is defined as multiple integer of f to guarantee the orthogonality within the frequency comb. N represents the number of carriers used in DEFC or the number of teeth of the generated frequency comb. We are able to flexibly adjust the coverage frequency range by simply increase or decrease the carrier number. The defined subcarrier can be represented as:

$$f_m = a_m exp(jm\omega_0 t) \tag{4.2}$$

Where, a is the complex value and ω_0 is the angular frequency step. Then, the mapped independent carrier is fed into IFFT module to convert to the time domain signal block which can be expressed as:

$$s(t) = \sum_{i=-N/2+1}^{N/2} a_i \exp(j\omega_i t), \quad 0 \leq t \leq T \tag{4.3}$$

Where, T is the duration length of time domain frame and $\omega_i = i \cdot \omega_0$. Afterwards, the guard interval (usually use the last 1/32 of the time domain signal or zero padding) is supplemented at the tail of the block. Now, a complete electrical frequency comb frame is constructed. The D/A process is achieved using arbitrary waveform generator (AWG). Analog signal at the output of AWG is amplified to drive the E/O modulator. In this way, the DOFC is generated. The structure of generated DEFC frames is shown in Fig. 4.5.

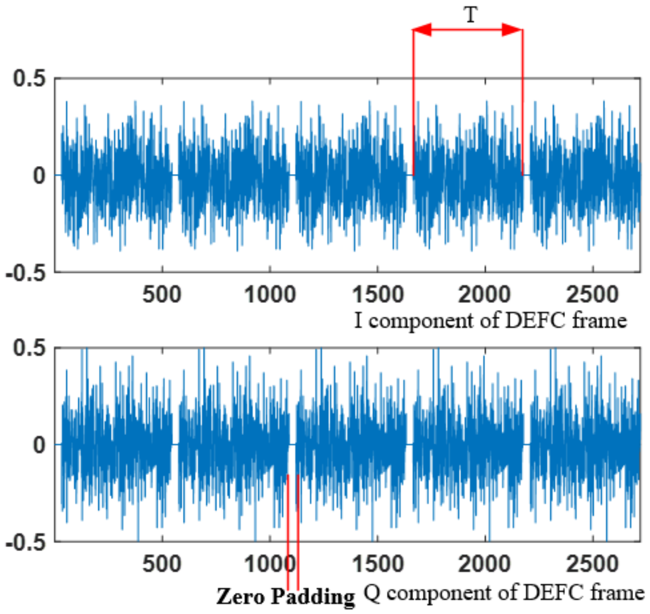

Fig. 4.5: Structure of generated DEFC frames. (a) real part of DEFC frames (b) Quadrature part of DEFC frames.

According to property of IFFT, the operation sampling rate of AWG f_s ,defines the minimum time interval of the time domain samples t_s. Therefore, the frequency coverage range of DOFC is dependent on the sampling rate of AWG. While the frequency gap between each tooth of DOFC calculated as $f = {f_s}/{N}$. In our scheme, f_s and ${f_s}/{N}$ corresponding to the frequency scanning range and frequency scanning step, respectively.

We can conclude that, increase the size of IFFT N would improve the frequency resolution i.e. the frequency gap between tooth of DOFC and increase the duration length of the time domain block T. In other words, duration length of DOFC frame T is inversely related to the resolution of frequency comb —the finer frequency resolution, the longer duration length. The limitation of T will be explained in the following part.

The demodulation of DOFC

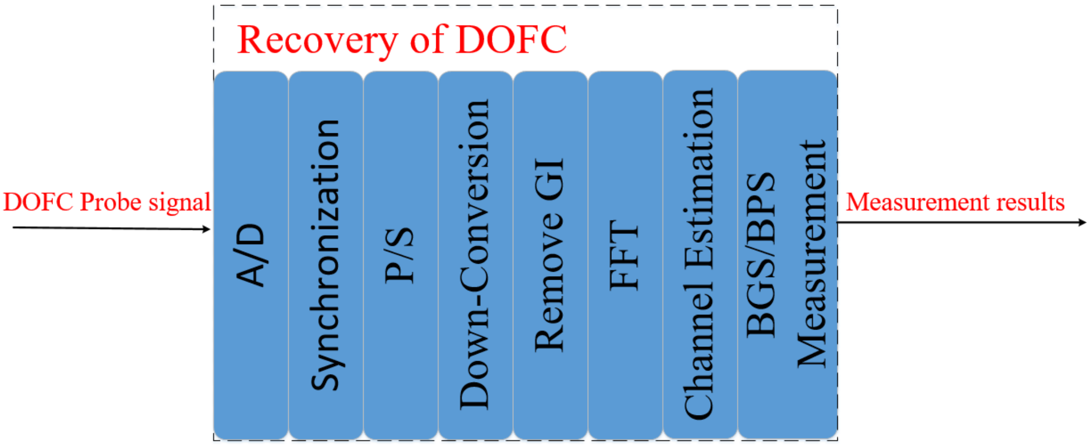

Fig. 4.6: Demodulation process of digital optical frequency comb. A/D analog to digital conversion; P/S: parallel to serial transition; FFT: Fast Fourier Transform;

Generated DOFC probe signal is transmitted in the FUT and amplified by counter-propagating pump signals. The complete Brillouin amplification profiles is recorded by the DOFC probe.

At the receiver end, the transmitted DOFC probe signals can be detected using coherent or direct detection method. In the following equations, coherent detection method is assumed for simplicity. The intensity and angle of the multi-carrier probe are fully mapped and digitalized with a high-speed oscilloscope. Then, collected signals is further processed offline to extract the ‘modulated’ channel response during stimulated Brillouin interaction.

$$E_s = \sum_{i=-N/2+1}^{N/2} a_i \exp(j\omega_i t) \cdot H(\nu) \cdot H_{SBS}(\nu_i) \tag{4.4}$$

Where $H(\nu)$ is the overall channel response of the fiber and $H_{SBS}(\nu_i)$ is the complex Brillouin gain spectrum. The demodulation process could be divided into several independent parts including synchronization, parallel to serial transition, frequency down-conversion, FFT and channel estimation.

Algorithms for accurate timing estimation

In the first step, synchronization algorithm is used to locate the duration position of each DOFC frame. As we know, the DOFC frames, each with a duration length of several hundred milliseconds, propagate in the FUT consecutively with Guard interval is inserted between each frame. The synchronization algorithms are fundamental for optical communication systems and have been investigated in depth for several decades. Most of these methods involve adding a predefined synchronization head with specified patterns in front of data frame which is used for correlation-based timing estimation. However, the arrangement would inevitably introduce extra overhead.

Besides, the most straightforward method to realize the location process is to calculate the correlation between transmitted frame with obtain ones. Peak of the correlation values indicates the starting point. But the signal pattern is distorted during transmission in the fiber due to non-uniform channel response which in turn distort the correlation value and lead to large estimation errors. Therefore, we have developed specific synchronization algorithm for accurate timing estimation. The basic operation principle is explained in the following. As the initial phase matrix θ_t for transmitted symbol $a_1, a_2 ... a_N$ is known. We can calculate the phase relation between each subcarrier θ_r. After transmission in the FUT, the absolute phase of transmitted symbol is shifted by an undetermined factor while the inter-phase relation θ_r' is to a large extent constant (though not completely stable). Then, we can calculate the correlation between θ_r and θ_r'. The benefits of this method are that it largely immune to the distortion of frequency offset between laser source and LO and thus relieve the requirement of accurate frequency offset compensation. As shown in Fig. 4.7, a correlation peak up to 10 dB of contrast is observed using the described method.

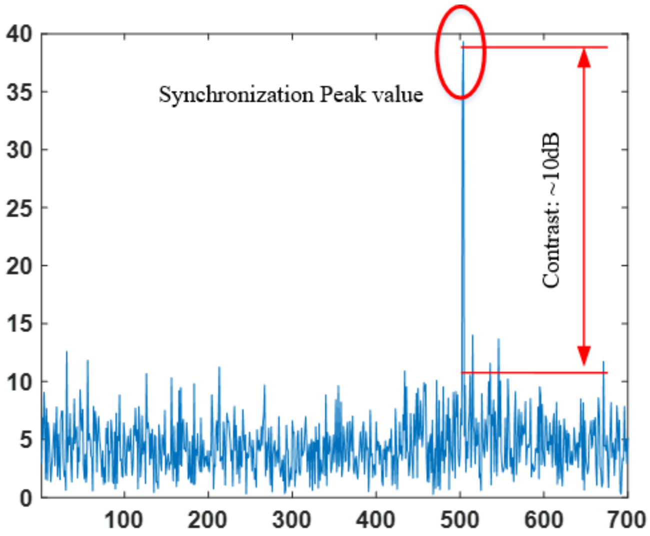

Fig. 4.7: Correlation peak of synchronization process.

Carrier frequency offset compensation

In the coherent detection, though derived from the same laser source, slight optical frequency difference still exists between DOFC probe and LO. Depending on the frequency drift of laser source combined with the length of FUT, up to several tens MHz of frequency offset is observed in our experiment. In general, a pilot tone is inserted to the DOFC signal to evaluate the influence of frequency offset. As the BFS measurement is based on the characterization of frequency response of each specific frequency tone of DOFC, a shift of frequency component would lead to a fault measurement result.

A single frequency pilot tone signal is added to the time domain DEFC signal and up-converted to optical domain multi-carrier probe signal. frequency of pilot tone is set at

1.1GHz to avoid overlap with the coverage range of probe signal.

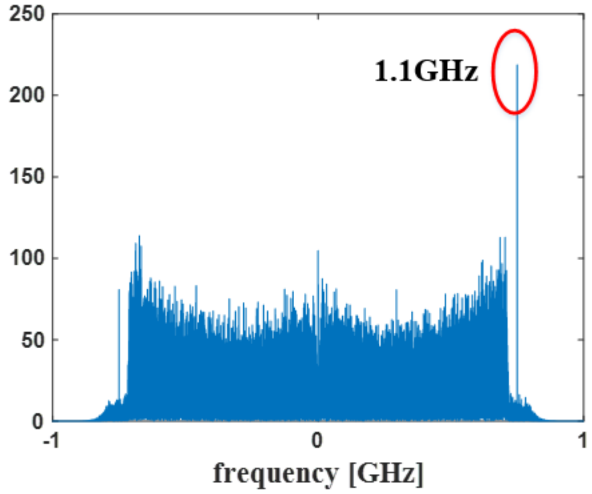

Fig. 4.8: The pilot tone of 1.1Ghz to evaluated frequency offset.

Then the serial time domain DOFC frames are separated and transformed to parallel blocks and GI is removed. The remaining N samples are fed into the FFT module to convert back to the frequency domain. Obtained N subcarriers are compared with the transmitted signals $\{a_1, a_2 ... a_N\}$ by simply dividingE_s by $s(t) \cdot H(\nu)$:

$$H_{SBS} = {}^{E_s}/_{s(t) \cdot H(\nu)} \tag{4.5}$$

The overall channel response $H(\nu)$ is first measured. Without introducing the pump signals, the DOFC probe signal in FUT do not experience any amplifications. Therefore, the measured result $H(\nu)$ is the overall channel response of the complete transmission system including the process of electrical signal amplification, E/O modulation and fiber transmission. By taking a large number of averages, accurate estimation of the transmission matrix $H(\nu)$ is obtained which function as a reference for subsequent measurement.

Taking the existed channel response into account, the calculated result $H_{SBS}(\nu)$ directly reflects the Brillouin amplification characteristics e.g. the BGS and BPS. Of course, a number of averages is required to reduce the influence of noise. Specifically, the intensity represents the gain profile and the phase shift is the Brillouin phase shift profile.

4.2.2 Sensing principle of BOTDA based on DOFC

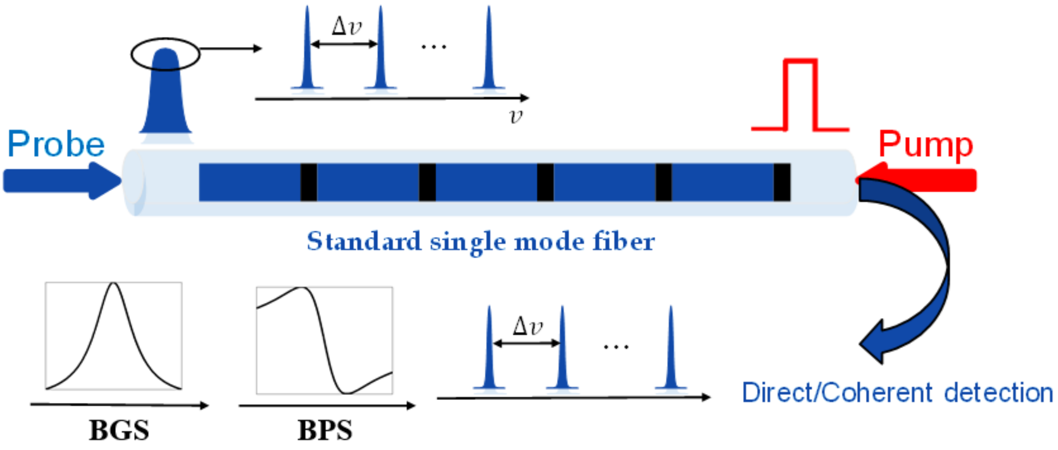

Fig. 4.9: Schematic representation of the principle of DOFC based BOTDA.

The measurement principle of proposed DOFC base BOTDA is illustrated in Fig. 4.9. In conventional BOTDA implementation method, the frequency of CW probe signal is swept one by one and the intensity/phase trace for each probe signal is recorded. Combining the whole transmission characteristics for each CW probe with different frequency, the Brillouin gain/phase profile is recovered. While, instead of using a single tone probe signal as in conventional BOTDA, wideband frequency comb probe frame is launched into the fiber under test (FUT) at position $z = 0$, while a single tone pump is introduced from the opposite direction at position $z = L$. The center frequency of the probe and pump signal is separated by about 11GHz depending on the typical BFS value of used fiber to excite the stimulate Brillouin interaction. It must be emphasized that, the parameter of frequency gap $\Delta\nu$ and frequency range must be carefully designed. The inverse relation between $\Delta\nu$ and DOFC frame duration length T exists:

$$\Delta\nu = {}^{1}/_{T} \tag{4.6}$$

The finer the frequency resolution used in the system the longer of the frame width. Here, the interaction process for the proposed DOFC based BOTDA sensor must be explained in detail. As described in previous section, the generated DOFC probe frame is injected into the fiber continuously and consecutively to interact with pump signal. The coverage of each frame is T as blue area indicated in the figure, dependent on the duration length. Then, each frame interacts with the counterpropagating pump pulse in sequence at different position. Hence, the interaction area is $\frac{T+T_{pump}}{2}$. Within the interaction area, the spectrum of DOFC probe signal is reshaped by pump signal and the BGS and BPS are recorded simultaneously without the need for frequency scanning.

At the receiver, the optical probe signal is detected with direct/coherent detection method. Then, the offline signal processing method discussed before is used to extract the carried information of probe signal. By analyzing the complex transfer matrix of DOFC frames, the environmental properties along the fiber such as temperature and strain distribution can be obtained accordingly. At the same time, the location of measurand is also realized which is corresponding to the position of DOFC frame. In summary, the spatial resolution is not only related to the pump pulse width as in conventional BOTDA but dependent on both the width of probe and pump pulse.

BGS/BPS curve fitting for DOFC based BOTDA system

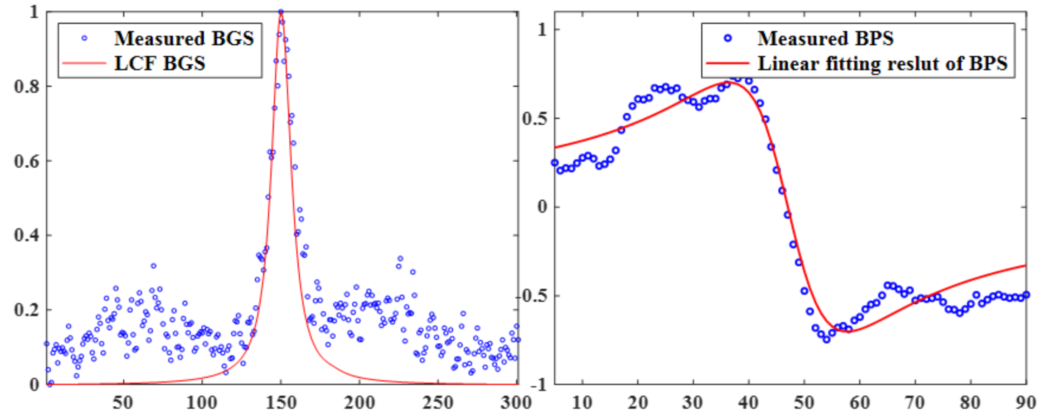

Fig. 4.10: LCF curve fitting result for BGS measurement and linear fitting result for BPS measurement using DOFC based BOTDA sensor.

The blue circle in the figure indicates the measured SBS intensity and phase response for different frequency shift, respectively. Longitudinal axis represents the frequency tone index of (e.g. frequency difference between probe and pump) measured Brillouin gain and phase spectrum. Large fluctuation is observed for the raw data due to the noise. With the LCF method, the peak of the gain spectrum is located which is corresponding to the induced BFS. For the phase shift profile, linear fitting method is used to find the center of the spectrum. The center of BGS/BPS indicate the BFS value. And the measurand is determined based on the BFS value using the linear dependence coefficient.

With the same procedure, we can determine the BGS/BPS distribution along whole fiber under test. As shown in Fig. 4.11, the sequence of frame represent for the location in the fiber as DOFC frames is recorded in chronological order. Each frame covers a measurement length of 51.2meter. It is easily locating the distance of event by calculating the sequence number of DOFC frames.

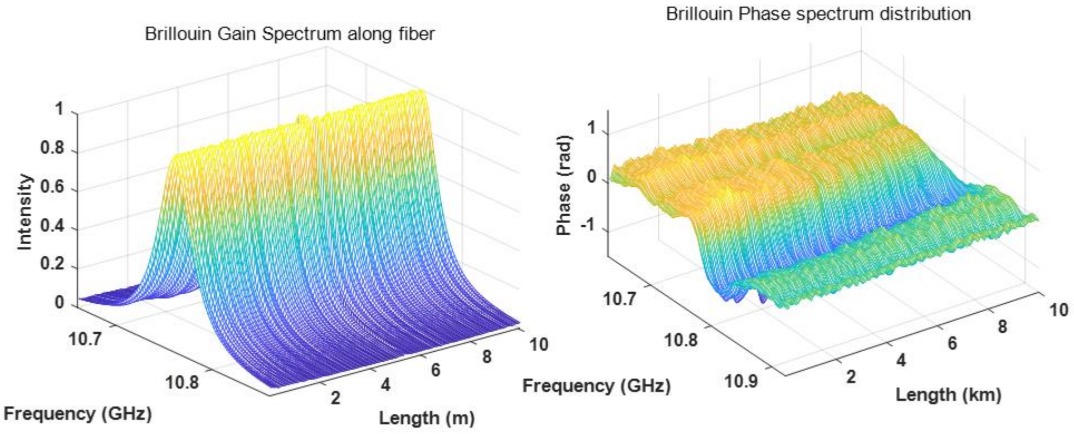

Fig. 4.11: Distribution of measured BGS and BPS along fiber.

4.3 Performance analysis of BOTDA sensor based on DOFC

4.3.1 Power distribution of generated DOFC

As explained in chapter 4, the efficiency of SBS is proportional to the local Brillion gain coefficient $g_B(\nu)$, power of probe signal P_{si}, power of pump signal P_{pi} and the interaction light Δz. In other words, the power transferred from pump to probe signal is higher if intense probe signal is used. The resulted Brillouin amplification profile would be biased if power of probe signal P_{si} is non-uniform. For the above-mentioned considerations, the frequency comb signal with the power uniformly distributed among each frequency tone is generated.

However, the power fluctuation between each frequency tone is observed at the back-to-back verification experiment. As explained previous, generated DEFC is programmed in the AWG in advance. Then output of AWG is used to drive the EOM through an electrical driver to generate DOFC which is subsequently directly detected by coherent receiver without going through any device or fiber.

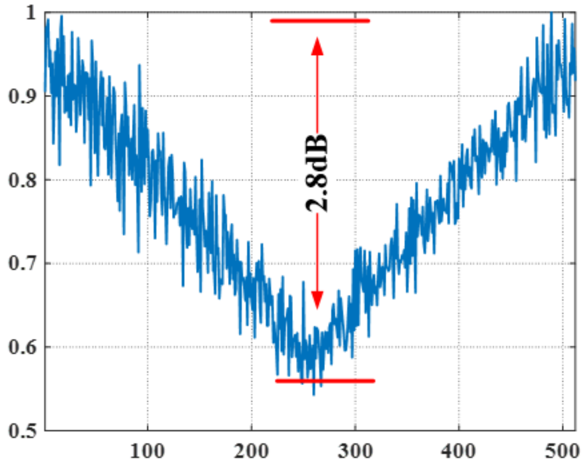

Fig.4.12: Illustration of the power difference between generated DOFC signal.

As shown in Fig. 4.12, a drop of the power distribution is clearly observed with power degradation of 2.8dB. Horizontal axis is the carrier index of the DOFC signal, and the detected intensity is normalized. In the middle of the carrier index which corresponding to the higher frequency, the detected intensity drops to about 60% of the intensity at baseband frequency. This could be ascribed to the amplification characteristics of driver and modulation efficiency of EOM. To be specific, the electrical driver used in experiment is commonly not uniform. The amplification gains drop with the frequency of input RF signal. Besides, the modulation efficiency of electro-optic modulator is also not linear for different frequency components

Power compensation using pre-equalization algorithm

- Frequency domain pre-equalization algorithm

The drawbacks of non-uniform power distribution of DOFC is obvious. To alleviate the power fluctuation, we propose to use pre-equalization algorithm to compensate the power difference. Basic operation idea of this method is simple. Power transmission matrix of the modulation process can be modeled as H_m. Estimation of the matrix can be represented as:

$$H_m = \begin{Bmatrix} a_1 & & a'_1 \\ a_2 & & a'_2 \\ \vdots & \cdot/ & \vdots \\ a_N & & a'_N \end{Bmatrix} \tag{4.7}$$

Then the transmitted samples are compensated in advance with the pre-equalization matrix. In this way, the power loss would be fully compensated. As shown in Fig. 4.13, the detected power distribution after pre-equalization is nearly uniform with a power difference of less than 10%.

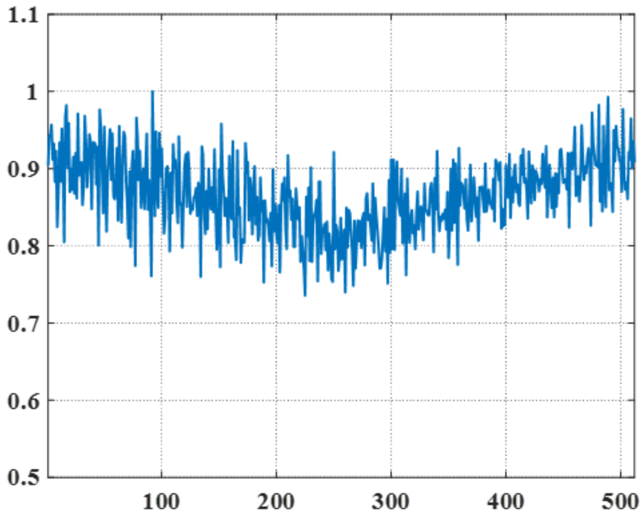

Fig. 4.13: Illustration of the power difference between generated DOFC signal with pre-equalization.

- Time domain pre-equalization algorithm

Except for the frequency domain pre-equalization algorithm, the power equalization method using time domain signal processing algorithm is also investigated. In the ultra-sensitive fading communication channels, the orthogonality between each carrier of DOFC could be seriously distorted by inter-symbol interference and the power inequality is also affected. The time domain pre-equalization combined with time domain channel impulse response estimation algorithm is an effective way for alleviate the discussed problem.

The proposed method first calculates the estimation of channel impulse response $h(t)$ on the separated sampling time. The corresponding effective coefficients for the constructed pre-equalization filter is determined based on the obtained channel impulse response $h(t)$. Following the minimum mean square criteria, the number of taps is selected to guarantee the best approximation of DOFC frames with even power distributions.

4.3.2 Measurement accuracy and spatial resolution

SNR and measurement error

The measurement error of BFS is dependent on SNR, frequency scanning step δ and full-width at half maximum (FWHM) $\Delta\nu_B$ of the Brillouin spectrum. In the system under study, SNR of acquired Brillouin gain trace is defined as the ratio between the maximum gain and the stand deviation of the random distributed noise. The relation can be simplified as:

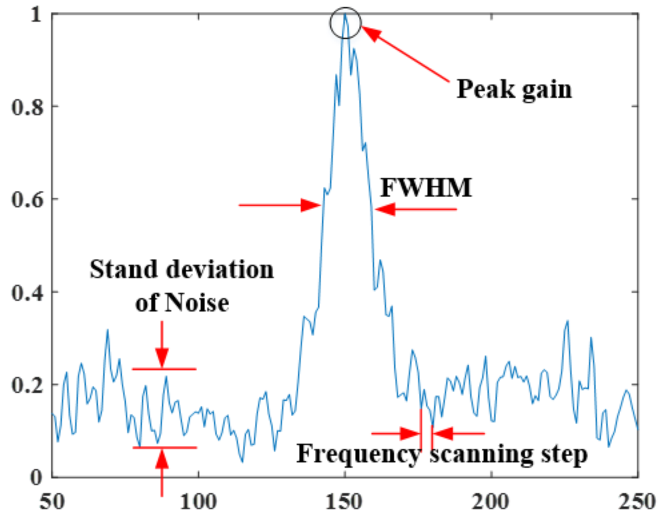

Fig. 4.14: SNR and measurement error.

$$\sigma_\nu = \frac{1}{SNR}\sqrt{\frac{3}{4}\delta\Delta\nu_B} \tag{4.8}$$

Where σ_ν is the estimated error of the measured BFS. It can be shown from the equation, the measurement accuracy can be improved with narrower frequency tone gap δ.

Trade-off between spatial resolution and frequency resolution

The inverse relationship between the spatial resolution and the frequency resolution is clarified in the section measurement principle. Trade-off between these two parameters is inevitable during the design of the proposed system. For example, if the required frequency resolution of the BOTDA sensing system is 2MHz, then the best spatial resolution is 50 meters. Detailed values are listed in Table 4.1.

Table 4.1 Typical values of spatial resolution and frequency resolution

Spatial resolution (m)	100	50	25	10
Frequency resolution (Mhz)	1	2	4	10

4.3.3 Measurement time

Factors limiting the response speed of conventional BOTDA is summarized in previous chapter including time of flight of pump pulse, frequency scanning time, time of averages and frequency switching speed. The performance in terms of measurement time of the proposed DOFC based BOTDA system is compared with the conventional BOTDA in detail in the following. Under the same conditions i.e., the comparison is draw with the same fiber length, frequency scanning step, frequency range and number of acquired traces. As the round-trip time for pump pulse is the same and the number of acquisitions is equal, the time needed is identical. Then, the number of frequency scanning is defined by $\nu/_{\Delta\nu}$. For example, if the required frequency scanning step is 1MHz over 1GHz range, the resulted scanning number is 2^{10} . However, DOFC based BOTDA system is capable of finishing this process in a single measurement. The frequency coverage range is only limited by the sampling rate of D/A device used. In conclusion, the measurement speed of DOFC based BOTDA sensor is improved by $\nu/_{\Delta\nu}$ compared with conventional BOTDA. Equation Chapter (Next) Section 1

5 Ultra-fast BOTDA based on direct detection of DOFC

In this chapter, an ultra-fast BOTDA sensing system based on direct detection of DOFC probe signal is proposed and demonstrated experimentally. The frequency spacing and coverage bandwidth for the DOFC used is 1.95-MHz and 2-GHz, respectively. The DOFC can be used to reconstruct the Brillouin gain spectrum (BGS) and locate the Brillouin frequency shift (BFS) without frequency scanning and thus can improve the measurement speed about 100 times compared with the conventional BOTDA. This scanning-free BOTDA system has also been demonstrated experimentally with 51.2-m spatial resolution over 10-km standard single mode fiber (SSMF) and with resolution of 1.4°C for temperature and 43.3με for strain measurement respectively.

5.1 The potential of dynamic BOTDA systems with DOFC

As we discussed in previous sections, the requirements for high-speed DOFS systems capable of distributed monitoring of temperature and strain change along the fiber in a few seconds or even lower has driven the research areas to investigate the properties of various dynamic DOFS system [80]. Among them, BOTDA system has shown a promising prospect in many application scenarios. However, in conventional BOTDA system, acquisition time is normally in the order of few minutes, mainly due to the need for scanning pump-probe frequency difference to reconstruct the Brillouin gain spectrum and locate the Brillouin frequency shift induced by temperature or strain along the fiber. This process is rather time consuming and thus cannot meet the requirement in the case of fast distributed monitoring system [69],[70]. Hence, BOTDA systems have been limited to slow analysis and static measurement till now. On the other hand, the possibility to extend the distributed optical fiber sensors to dynamic measurements would be of special interest in some application fields, such as measurement of vibrations in civil or aeronautic structures which require a monitoring response in the range of seconds or even less. One of the main methods to realize the real time BOTDA system is based on avoiding the scanning of the probe signal.

Recently, several adaptations are proposed to realize the frequency scanning-free BOTDA system. For example, slope-assisted BOTDA is realized based on tuning the frequency of probe optical signal to the half of BGS. In this way, BFS can be mapped as intensity variation of Stokes pulse [71]-[73]. However, the dynamic range of strain measurement using this scheme is limited by the linear range of BGS. Another scheme is proposed using the polarization dependence of the Brillouin gain. In recent year, another kind of scanning-free BOTDA is proposed based on multiple probe and pump signal pairs, the frequency difference of each signal pairs lies in different position of BGS, so allowing for the fast measurement of strain/temperature change along the fiber [74]-[76]. A modification of this scheme can be realized based on only single pump signal but comprising multiple frequency tones. The number of pump-probe pairs is finite due to the bandwidth of BGS and frequency spacing of pump and probe signals, and thus the measurement range and resolution cannot be optimized simultaneously for this scheme.

Optical frequency comb has already found important implementation in precise metrology and many other applications [81][82]. In this section, we demonstrated an ultra-fine and fast BOTDA system with DOFC without frequency scanning and thus can be potentially used to realize a fast BOTDA. In our experimental, 51m spatial resolution is successfully demonstrated over 10km standard single mode fiber. The resolution and range are 1.5°C and 30°C for temperature measurement respectively. The resolution and range are 43.3με and 900με for strain measurement respectively.

5.2 Principle and experimental setup

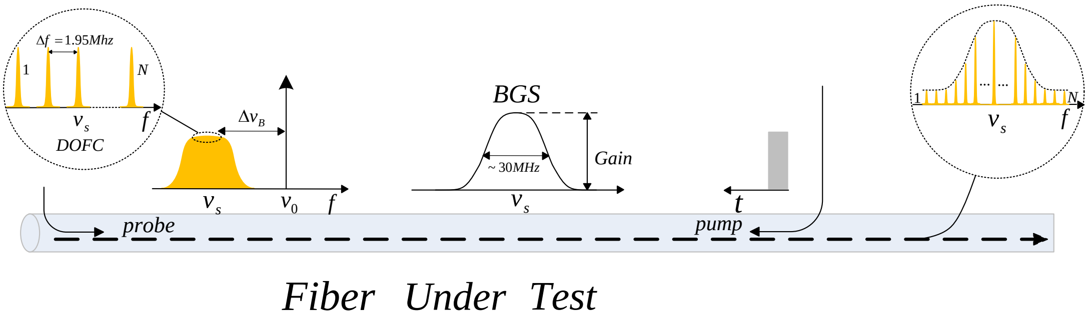

Fig. 5.1: Schematic representation of the principle of DOFC based BOTDA.

In the proposed frequency sweep-free BOTDA sensing scheme, DOFC is used as probe to detect BGS and locate BFS. The sensing principle is illustrated in Fig. 5.1. A wideband pulsed DOFC signal at 1550nm is launched into the FUT as probe, while a single tone pump signal is introduced from the opposite direction. The frequency of DOFC probe signal and pump is seperated by modulation method. By mixing with a RF signal, baseband DOFC is converted to the corresponding high freuqnecy band which is around the typical BFS value (~11 GHz) in single mode fiber with a frequency range of 1GHz. As shown in Fig. 5.1, the multi-tone optical signal distribute symmetrically around setted RF freuqncy value, and it has a flat top within the Brillouin linewidth. After interacting with pump signal in the FUT, the spectrum of DOFC probe is reshaped by frequency selective Brillouin amplification induced by SBS process. Therefore, the distributed BFS can be obtained by detecting the corresponding digital electrical frequency comb (DEFC) after photo detection, and the environmental properties around the fiber such as the temperature and strain can be recorded accordingly.

The generation and demodulation of process of DEFC is slightly different from the one explained principle in chapter 4. The process is shown in Fig. 5.2. A proper real-valued train of data with unit amplitude is generated in the software. Then, the generated real-value data is transformed to digital electrical frequency comb by 1024-point IFFT module. The digital to analoge conversion is realizdd by fedding into an AWG operating at the sampling rate of 2G Samples/s. In this way, a frequency comb of 1.95MHz span and 2GHz coverage range is generated. Each base-band DEFC frame is separated by a Guard Interval (GI) to avoid inter-frame distortions before up-converted by mixing with 11 GHz sinusoidal wave to cover the BFS range in the distributed sensor system. We must make clear that the duration length of DEFC frame T is inversely related to the resolution of frequency comb $\Delta \mathrm{f}$ —the finer frequency resolution, the longer duration length.

$$T = \frac{1}{\Delta \mathrm{f}} \tag{5.1}$$

Through electro-optic modulation, a optical frequency comb signal is obtained with the same frequency span and resolution as DEFC. After SBS process in the FUT, the DOFC signal is detected with a wide-band photodiode. The beating signal between optical carrier and the upper sideband which is generated by the same laser through electro-optic modulation is collected. While the lower sideband is filtered out in order to eliminated distortions. Processing methods includ frame synchronization, frequency down-conversion and FFT. The demodulation process is roughly the same as those disscussed in chapter 4. The duration location is determined use the synchronization method. Then the mixing RF signal is eliminated with a digital down-conversion process. FFT module is applied subsequently to transform the time domain signal back to freuqncey domain. Finally, DEFC frames are demodulated to analyze the amplification information carried on each frequency comb line, i.e. the BGS.

Unlike the conventional BOTDA, the location principle of DOFC-BOTDA is based on consecutive but separated DEFC frames. Each frame, collected by oscilloscope chronologically, contains the information of peak gain frequency of a section of fiber it covered. In this way, the spatial resolution of the system is limited by the duration length of frame. For example, a DEFC frame with duration length of 50ns corresponds to a spatial resolution of 5 meters.

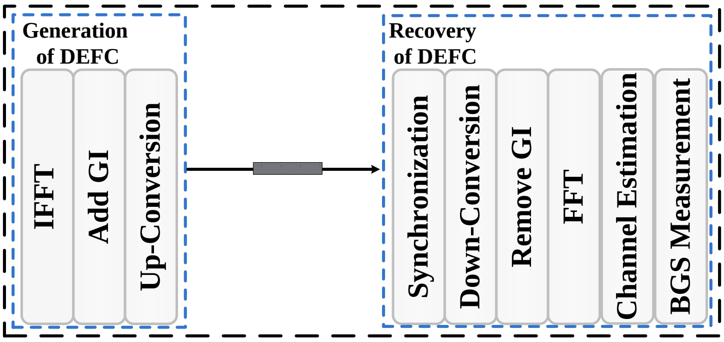

Fig. 5.2: Generation and demodulation of digital electrical frequency comb. IFFT: Inverse fast Fourier Transform; FFT: Fast Fourier Transform; GI: Guard Interval.

Fig. 5.3 shows the power spectrum of the generated baseband DEFC, which are orthogonal multi-carrier signal. It is worth noting that the frequency range of DEFC is limited by sample rate of AWG. In configuration adopted, most of the power is distributed within the range of 1GHz. The power spectrum within 1GHz is flat, and the power densities beyond this range drop dramatically, which is beneficial to the noise resistance capability. In the study, 1024 subcarriers each carried with unit amplitude signal is inversely transformed to time domain by IFFT, generating an orthogonal multi-carrier signal. The

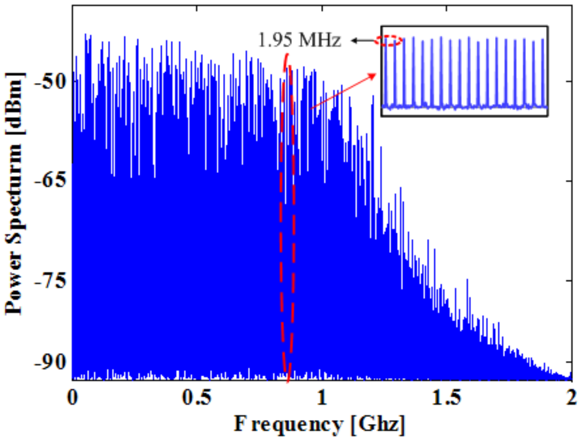

Fig. 5.3: Power spectrum of digital electrical frequency comb.

inset picture in Fig. 5.3 shows the zoomed view of the generated DEFC with frequency spacing of 1.95MHz (2GHz/1024), corresponding to a temperature/strain resolution of 1.5°C/43.3με respectively. Here, the frequency spacing of DEFC can be further reduced by increasing the length of IFFT.

5.3 Experimental setup and results

Experimental setup

The experimental setup of the scanning-free BODTA based on DOFC is shown in Fig. 5.4. In this experiment, a tunable laser operating at 1550nm with 100 kHz linewidth is split into two parts to serve as pump and probe signal respectively by using a 50/50 optical coupler. For the probe signal, the baseband DEFC is first up-converted to 11GHz by mixing with an 11GHz RF signal using a RF mixer in order to cover the whole BGS, as shown in the inset (b) of Fig. 5.4. It can be seen that the bandwidth of the DEFC become 2GHz from 1GHz after the frequency up-conversion. The duration length of each DEFC frame is 512ns, corresponding to spatial resolution of 51.2m. The up-converted DEFC is then modulated onto a laser through a Mach-Zehnder modulator (MZM) biased at quadrature point to generate double sideband DOFC, as shown in the inset (c) of Fig. 5.4. The DOFC is amplified by an EDFA and then pass through the FUT for distributed Brillouin interaction with the pump signal. In this process, the environmental properties around the fiber, such as the temperature and strain are recorded on the amplitude, phase and polarization of each frequency comb line of DOFC.

For the pump signal, ordered electrical pulse trains generated from the pulse generator is modulated onto the pump laser through a high extinction ratio optical intensity modulator biased at null-transmission point. In this way, the optical pulse of 100ns width

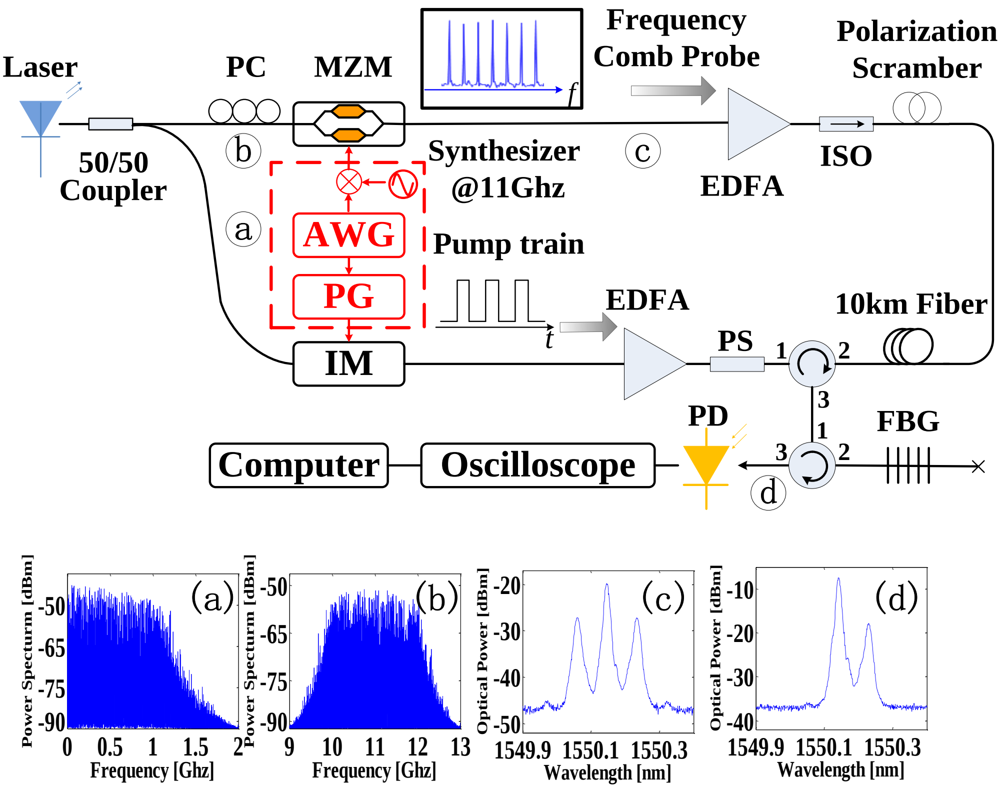

Fig. 5.4: Scanning-free BOTDA experiment Setup. AWG: arbitrary waveform generator; MZM: Mach-Zehnder modulator; EDFA: erbium-doped fiber amplifier; OSA: optical spectrum analyzer; ISO: isolator; PG: pulse generator; IM: intensity modulator; PC: polarization controller; PS: polarization scrambler; FBG: fiber Bragg grating; PD: photo detector.

and 8.2 kHz repetition rate is generated with extinction ratio about 35dB. The average pump signal power is ~0dBm. Besides, a replica of the same electrical pulse is used to trigger the real-time oscilloscope in order to facilitate data acquisition and signal averaging. The pump pulse is sent to EDFA for amplification before launched into FUT. A polarization scrambler is placed in front of the optical circulator to alleviate polarization dependent fluctuations for Brillouin effect between the pump and probe signals.

At the receiver, after Brillouin scattering frequency selective amplification, the probe signal from the FUT is first filtered by a narrow band fiber Bragg grating to block

DOFC at the lower sideband before entering the photo detector with 12GHz bandwidth, as shown in inset (d) of Fig. 5.4. A ~11GHz electrical signal is obtained by beating between optical carrier and DOFC signal at upper sideband and collected by a real-time oscilloscope working with 50 GHz sample rate. The collected DEFC signal is transferred to polarization controller (PC) for digital frequency down-conversion and further digital signal processing to locate the information of BFS.

Experimental Results

After processing using the method described in previous section, the amplification characteristics in the center of the BGS is shown in Fig. 5.5. For clarity, only the Brillouin gain around BFS is illustrated. The blue curve indicates the original measured BGS which is obtained directly by the intensity gain of measured frequency comb. Fluctuations can be easily observed due to the limited SNR. Then, received DEFC frames are first averaged 100 times to improve the measurement accuracy as well as to obtain the desirable SNR. The BGS after Lorentz fitting is shown as a red curve in Fig. 5.5, with the estimated full width at half maximum (FWHM) to be ~30MHz. In this way, the BGS distribution is

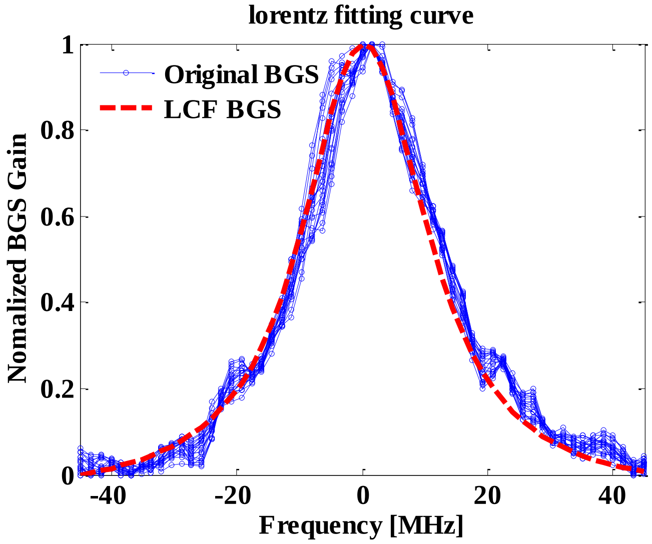

Fig. 5.5: Original measured BGS and Lorentz fitting curve.

successfully characterized without any frequency scanning. The measurement speed for BOTDA is improved by at least 2 orders with frequency step is 1.95MHz and coverage range is 2GHz. Through, it is unfair to compare the figure of measurement time directly with the conventional frequency-scanning based implementation method as the required frequency sweeping range for common sensing purpose is about several hundred MHz.

- **Temperature measurement result of DOFC based scanning-free BOTDA system**

The performance of proposed scanning-free BOTDA system is evaluated with temperature and stain measurement. In the temperature measurement configuration, the first 51m fiber of 10km fiber is heated using a thermal chamber. Temperature setup is adjusted from the 30°C to 60°C with 5°C steps. The linear fitting result of measured BFS changes with the temperature variation is depicted in Fig. 5.6. Temperature coefficient for this fiber is calculated to be 0.79°C/MHz, which is similar to the result of conventional BOTDA. Maximum temperature measurement deviation is about 0.5°C.

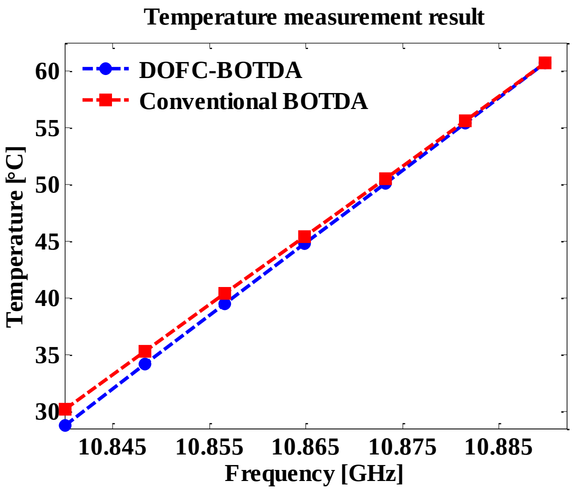

Fig. 5.6: Linear fitting of temperature measurement results using conventional BOTDA and DOFC-BOTDA.

In order to evaluate the proposed method on distributed sensing, measurements at three different positions along the 10km fiber are carried out: they are the first 51m fiber, middle 51m fiber and the last 51m fiber along the 10km fiber under test. The same temperature of 60°C is applied on aforementioned fiber section at different locations along the fiber. Fig. 5.7 shows the obtained BFS as a function of position after averaging 100 times. The inset pictures in Fig. 5.7 provide the zoomed view of the measured temperature changes after fitting the measured spectrum with Lorentz curve.

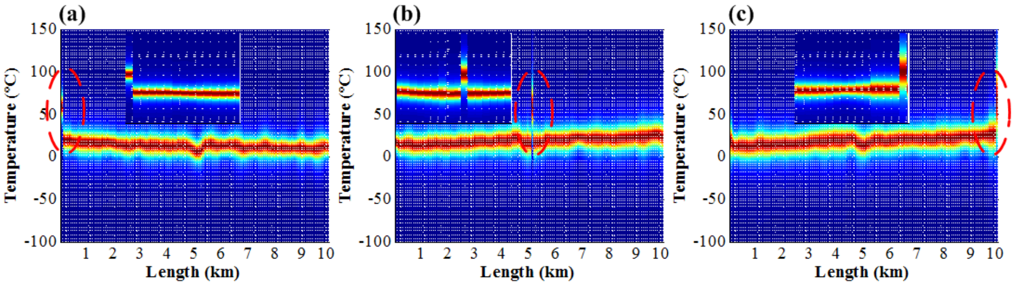

Fig. 5.7: Temperature measurement at different position: (a) first 51m fiber, (b) middle51m fiber (c) last 51m fiber of 10km fiber under test.

- **Stain measurement result of DOFC based scanning-free BOTDA system**

A strain measurement is also carried out based on almost the same experimental setup. One end of 51m fiber is first wound and fixed on a base plate of the optical experiment bench, while the other end of this 51m fiber is stretched by displacement platform to gradually increase the strain applied on fiber under test. The strain is adjusted from 0με to 900με changing with a step of about 110με corresponding to frequency shift step of 5MHz. Fig. 5.8 shows the liner fitting result of BFS as a function of strain at the first 51m fiber. Good linear relationship is achieved within the strain measurement range. The measurement deviation is less than 19με, and BFS coefficient is about 22.5με/MHz.

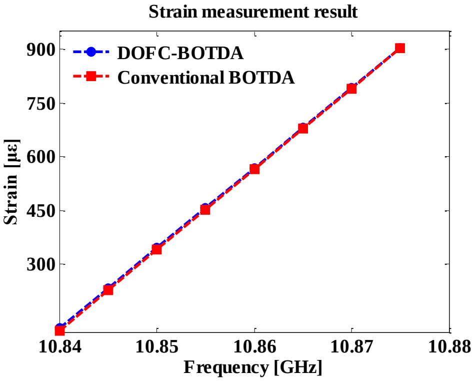

Fig. 5.8: Linear fitting of strain measurement results using conventional BOTDA and DOFC-BOTDA.

In the setup, the time needed for each acquisition is about 100 μs, and 100 acquisitions are needed in a single measurement to improve the obtained SNR, resulting a total measurement time of approximately 10ms. The obtained SNR at the end of FUT degrades slightly (~0.6dB) compared with conventional BOTDA due to the multiple power transfer occurred in the SBS process between single pump and DOFC. BOTDA sensors, however, typically operates in a small gain regime (i.e. the relative power transfer is actually very below). This degradation is estimated to be minor compared with the Brillouin gain. As reported above, conventional BOTDA and DOFC-BOTDA are performed for comparison. In the conventional BOTDA, the obtained SNR at the far end of fiber is 8.76dB. While in DOFC-BOTDA, this figure degraded slightly to 8.1dB.

5.3.1 Conclusions

In summary, a scanning-free BOTDA is presented and demonstrated experimentally. Based on DOFC, the BGS can be reconstructed without frequency-sweep thus greatly improves the measurement speed. Distributed temperature and strain measurements over 10km fiber range are conducted and compared with the conventional BOTDA. Favorable results are obtained and show a good agreement with conventional BOTDA.

6 Single-measurement digital optical frequency comb-based phase-detection Brillouin optical time domain analyzer

In this chapter, a single-measurement sweep-free distributed BOTDA sensor based on phase detection is proposed and experimentally demonstrated employing DOFC probe signal. BPS of DOFC probe induced by Brillouin interaction is measured using coherent detection in a single acquisition, without any frequency scanning and data averaging. Single-measurement BOTDA sensor based on BPS in 10km long fiber is demonstrated with a response time of 100 μs, which is limited only by the fiber length. The spatial resolution is 51.2m, determined by the duration of DOFC. The BFS uncertainty is estimated to be~1.5 MHz at the end of FUT. Benefiting from the fast response time, dynamic measurement up to 1 kHz vibration frequency has been demonstrated.

6.1 Single-measurement BOTDA system

In this chapter, the limitation factors for BOTDA system is further investigated. As reviewed, two major factors limiting the speed of a BOTDA[83]-[87]. One is the scanning of probe or pump frequency and the other is large amount of averaging times due to poor SNR. The first issue means that it is necessary to scan the whole BGS to identify the BFS. Typically, in conventional BOTDA, the probe or pump signal need to be swept in frequency domain more than 100 times around the BFS to interrogate Brillouin amplification characteristics at different positions along the fiber [88]-[90], which severely limits the demodulation speed of the BFS distribution along the optical fiber. As discussed in previous chapters, a DOFC based scanning-free BOTDA system has been proposed and experimentally demonstrated to facilitate the flexible reconstruction process of BGS without any frequency scanning [82].

However, the proposed schemes are based on direct detection of the probe signal intensity. Due to the poor SNR, over hundreds of averaging times is inevitable to enhance the measurement precision. While, phase detection has been considered as a promising candidate since Brillouin phase shift spectrum in the vicinity of BFS has been proved to be quasi-linear, which is far more sensitive than the intensity variation near the Brillouin gain peak. Several techniques have been proposed to characterize the BPS [91]-[93], and the benefits of BPS when used to determine BFS has been demonstrated in [94]-[95]. The high sensitivity of BPS has been applied in dynamic strain measurement with the advantage of large tolerance to variations in fiber attenuation or changes in pump pulse power [96].

In this chapter, the proposed direct detection DOFC based BOTDA system has been modified and a single-measurement BOTDA based on coherent detection of the phase of DOFC probe signal is reported without any averaging and frequency scanning process. The phase shift of each frequency component of DOFC probe, after transmitting through the FUT is directly mapped by coherent demodulation in a single data acquisition without any averaging, leading to a sensing speed only limited by the sensing range. Compared with the previous technique in[82], the measurement time is further reduced by eliminating the need for averaging. BPS detection instead of BGS has been performed for better accuracy. The performance of the proposed scheme is analyzed through simulation and experiment. Distributed temperature sensing over 10km FUT has been demonstrated by using the proposed single-measurement BOTDA with a BFS uncertainty of 1.5 MHz and spatial resolution of 51.2 m. With the advantage of high speed, dynamic measurement up to 1 kHz vibration frequency has been demonstrated.

6.2 Sensing principle, generation and demodulation of digital electrical frequency comb

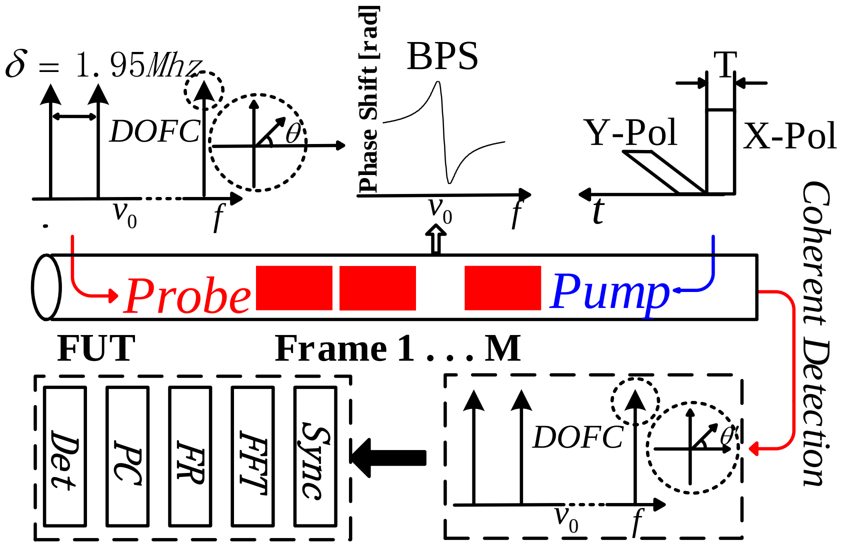

Fig. 6.1: Proposed BPS based BOTDA sensor scheme. DOFC: digital optical frequency comb; BPS: Brillouin phase spectrum; FUT: fiber under test; Sync: synchronization; FFT: Fast Fourier Transform; FR: frequency offset recovery; PC: phase noise compensation; Det: detection; θ: pre-defined phase vector of the DOFC; θ^': detected phase vector after Brillouin interaction in the FUT.

Fig. 6.1 presents the principle of the proposed scheme. In the proposed scheme, the generation process of DOFC is quite similar to the one elaborated in [82], except that the pulse train of data used to generate DEFC is replaced by a complex signal with predefined random phase offset vector θ. The optical frequency comb is generated using Electro-Optic Modulator (EOM) driven by DEFC. In this way, the same initial phase offset vector θ as defined in DEFC of each DOFC frame is guaranteed. Note that tradeoff exists between spatial resolution and frequency spacing of DOFC. Higher spatial resolution results in worse frequency resolution and vice versa. The optical field for the transmitted DOFC probe signal could be expressed as:

$$E_s(t) = \sum_{-N/_2+1}^{N/_2} e^{j(2\pi\nu_k t+\theta_k)} \quad \nu_k = k\delta \tag{5.2}$$

Where N is the number of frequency tones and δ is the frequency spacing between each tone. N frequency tones distributed symmetrically around the probe wave are transmitted simultaneously with a spacing of δ, resulting in a sensing coverage range of $N\delta$. Orthogonally polarized pump pulses are utilized to excite Brillouin effect in the FUT, which can significantly eliminate the detrimental effects from polarization noise [97]-[100].

After Brillouin interaction with pump signal in FUT, the optical field of DOFC probe (normalized fields are assumed for simplicity) detected at coherent receiver is given by the following expression:

$$E_s(t) = \sum_{-N/_2+1}^{N/_2} e^{j(2\pi\nu_k t+\theta_k)} H_{SBS}(\nu_k) \tag{5.3}$$

$H_{SBS}(\nu)$ is the complex Brillouin response spectrum for different frequency offset, which has the following form:

$$H_{SBS}(\nu) = (1 + g_\nu)e^{j\phi_\nu} \tag{5.4}$$

where g_ν and ϕ_ν are the Brillouin gain and phase spectrum, respectively. Then the phase shift φ recorded on each frequency component is retrieved by offline digital signal processing (DSP).

The post-processing algorithm has been elaborated in chapter 4. As the transmitted DOFC signal is known, the processing algorithm is simplified considerably, and it is modified to best suit the sensing purpose. The proposed demodulation algorithm includes five parts, i.e. synchronization, FFT, probe and LO frequency offset recovery, phase noise compensation and detection. In the synchronization, the temporal relationship of each detected DOFC frame is located by calculating the correlation between the received frames and the transmitted ones. In this way, the correlation peak and hence the temporal duration for each DOFC frame are readily determined. FFT is used subsequently to get the complex signal of each frequency tone and the angle of the complex signal is then calculated. By comparing the angle of the received complex signal with that of the transmitted one, the phase shift spectrum is easily obtained. As the phase shift is affected by the frequency offset and phase fluctuation between the probe and LO exist during coherent detection, frequency offset recovery and phase noise compensation is required to minimize the phase noise. Beating frequency between the probe and LO will inevitably lead to a continuous phase change of probe signal. Therefore, frequency offset is treated as the constant relative phase rotation between each DOFC frame and extra phase drift of adjacent frame due to frequency offset is calculated sequentially using the frequency offset recovery algorithm. To compensate the extra phase shift due to phase noise between LO and probe, here one of frequency tones (usually the first tone is used for convenience) is selected to serve as an accurate reference of phase fluctuation distribution and used for further compensation of the residual phase noise for the remaining frequency components. After the extra phase shift due to frequency offset and phase noise is compensated, the frequency-dependent Brillouin phase shift is simply obtained, and BPS can be reconstructed accordingly. The BFS distribution as well as the temperature or strain along the fiber are obtained based on the measured BPS.

The determination of spatial resolution and location is the same as that in [82]. Unlike conventional BOTDA, the spatial resolution in the proposed scheme is determined by the duration of DOFC frame. Probe signal is continuous but composed of M consecutive DOFC frames (indicated as frame 1 to M) with minor time spacing between each other. In addition, M consecutive DOFC frames serve as probe to interact with pump in sequence through SBS in the fiber. In this way, FUT can be divided as M independent sections. The amplification and phase shift spectrum of individual interaction section is recorded by each DOFC frame. Hence, the minimum detectable length of fiber, namely the spatial resolution, is limited by the duration of DOFC frame (512 ns), resulting in a spatial resolution of 51.2 m in our case.

It should be noted that, recovered phase shift spectrum still suffers from the random intensity noise which is demonstrated in the following. The variance of the Gaussian noise affecting BGS and BPS is the same when using the interference method described in [94][95], as the intensity variation is directly translated to the phase fluctuation. In the proposed method, the BPS is fully retrieved by coherent detection, and hence it results in an improved performance of phase noise variance. As described in the Appendix, the variance of phase noise can be expressed as follows:

$$D(\phi_k) = \frac{\sigma^2/_2}{1+g^2} \tag{5.5}$$

Where σ is the stand deviation of measurement noise in Brillouin gain spectrum and g is the Brillouin gain coefficient. Note that the variance of phase noise in Eq. (6.4) is half of the intensity noise. It implies that with the same obtained SNR, the averaging time can be reduced by two times. Simulations have been conducted to validate these expressions. Perfect BGS and BPS profile is assumed in the simulation. As in conventional BOTDA, SNR is defined as the inverse of maximum gain of time trace, which in this case equals to $\frac{g}{v}$. In the simulation, 60 frequency tones with 2 MHz frequency spacing are utilized as DOFC probe signal. It should be noted that the intensity of complex optical field for each frequency tone is normalized. Fig. 6.2 (a) shows the variance of phase noise and intensity noise as a function of SNR. It shows that the variance of phase noise is only half

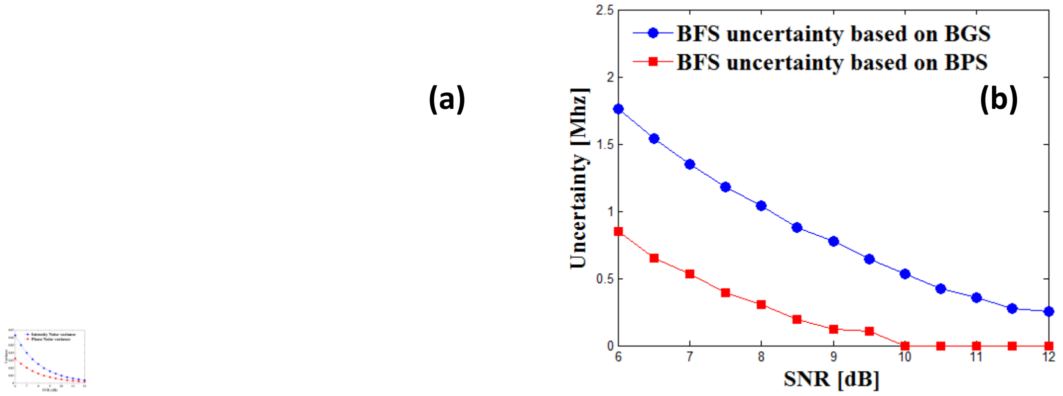

Fig. 6.2: (a) intensity noise variance and phase noise variance as a function of SNR. (b) BFS uncertainty based on BGS and BPS as a function of SNR.

of the variance of intensity noise under the same SNR. Furthermore, the BFS error based on BGS and BPS are calculated and illustrated in Fig. 6.2(b). 100 measurements are simulated to calculate the uncertainty of BFS. Lorentzian curve fitting (LCF) method is used for the determination of BFS based on BGS while linear fitting method is used for the case of BPS. Though both uncertainties using BGS and BPS deteriorate with the degradation of signal quality, the normalized uncertainty based on BPS still shows clear improvement under the worst situation where SNR is merely 6dB.

6.3 Experimental setup

The experimental setup illustrated in Fig. 6.3 is used to achieve the proposed single-measurement BOTDA. A tunable laser operating at 1550 nm with 100 kHz linewidth is split into two parts by 3dB coupler to serve as pump and probe signal respectively.

Unlike the conventional implementation for frequency-sweep BOTDA, optical pump frequency is up-converted by modulation. A PC is inserted between coupler and MZM to maintain high modulation efficiency. MZM biased at null point is driven by a synthesizer running at the frequency around the BFS to create the required sidebands. The maximum achieved extinction ratio of carrier suppression exceeds 30 dB. Then the higher frequency sideband is selected by a narrow bandwidth Fiber Bragg grating (FBG) filter before chopped by another IM. Optical pulse series is generated through the IM driven by pulse generator which provides 100 ns long pulses with 8.3 kHz repetition rate. The IM allows shaping high extinction ratio optical pulses (~40 dB). The generated optical pulse series is then split by polarizing beam splitter (PBS) to two identical portions with orthogonal polarization state. A PC is inserted in front of PBS to adjust the state of polarization (SOP) of input pump signal and guarantee identical power in two polarization

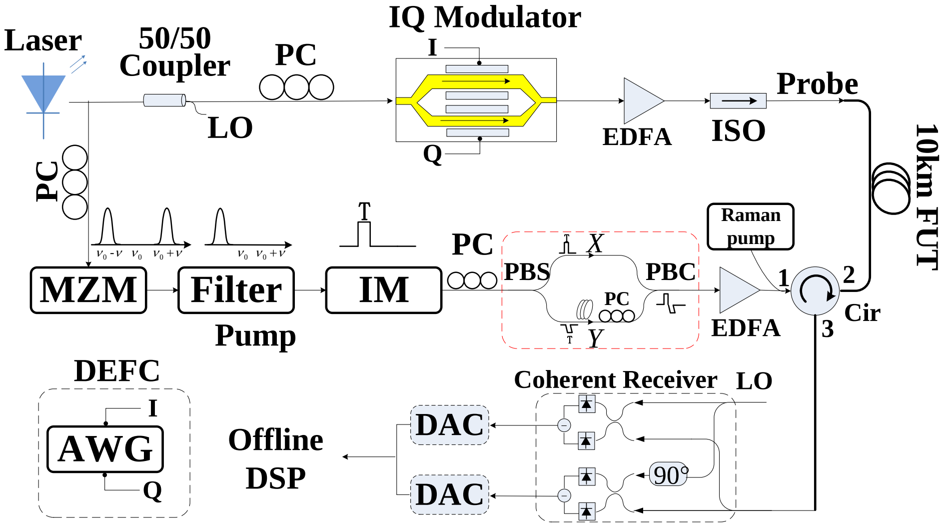

Fig. 6.3: Experiment setup of scanning-free BOTDA based on polarization-diversity pump. PC: polarization controller; EDFA: erbium-doped fiber amplifier; ISO: isolator; MZM: Mach-Zehnder modulator; IM: intensity modulator; PBS: polarizing beam splitter; PBC: polarizing beam combiner; Cir: circulator; LO: local oscillator; DAQ: data acquisition card; OSC: oscilloscope.

state. Another PC has been used in one of the branches in PBS/PBC structure in order to control SOP of the branch for polarization multiplexing. Before recombined in the subsequent polarizing beam combiner (PBC), one channel is delayed by a 20m single mode fiber (SMF) corresponding to the pulse width of 100 ns. The polarization multiplexed pump pair is directed into the FUT via a circulator after amplified by an EDFA. The average power of pump is set at 0 dBm. A Raman pump with a total power of ~200mW is co-propagating with Brillouin pump signal to compensate energy loss during transmission.

In the opposite direction, another 3dB coupler is used to divide the optical wave into two branches for probe optical signal and LO, respectively. It should be noted that the LO and probe signal are derived from the same laser source, which avoids significant laser frequency drift. More complicated frequency offset estimation and phase noise compensation algorithm are necessary if independent probe and LO laser is used. Probe signal is modulated by an IQ modulator with in phase and quadrature port driven by two independent channels of AWG. The modulator output comprises a baseband optical frequency comb with a frequency range of 1 GHz and 1.95 MHz spacing. The optical power of the probe is set at 3dBm by EDFA before delivering it into the FUT where it counter-propagates with the pump signal to characterize the phase spectrum profile.

Integrated digital coherent receiver (ICR, Fujitsu FIM24704) is used at the receiver side to obtain the phase shift directly. After Brillouin frequency selective amplification, the probe signal from the FUT is delivered to the optical coherent receiver. Note that no extra EDFA is needed to compensate the energy loss of probe signal and satisfy the threshold of direct detection, which helps to eliminate the broadband noise induced by amplification. Probe signal is beating with LO and detected by balanced detector. The resultant electrical signals are collected by data acquisition card (DAQ) with 2 GHz sampling rate and further processed to obtain the distribution of BFS along the fiber.

6.4 Experimental results

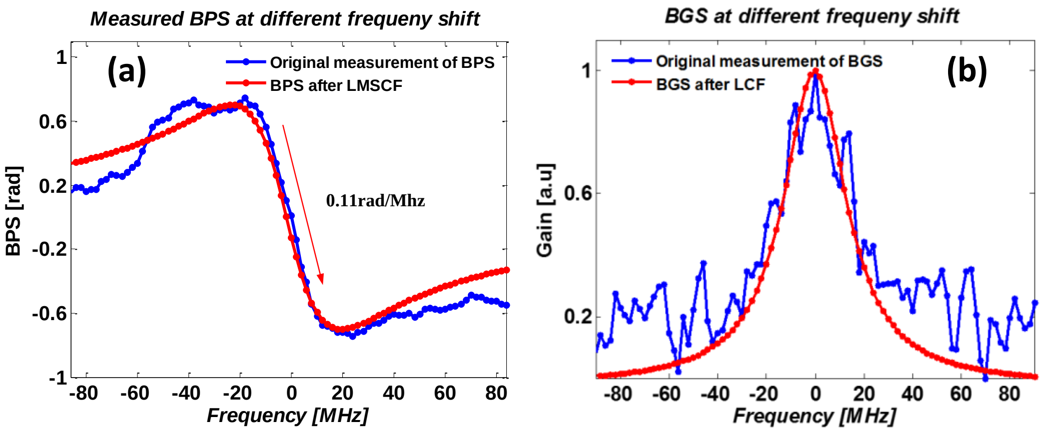

Fig. 6.4: Brillouin phase spectrum and Brillouin gain spectrum measured by the multi-tone probe signals at the beginning of FUT.

The sensing performance of the proposed single-measurement BOTDA system is evaluated using 10km SMF (composed of two 5km fiber reels) with uniform BFS distribution of 10.83GHz at room temperature (@1550nm). It should be noted that the calibration process is necessary to eliminate the distortions from electronic amplifier, photo-detector and environment variations. This can be done by recording the frequency response (including gain and phase characterization) of the multi-tone probe signals with a frequency granularity of 1.95MHz. Both gain and phase shift profiles are recovered in the measurement. Measured BPS without any applied environmental variance is shown in Fig. 6.4(a). The linear part of the BPS is about 40 MHz, equal to the linewidth of BGS. The slope for the linear part is estimated to be 0.11 rad/MHz using least mean square curving fitting (LMSCF). The BFS is readily extracted by locating the linear center of BPS fitting process, which locates the characteristics of linear drop in the curve. Since BGS is simultaneously obtained in the configuration, the results for BGS measurement are also shown. Original BGS is illustrated as the blue curve in Fig. 6.4(b), while the BGS after

LCF is shown as a red curve, with the estimated FWHM of ~40MHz.

Then the BPS distribution along the FUT is analyzed and depicted in Fig. 6.5. As the Brillouin phase profile can be reconstructed without frequency scanning process and averaging, the resultant response speed of the proposed sensor is solely limited by the FUT length which is 10km in the experiment, corresponding to 100 μs. The inset illustrates the corresponding BFS distribution extracted from the BPS. Assisted by the Raman

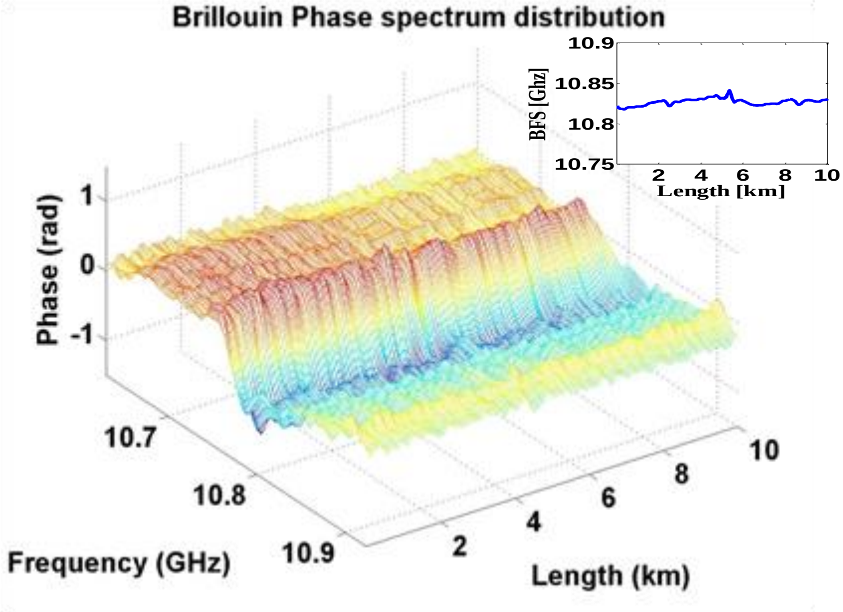

Fig. 6.5: Brillouin phase spectrum and the measured BFS distribution (inset) along the FUT.

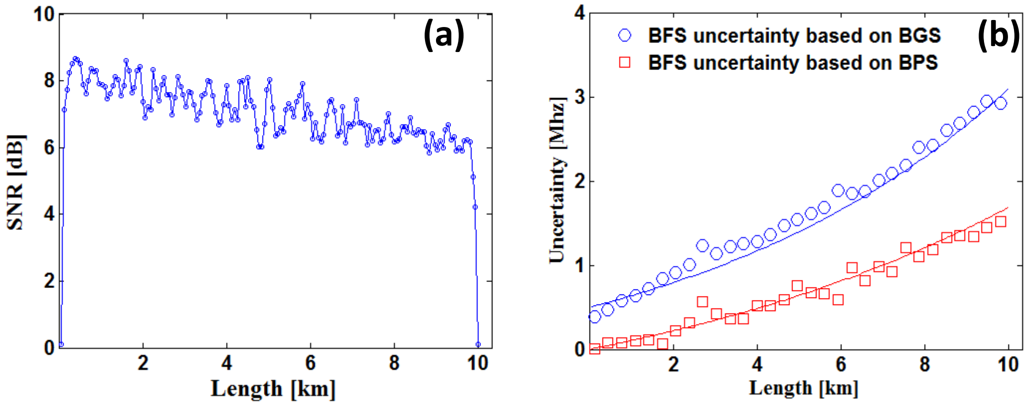

Fig. 6.6: (a) The SNR along FUT, defined by the maximum gain in the central of BGS normalized against noise deviation. No averaging is used in the measurement of SNR. (b) BFS uncertainty against distance calculated using BGS and BPS, respectively.

amplification, the pump power depletion can be largely compensated and hence it maintains a power level to secure sufficient gain for the proposed scheme.

The SNR and BFS uncertainty along FUT using are given in Fig. 6.6. Relatively poor SNR is observed due to the fact that no averaging is used in the experiment. Linear fitting method is used for the determination of BFS from BPS, while as a comparison LCF method is used to obtain BFS from BGS. BFS uncertainty is calculated by taking the standard deviation of 100 experimental measurement results. Though both uncertainties based on BPS and BGS deteriorate with the degradation of signal quality, the one using BPS is estimated to be ~1.5MHz at the end of FUT which is less than half of that for BGS. The mismatch of the absolute uncertainty value between Fig. 6.6 (b) and Fig. 6.2 (b) simulation result could be attributed to the polarization misalignment during the splitting and recombination of pump pulses and the imperfect orthogonality of pump pairs during

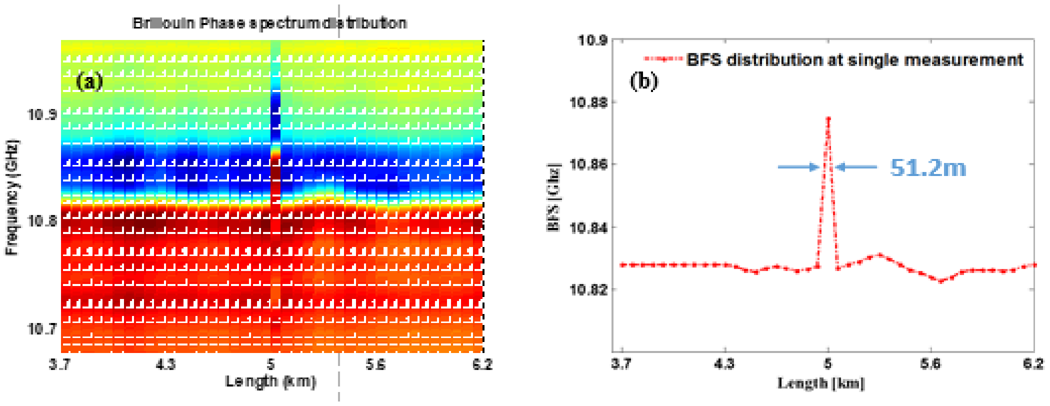

Fig. 6.7: Evaluation of spatial resolution with ~51m fiber section at the middle heated to 60 ℃ (equivalent to 50MHz). (a) BPS distribution (b) BFS distribution.

propagation inside fiber.

In order to experimentally evaluate the spatial resolution of the proposed scheme, 51-meter fiber section at the middle of FUT is heated by a thermal chamber. Spatial resolution is determined through the measured BFS transition between the heated and unheated fiber sections. As shown in Fig. 6.7, the BPS and resultant BFS at the hot-spot section with a temperature of 60°C is different from those of section at room temperature, and the spatial resolution is found to be 51.2 m at the temperature transition section, which matches well with the 512-ns duration of the DOFC.

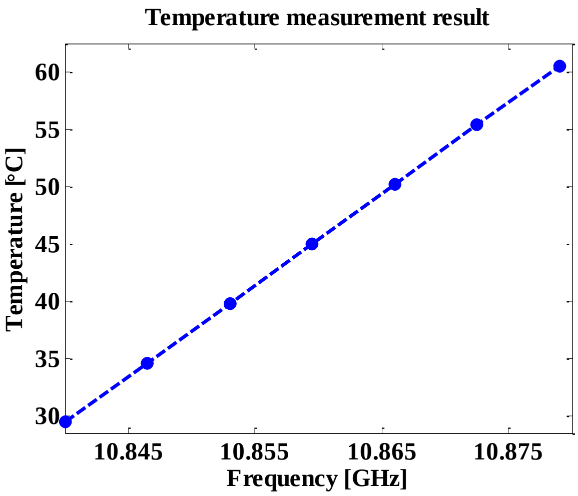

Fig. 6.8: Linear fitting results of temperature measurement.

To evaluate the temperature accuracy based on the proposed scheme for BPS measurement, the last 51m fiber of FUT is heated from 30°C to 60°C with 5°C step. The measured BFS change with the temperature variation is depicted in Fig. 6.8. Maximum temperature measurement deviation from the linear fitting is about 0.5°C and temperature

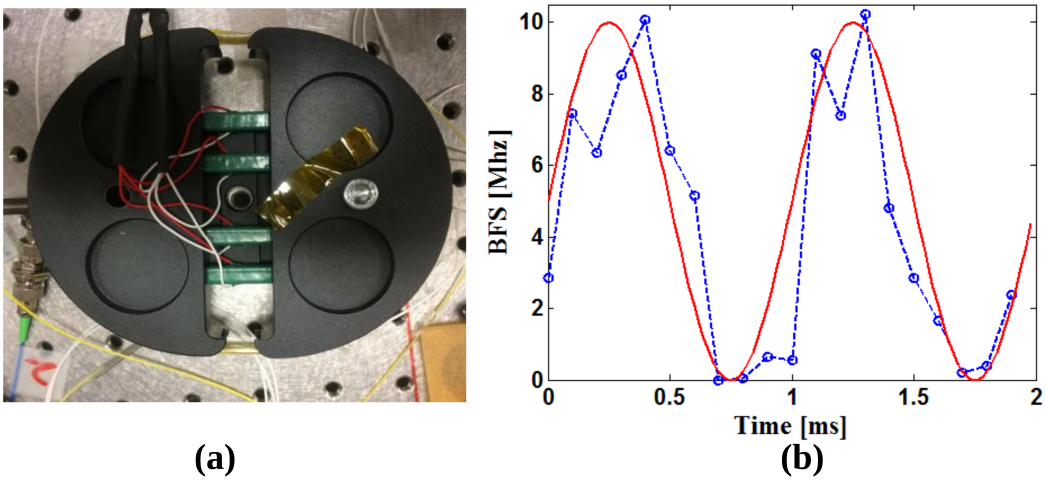

Fig. 6.9: Vibration measurement result. (a): Piezo-ceramic Transducers (PZT) fiber stretcher. (b): measured BFS variation as a function of time. Dynamic strain is applied by Piezo-ceramic Transducers (PZT) fiber stretcher with 51meter fiber wound on the PZT disk. The stretcher is driven by 1 kHz sinusoidal signal.

coefficient for this fiber is calculated to be 1.25 MHz/℃.

Moreover, vibration measurement using DOFC based phase-detection BOTDA has also been demonstrated using PZT driven by 1 kHz sinusoidal signal. The strain coefficient of the fiber measured in the experiment is about 0.045 MHz /με **错误!未找到引用源。**. Thus, the theoretical dynamic range of strain is about 22500με. Since the spatial resolution is 51.2m, 51m fiber is wound on the PZT for the demonstration of dynamic measurement. The results are given in Fig. 6.9. The time interval between each data point in Fig. 6.9 (b) is 0.1ms corresponding to a sampling rate of 10 kHz which is limited only by the fiber length (10km in our case). As shown in Fig. 6.9 (b) the BFS is measured to have a variation rate of 1 kHz, which confirms with the vibration frequency applied on the 51m fiber. This indicates the successful measurement of dynamic strain using the proposed scheme. Note that due to the limited elongation length of the PZT, the maximum BFS change is only 10MHz. Furthermore, non-uniform strain distribution on the 51m fiber induced by the imperfect winding process on the PZT distorts the BFS waveform from an ideal sinusoidal signal. All of these results in the discrepancy between the measurement result waveform and the applied vibration signal.

6.5 Conclusions

In summary, a single-measurement BOTDA sensor is proposed and experimentally demonstrated with 51 m spatial resolution over 10km fiber by employing coherent detection of BPS without any frequency scanning and averaging processes. The phase shift for all the frequency tones induced by Brillouin interaction are obtained in a single data acquisition. The response time of 100 μs is limited only by the fiber length in our single-measurement BOTDA. Temperature measurement of 51m heated fiber over 10km FUT indicates a BFS uncertainty of 1.5 MHz and maximum temperature measurement deviation of 0.5°C. Dynamic measurement up to 1 kHz vibration frequency is successfully demonstrated to verify the dynamic characteristic of proposed technique. The high measurement speed and phase detection make the single-measurement BOTDA promising candidate for wide range of fast sensing scenarios with acceptable accuracy.

7 Summaries and Future works

In this Chapter, summaries of the thesis are given and possible future works for optical scattering based DOFS are discussed.

7.1 Summaries

DOFS systems have developed rapidly and have been applied in various application scenarios for their unique advantages comparing with other alternative sensing techniques. Though concentrated mainly on the measurement of quasi-static process like temperature variation or applied strain at the beginning period, the dynamic properties of optical sensing techniques are increasingly valued recently. Motivated by demands for lower respond time applications, dynamic DOFS system has developed rapidly for the purpose of providing dynamic information of non-static scenarios involving pipeline security monitoring, infrastructure health monitoring, etc. Several novel distributed fiber-optic sensing schemes for such dynamic measurements have been proposed and investigated in depth. In this thesis, dynamic DOFS systems based optical scatterings has been investigated.

Chapter 1 presents the backgrounds and development of dynamic DOFS techniques in general.

In chapter 2, the origin of optical scattering in fiber is discussed including the elastic scattering and inelastic scattering. The frequency spectrum as well as the scattering characteristic are presented. The transmission characteristics of the phenomenon is described in mathematical equations derived from Maxwell's equation. Then, basic principle of optical sensor system based on Rayleigh scattering phenomenon is discussed in depth. Together with the performance in terms of the SNR, measurement accuracy and spatial resolution. After that, the operating principle the optical fiber scattering of Brillouin based scattering is also presented. Optical sensor systems based on each Brillouin scattering phenomenon including BOTDR and BOTDA are discussed independently. Especially, the operation principle of BOTDA is explained in detail with its dynamic sensing performance, obtained SNR and processing method.

In chapter 3, an integrated telecommunication system and phase-OTDR sensing system with shared optical bandwidth is described. OFDM modulation technique is selected and applied in the communication system as it is widely recognized as one of the major transmission techniques used in modern optical communication systems for its numerous advantages. In the proposed system, 16QAM-OFDM signal at 112 Gb/s is transmitted over 20km SSMF. Meanwhile distributed phase sensitive-OTDR system is deployed to monitor the environmental variation along the fiber. it should be noted that these two systems share the same optical source before being modulated and launched into the FUT. Hence, the mutual influence is inevitable. Experimental results for the communication system show that compared with unaffected OFDM frames, about 1 dB OSNR penalty to BER performance is observed in the affected frames by the high-power optical pulse used in sensing configuration. On the other hand, the influence of communication signal on the sensing system is almost negligible as the reflected OFDM signal power is extremely weak (more than 30 dB lower than reflected phase-OTDR signal). 20 m spatial resolution and SNR of location information as high as 8.4 dB is obtained with 20 km fiber length. Detection of 1khz vibration applied by PZT is also successfully demonstrated.

In chapter 4, the principle of scanning-free BOTDA sensor is elaborated in detail. The progress of dynamic BOTDA system is reviewed first. Then the operation principle of proposed scanning-free BOTDA based on DOFS is discussed with the modulation and demodulation method. Characterization of the SBS induced gain and phase shift profile based on the DOFC probe signal is presented along with the detection and DSP procedures of DOFC signal. Sensing performance of the proposed system is analyzed in the last part.

In chapter 5, ultra-fast BOTDA system based on direct detection of DOFC is proposed and demonstrated experimentally. The frequency spacing and coverage bandwidth for used DOFC is 1.95-MHz and 2-GHz, respectively. The DOFC can be used to reconstruct the Brillouin gain spectrum (BGS) and locate the Brillouin frequency shift (BFS) without frequency scanning and thus can improve the measurement speed about 100 times compared with the conventional BOTDA. This scanning-free BOTDA system has also been demonstrated experimentally with 51.2-m spatial resolution over 10-km standard single mode fiber (SSMF) and with resolution of 1.4°C for temperature and 43.3με

In chapter 6, a single-measurement BOTDA based on coherent detection of the phase of DOFC probe signal is reported without any averaging and frequency scanning process. The phase shift of each frequency component of DOFC probe, after transmitting through the FUT is directly mapped by coherent demodulation in a single data acquisition without any averaging, leading to a sensing speed only limited by the sensing range. Compared with the previous techniques, the measurement time is further reduced by eliminating the need for averaging. The dynamic property of the proposed system is demonstrated with a 1kHz vibration measurement.

7.2 Future works

A number of additional techniques can be further investigated in the future for the works presented in this thesis. In this section, possible extensions of the research work on distributed optical fiber sensing are illustrated.

7.2.1 Spatial resolution improvement of dynamic BOTDA sensing system

For future work, one major research area is to improve the spatial resolution of the proposed technique which is currently limited by the tradeoff between probe frame duration length and frequency resolution. Events with 51.2m spatial distribution can be successfully discerned with current configuration. While modern advanced applications require a better spatial resolution without compromising temperature/strain precision over a long range. For this purpose, further improvement of the spatial resolution performance can be achieved by either using a time-resolved plan of chirped pump signal or relaxing the frequency step requirements of DOFC while introducing a few frequency interleaving arrangements.

Spatial resolution improvement using sparse frequency comb signal

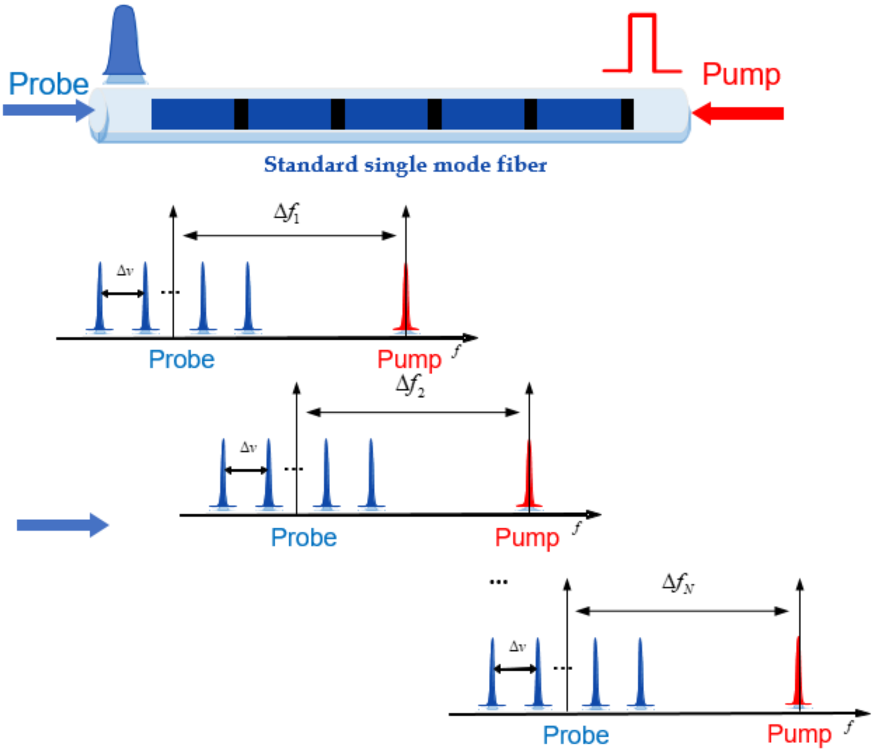

Fig. 7.1 Spatial resolution improvement using sparse frequency comb signal.

As discussed in previous sections, spatial resolution is limited by the frequency spacing between DOFC and pump signal. comprise in frequency resolution would, without a doubt, improve the spatial resolution. For example, using a sparse frequency comb with gap of 10MHz, the spatial resolution is improved to 10 meters. Then, we can use interleaving method to compensate the missing information with the blank area between each frequency

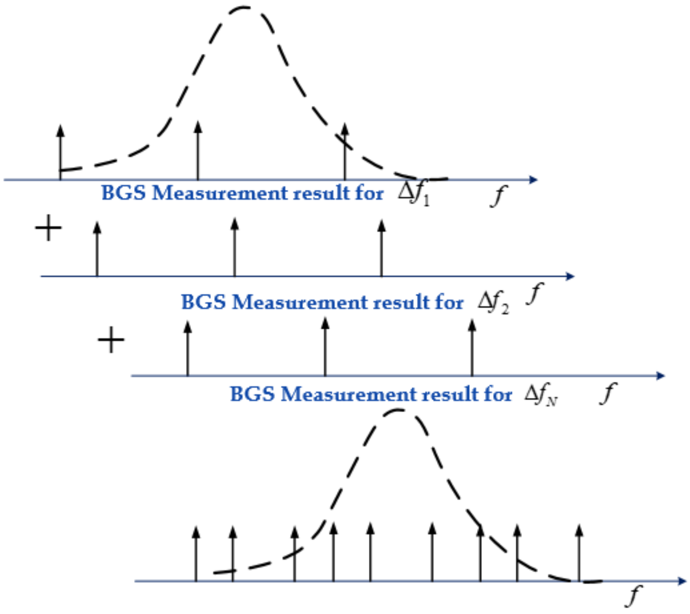

Fig. 7.2 N interpolation between M BGS measure results.

tone. As shown in Fig. 7.2, the frequency distance between probe is initially set at Δf_1, the corresponding measured BGS/BPS is at $\Delta f_1 + \Delta v(1{:}M)$. M is the number of frequency tones. Then, increase the frequency distance from Δf_1 to Δf_N. In this way, the N times measurement results construct the interpolation between M BGS measure results.

Spatial resolution improvement using frequency multiplex pump signal

Another method to improve the spatial resolution is using frequency multiplex pump signal. As shown in Fig. 7.3, instead of using the single tone pump, a frequency multiplex signal is utilized as pump signal to interact with the corresponding frequency span of DOFC probe

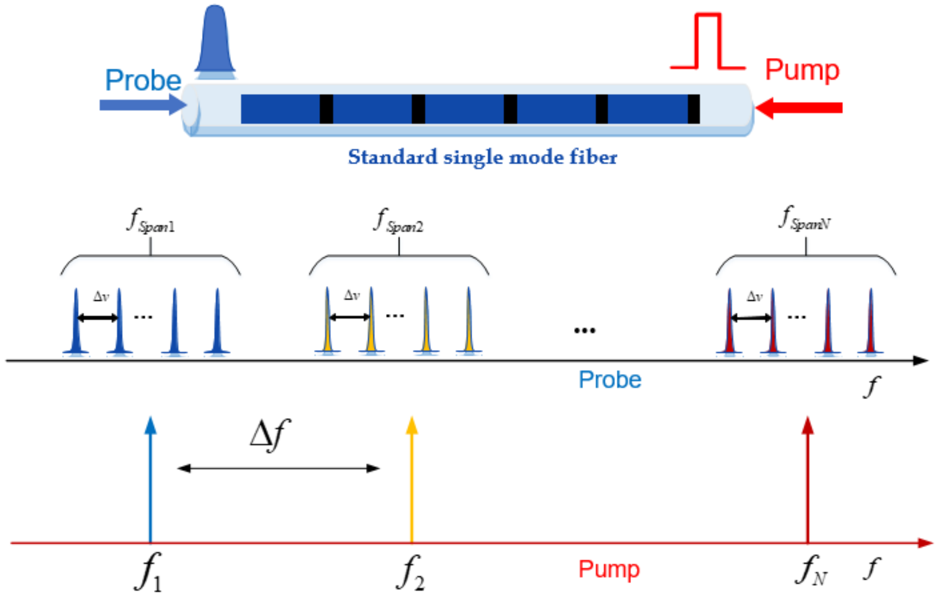

Fig. 7.3 Spatial resolution improvement using frequency multiplex pump signal.

signal. Therefore, the frequency resolution of probe signal is alleviated, and thus spatial resolution is improved. For example, if we use N pump signals, each with a spacing of Δf. In particular, $\Delta f = M \cdot \Delta v + \Delta f_s$. Then, the measured BGS/BPS for each measurement is shown in Fig. 7.4.

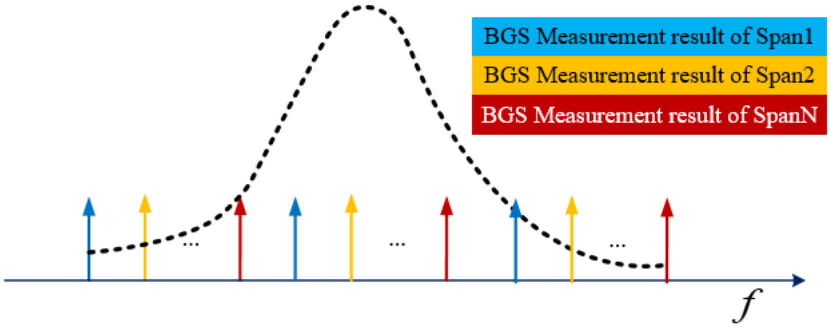

Fig. 7.4 Interpolation of BGS measurement results using frequency multiplex pump signal

7.2.2 Embedded dynamic optical sensing system for various kind of optical communication system

With the rapid development of optical communication technique driven by the bandwidth requirements, optical fiber network is deployed all around the world connecting cities, towns, highways and links countries. In 2018, the total deployed optical fiber cable exceeds 500 million kilometers in total. Up to now, the operation status of optical fibers in communication network is not sufficiently monitored. The current situation is that it is impossible to take precaution actions unless damage of optical fiber cable is caused. This means that the status of communication is binary: functional or damaged.

Among various solutions, we have demonstrated one possibility of using phase-sensitive OTDR sensing system for sensitive monitoring of optical OFDM communication system. Apart from enhancing the system performance of DOFS techniques based on Rayleigh scattering and Brillouin scattering, it is also possible to combine the system with other sensing schemes, such as intensity scattering, frequency, polarization and phase based sensing schemes, which can be employed to realize hybrid systems to provide more sensing information. For example, we may use the optical interferometer based on phase interference to provide more accurate measurement while using distributed sensing scheme

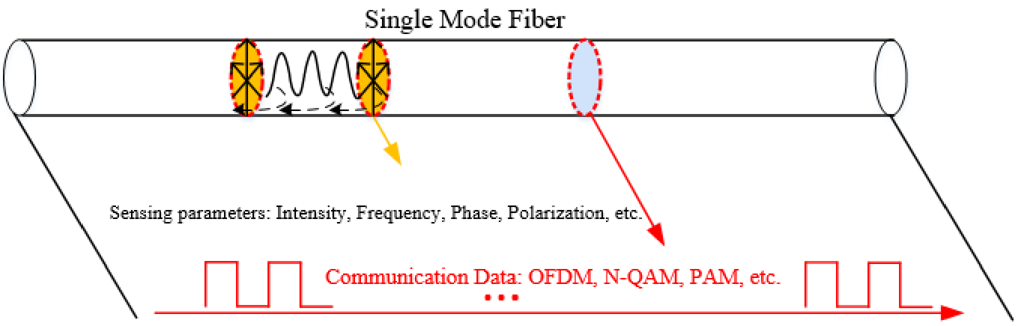

Fig. 7.5 Embedded dynamic optical sensing system for various kind of optical communication system.

for providing location information.

On the other hand, as shown in Fig. 7.5, various kinds of transmission technologies are used in different communication systems including advanced modulation formats, wavelength-, polarization- and space- division multiplexing techniques. Therefore, the sensing requirement is diverse. In the future, we will continue to investigate the application of distributed dynamic optical sensing system in optical network. Especially, the sensing performance in terms of measurement speed, accuracy, spatial resolution as well as sensing distance. Besides, the influence induced by various sensing schemes on the optical communication network will be emphasized.

7.2.3 Application of machine learning algorithms in dynamic sensing system

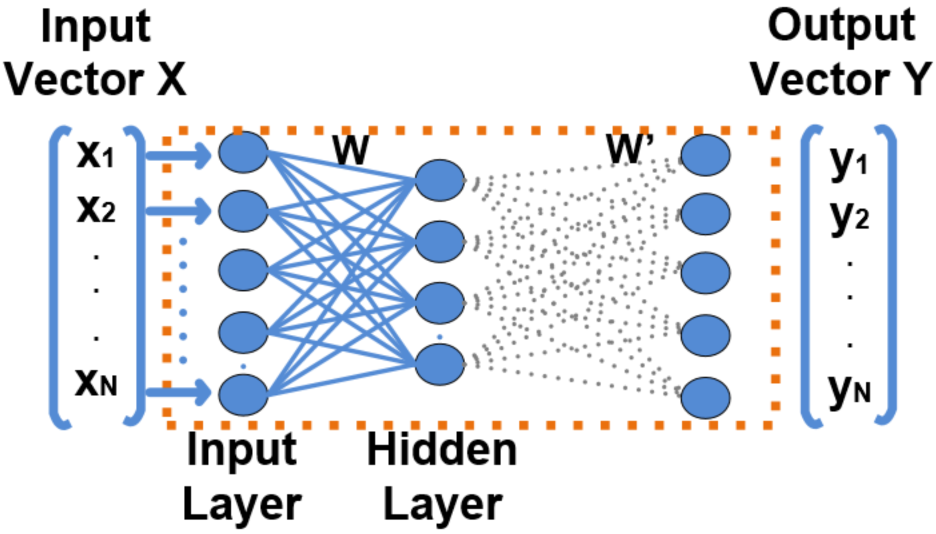

Fig. 7.6: Application of machine learning algorithms in processing dynamic sensing measurement results.

Another possible area of investigation is the use of advanced algorithms for sensing system performance enhance which may evolve to a system or a network providing massive amount of raw data in real-time manner, the advanced algorithms shall also help for extracting, analyzing, and archiving the sensing information. The algorithms include artificial neural network, deep learning algorithms, which are commonly used in computer science area, and they can be integrated into the sensing system for post-processing in order to enhance the system performance or extend new features.

7.2.4 Real-time realization and field test of dynamic sensing system

Up to now, most dynamic sensing techniques focus on the experimental demonstration of vibration detection performance using single tone signal generated using for example a PZT. However, the performance of the system in field-test with signal with complicated frequency components over a large dynamic range still need to be evaluated. In addition, analyzing the signal obtained using the DOFS systems to identify some special events shall enable it to be used in practical application systems. Real-time demonstration of proposed distribute dynamic sensing system is illustrated in Fig. 7.7 with Analog-to-

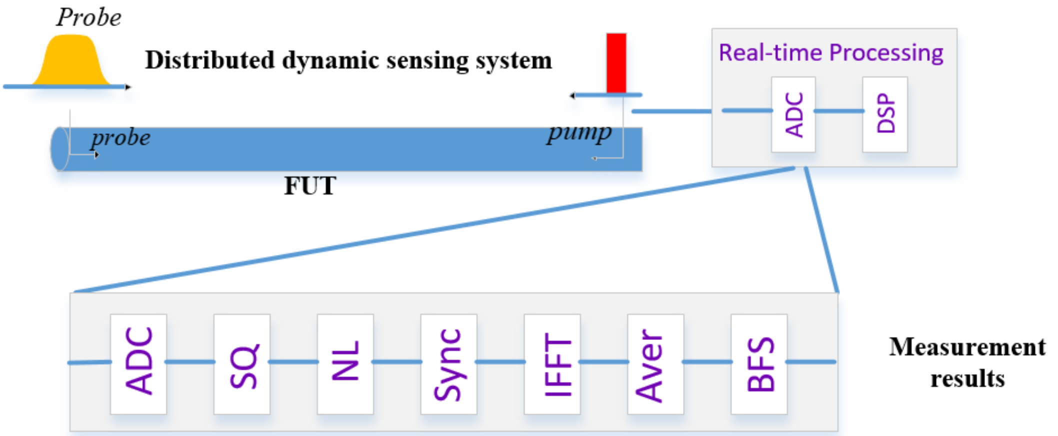

Fig. 7.7: Illustration of the real-time realization of proposed dynamic distributed optical sensing system.

Digital Converter (ADC) and digital signal processing (DSP) configuration. The detected signal is collected and digitalized by a high-speed ADC. Collected samples are processed in Field Programmable Gate Array (FPGA) with separate digital signal processing functional part. Measured trace is first quantified and normalized to allow for digital processing. Then synchronization is taken to subtract the consecutive probe frames. Through IFFT, the probe frames are transformed to the frequency domain to analyze the BFS distribution, by which the measurand is determined.

Appendix

Maxwell's Wave Equations

To better explain the propagation of optical signals inside optical fibers which is governed by Maxwell's equations, the propagation equation is derived in the following [101], [102]:

$$\nabla \times \boldsymbol{E} = -\frac{\partial \boldsymbol{B}}{\partial t} \tag{5.6}$$

$$\nabla \times \boldsymbol{H} = \frac{\partial \boldsymbol{D}}{\partial t} + \boldsymbol{J} \tag{5.7}$$

$$\nabla \cdot \boldsymbol{D} = \rho_f \tag{5.8}$$

$$\nabla \cdot \boldsymbol{B} = 0 \tag{5.9}$$

Where $\boldsymbol{E}$ and $\boldsymbol{H}$ are electric and magnetic field vectors. $\boldsymbol{D}$ and $\boldsymbol{B}$ are corresponding electric and magnetic flux densities. As optical fiber contains no free charges as well as electrical currents, so:

$$\boldsymbol{J} = 0 \tag{5.10}$$

$$\rho_f = 0 \tag{5.11}$$

While the densities $\boldsymbol{D}$ and $\boldsymbol{B}$ is expressed as:

$$\boldsymbol{D} = \varepsilon_0 \boldsymbol{E} + \boldsymbol{P} \tag{5.12}$$

$$\boldsymbol{B} = \mu_0 \boldsymbol{H} + \boldsymbol{M} \tag{5.13}$$

Where ε_0 is the permittivity in vacuum and μ_0 is the permeability in vacuum. $\boldsymbol{P}$ and $\boldsymbol{M}$ represent the electric and magnetic polarizations. Taking the curl in both side of Equation (2.1) and substituting the Equation (2.2), (2.5) and (2.6). The term $\boldsymbol{D}$ and $\boldsymbol{B}$ is eliminated in favor of $\boldsymbol{E}$ and $\boldsymbol{P}$:

$$\nabla \times \nabla \times \boldsymbol{E} = -\frac{1}{c^2}\frac{\partial^2 \boldsymbol{E}}{\partial t^2} - \mu_0 \frac{\partial^2 \boldsymbol{P}}{\partial t^2} \tag{5.14}$$

$$\frac{1}{c^2}\frac{\partial^2 \boldsymbol{E}}{\partial t^2} - \nabla^2 \boldsymbol{E} + \nabla(\nabla \cdot \boldsymbol{E}) + \mu_0 \frac{\partial^2 \boldsymbol{P}}{\partial t^2} = 0 \tag{5.15}$$

The relation $\mu_0\varepsilon_0 = {}^{1}\!/_{c^2}$ was used and the operator $\nabla^2 = \frac{\partial^2}{\partial x^2} + \frac{\partial^2}{\partial y^2} + \frac{\partial^2}{\partial z^2}$. It is easy to notice that total polarization $\boldsymbol{P}$ contribute to the nonlinear phenomena during the transmission in fiber. At the same time, polarization $\boldsymbol{P}$ originate from the electric dipoles which is nonlinear response of the applied electrical field $\boldsymbol{E}$. Generally, a more commonly used equation is used to describe the relation:

$$\boldsymbol{P} = \varepsilon_0(\chi^{(1)} \cdot \boldsymbol{E} + \chi^{(2)} \vdots \boldsymbol{EE} + \chi^{(3)} \vdots \boldsymbol{EEE} + \cdots) \tag{5.16}$$

where $\chi^{(j)}$ is j^{th} order susceptibility. The linear susceptibility $\chi^{(1)}$ represents the dominant contribution to $\boldsymbol{P}$. The second-order susceptibility $\chi^{(2)}$ vanishes for silica glasses as the material SiO_2 used to fabricate optical fiber has molecular symmetry. Therefore, we focus on the third-order nonlinear effects $\chi^{(3)}$ which is further analyzed in two parts-the linear part $\boldsymbol{P}_L(\boldsymbol{r},\boldsymbol{t})$ and the nonlinear part $\boldsymbol{P}_{NL}(\boldsymbol{r},\boldsymbol{t})$:

$$\boldsymbol{P}(\boldsymbol{r},\boldsymbol{t}) = \boldsymbol{P}_L(\boldsymbol{r},\boldsymbol{t}) + \boldsymbol{P}_{NL}(\boldsymbol{r},\boldsymbol{t}) \tag{5.17}$$

Derivation of variance of phase noise

The variance of phase noise is derived. Considering additive white Gaussian noise, the retrieved DOFC signal with described DSP method can be expressed as:

$$E_s = \sum_{k=-N/2-1}^{N/2} (1+g_{v_k})e^{j\varphi_k} + \sigma$$

Where σ is the stand deviation of measurement noise in Brillouin gain spectrum. The phase profile recovered from the DOFC signal is also distorted by random noise, as shown in the following equation:

$$\varphi_k = Arg\left[(1+g_v)e^{j(\varphi_k)} + \sigma\right]$$

For convenience, let:

$$I = (1+g_v)e^{j(\varphi_k)} + \sigma$$

$$R = {}^{I_Q}\!/_{I_I} = {}^{\mathrm{Im}(I)}\!/_{\mathrm{Re}(I)}$$

$$= \frac{(1+g_v)\sin(\varphi_k)+\sigma_Q}{(1+g_v)\sin(\varphi_k)+\sigma_I}$$

$$\sigma = \sigma_I + j*\sigma_Q$$

The unbiased estimation of R is:

$$\bar{R} = \tan(\varphi_k)$$

While the variance of R is given in [103]:

$$D(R) = \bar{R}^2 \left[\frac{D(I_I)}{\bar{I}_I^{\,2}} + \frac{D(I_Q)}{\bar{I}_Q^{\,2}} - 2\frac{c(I_I, I_Q)}{I_I I_Q} \right]$$

Where I_I I_Q , represent for the In-phase and Quadrature component of I , $D(I)$, $D(Q)$, and $c(I,Q)$ denote variance of estimators of $\mathrm{var}(I)$, and $\mathrm{var}(Q)$, and $C\mathrm{ov}(I_I, I_Q)$ respectively.

The error of the estimation of phase profile is determined from the variance of φ_k .The anti-trigonometric function is expanded in the neighborhood of φ_k according to the Taylor's theorem [104]:

$$\varphi_{(k)} = \arctan(\bar{R}) + \arctan'(\bar{R})(R-\bar{R}) + L_2(R)$$

$L_2(R)$ Represents for the Lagrange remainder term. φ_k Can be approximated by (8) if we ignore the remainder term.

$$\varphi_{(k)} \approx \arctan(\bar{R}) + \arctan'(\bar{R})(R-\bar{R})$$

The variance of φ_k can be analyzed with:

$$D(\varphi_k) \approx \arctan'(\bar{R}^2) D(R)$$

Substitute formula (9) into equation (12), the following expression for the variance of phase noise can be obtained:

$$D(\varphi_k) = \frac{\bar{R}^2}{(1+\bar{R}^2)^2}\left(\frac{\sigma_I^2}{\bar{I}_I^2} + \frac{\sigma_Q^2}{\bar{I}_Q^2}\right)$$

$$= \frac{\sigma^2 \big/ 2}{1 + g^2}$$

Bibliography

[1] J. Hecht, City of Light: The Story of Fiber Optics, Oxford, New York 1999.

[2] K. C. Kao and G. A. Hockham, “Dielectric-fiber surface waveguides for optical frequencies,” Proc. Inst. Electr. Eng., vol. 133, no. 3, pp. 1151–1158, 1966.

[3] F. P. Kapron, D. B. Keck, and R. D. Mauer, “Radiation losses in glass optical waveguides,” Appl. Phys. Lett., vol. 17B, pp. 423–425, 1970.

[4] W. G. French, A. D. Pearson, G. W. Tasker, J. B. MacChesney, "A low-loss fused silica optical waveguide with boro-silicate cladding," Appl. Phys. Lett., vol. 23, pp. 338-339, 1973.

[5] T. Miya, Y. Terunuma, T. Hosaka, and T. Miyashita, “Ultimate low-loss single-mode fibre at 1.55 μm,” Electron. Lett., vol. 15, pp. 106–108, 1979.

[6] Debye, P., “Molecular-weight determination by light scattering,” J. Phys. Chem. , vol. 51, pp. 18–32, 1947.

[7] M. J. Damzen, V. Vlad, A. Mocofanescu, and V. Babin, “Stimulated Brillouin Scattering: Fundamentals and Applications.” (Taylor & Francis, 2010).

[8] W. Zou, X. Long and J.P. Chen “Advances in optical fiber technology,” Intech, 2015

[9] L. Brillouin, “Diffusion de la lumiere et des rayonnes X parun corps transparent homogene; influence del’agitation thermique,” Ann. Phys., vol. 17, pp. 88–122, 1922.

[10] Boyd, R.W. Nonlinear Optics, 3rd ed.; Academic Press: San Diego, CA, USA, 2008.

[11] Barnoski MK, Jensen SM. “Fiber waveguides: a novel technique for investigating attenuation characteristics,” Appl. Opt., vol. 15, pp. 2112-5, 1976.

[12] Palmieri, Luca, and L. Schenato, "Distributed Optical Fiber Sensing Based on Rayleigh Scattering," The Open Optics Journal, pp. 104, 2013.

[13] Barnoski, M.K.; Rourke, M.D.; Jensen, S.M.; Melville, R.T., “Optical time domain reflectometer,” Appl. Opt., vol.16, pp. 2375–2379, 1977.

[14] A. Kyoo Nam Choi, Juan Carlos Juarez, and Henry F. Taylor, "Distributed fiber-optic pressure/seismic sensor for low-cost monitoring of long perimeters," Proceeding of SP IE, vol. 5090, pp. 134 -14, 2003.

[15] JuanC.Juarez, EricW.Maier, Kyoo NamChoi, and Henry F. Taylor, "Distributed fiber-optic intrusion sensor system, " J. Lightwave Technology, vol. 23, pp. 2081-2087, 2005.

[16] Yuelan Lu, TaoZhu, LiangChen, and Xiaoyi Bao, "Distributed vibration sensor based on coherent detection of phase-OTDR, " J. Lightwave Technology, vol. 28, pp. 324, 2010.

[17] G. J. Tu, X. P. Zhang, Y. X. Zhang, F. Zhu, L. Xia, and B. Nakarmi, “The Development of an Φ-OTDR System for Quantitative Vibration Measurement,” IEEE Photonics Technol. Lett., vol. 27, pp.1349–1352, 2015.

[18] A. Masoudi, M. Belaland, and T. P. Newson, “A distributed optical fibre dynamic strain sensor based on phase-OTDR,” Meas. Sci. Technol. 24(8), 085204 (2013).

[19] G. S. Fang, T. W. Xu, S. W. Feng, and F. Li, “Phase-sensitive optical time domain reflectometer based on phase-generated carrier algorithm,” J. Lightwave Technol. 33(13), 2811–2816 (2015).

[20] J. Zhou, Z. Q. Pan, Q. Ye, H. W. Cai, R. H. Qu, and Z. J. Fang, “Phase demodulation technology using a multi-frequency source discrimination of interference-fading induced false alarm in a Φ-OTDR system,” Chin. J. Lasers, vol. 40, pp. 0905003, 2013.

[21] Z. Wang, L. Zhang, S. Wang, N. Xue, F. Peng, M. Fan, W. Sun, X. Qian, J. Rao, and Y. Rao, “Coherent Φ-OTDR based on I/Q demodulation and homodyne detection,”

Opt. Express, vol. 24, pp. 853–858, 2016.

[22] Y. Dong, X. Chen, E. Liu, C. Fu, H. Zhang, and Z. Lu, “Quantitative measurement of dynamic nanostrain based on a phase-sensitive optical time domain reflectometer,” Appl. Opt., vol. 55, pp. 7810–7815, 2016.

[23] Y. Muanenda, “Recent Advances in Distributed Acoustic Sensing Based on Phase-Sensitive Optical Time Domain Reflectometry,” J. Sens., vol. 2018, pp. 3897873, 2018.

[24] A. Masoudi, M. Beal, “A distributed optical fibre dynamic strain sensor based on phase-OTDR,” Meas. Sci. Technol., vol. 24, 2013.

[25] G. P. Agrawal, Fiber-Optic Communication Systems, USA, NY, New York: Wiley, pp. 156-158, 2002.

[26] H. F. Martins, S. Martin-Lopez, P. Corredera, M. L. Filograno, O. Frazao, M. Gonzalez-Herraez, "Coherent noise reduction in high visibility phase sensitive optical time domain reflectometer for distributed sensing of ultrasonic waves", J. Lightw. Technol., vol. 31, no. 23, pp. 3631-3637, 2013.

[27] V. I. Bespalov, V. I. Talanov, "Filamentary structure of light beams in nonlinear liquids", JETP Lett., vol. 3, pp. 307-310, 1966.

[28] V. I. Karpman, “Self-modulation of Nonlinear Plane Waves in Dispersive Media,” JETP Lett., vol. 6, pp. 277–279, 1967.

[29] S. M. Foaleng and L. Thévenaz, “Impact of Raman scattering and modulation instability on the performances of Brillouin sensors,” in 21st International Conference on Optical Fiber Sensors, pp. 77539V-77539V, 2011.

[30] Gabai, H., and Eyal, A., “On the sensitivity of distributed acoustic sensing,” Optics Letters, 2016.

[31] H. Gabai and A. Eyal, “How to specify and measure sensitivity in distributed acoustic

sensing (DAS)?," in 25th International Conference on Optical Fiber Sensors, pp. 1–4, Jeju Island, Republic of Korea, 2017.

[32] Horiguchi, T.; Kurashima, T.; Tateda, M. Tensile strain dependence of Brillouin frequency shift in silica optical fibers. IEEE Photonics Technol. Lett., vol.1, pp. 107–108, 1989,

[33] Kurashima T, Horiguchi T, Izumita H, Furukawa S and Koyamada Y "Brillouin optical-fber time domain reflectometry" IEICE Trans. Commun. E76-B 382–90.

[34] S.M. Maughan, H.H. Kee and T.P. Newson, "Simultaneous distributed fibre temperature and strain sensor using microwave coherent detection of spontaneous Brillouin backscatter," Meas. Sci. Technol., vol. 12, pp. 834-842, 2001.

[35] Y. Koyamada, Y. Sakairi, N. Takeuchi, and S. Adachi, "Novel technique to improve spatial resolution in Brillouin optical time-domain reflectometry," IEEE Photon. Technol. Lett., vol. 19, pp. 1910-1912, 2007.

[36] J. Geng, S. Staines, M. Blake, et al., "Distributed fiber temperature and strain sensor using coherent radiofrequency detection of spontaneous Brillouin scattering," Applied Optics, vol. 46, pp. 5928-5932, 2007.

[37] Horiguchi, T.; Tateda, M. "Optical-fiber-attenuation investigation using stimulated Brillouin scattering between a pulse and a continuous wave," Opt. Lett., vol. 14, pp. 408-410, 1989.

[38] Tateda, M.; Horiguchi, T.; Kurashima, T.; Ishihara, K., "First measurement of strain distribution along field-installed optical fibers using Brillouin spectroscopy," J. Lightwave Technol., vol. 8, pp. 1269-1273, 1990.

[39] Horiguchi, T.; Kurashima, T.; Tateda, M. "Tensile strain dependence of Brillouin frequency shift in silica optical fibers," IEEE Photonic. Technol. Lett., vol. 1, pp. 107-108, 1989.

[40] Horiguchi, T.; Kurashima, T.; Tateda, M.; Ishihara, K.; Wakui, Y., “Brillouin characterization of optical fiber strain in bent slot-type optical-fiber cable,” J. Lightwave Technol., vol. 10, pp. 1196-1201, 1992.

[41] Culverhouse, D.; Farahi, F.; Pannell, C.N.; Jackson, D.A., “Potential of stimulated Brillouin scattering as sensing mechanism for distributed temperature sensors,” Electron. Lett., vol. 25, pp. 913-915, 1989.

[42] Kurashima, T.; Horiguchi, T.; Tateda, “M. Distributed-temperature sensing using stimulated Brillouin scattering in optical silica fibers,” Opt. Lett., vol. 15, pp. 1038-1040, 1990.

[43] Bao, X.; Webb, D.J.; Jackson, D.A., “22-km distributed temperature sensor using Brillouin gain in an optical fiber,” Opt. Lett., vol. 18, pp. 552-554, 1993.

[44] M. A. Soto and L. Thévenaz, “Modeling and evaluating the performance of Brillouin distributed optical fiber sensors,” Opt. Express, vol. 21, pp. 31347–31366, 2013.

[45] K. Hotate, and T. Hasegawa, “Measurement of Brillouin gain spectrum distribution along an optical fiber using a correlation-based technique -proposal, experiment and simulation,” IEICE Trans. Electronics, vol. E83-C, pp. 405-412, 2000.

[46] Y. Mizuno, W. Zou, Z. He, and K. Hotate, "Proposal of Brillouin optical correlationdomain reflectometry (BOCDR)," Optics Express, vol. 16, pp.12148-12153, 2008.

[47] M. Niklès, L. Thévenaz, and P. A. Robert, “Simple distributed fiber sensor based on Brillouin gain spectrum analysis,” Optics Lett., vol. 21, pp. 758-760, 1996.

[48] A. Dominguez-Lopez, X. Angulo-Vinuesa, A. Lopez-Gil, S. Martin-Lopez, and M. Gonzalez-Herraez, “Non-local effects in dual-probe-sideband Brillouin optical time domain analysis,” Opt. Express, vol. 23, pp. 10341–10352, 2015.

[49] K. Shimizu, T. Horiguchi, and Y. Koyamada, “Measurement of distributed strain and

temperature in a branched optical fiber network by use of Brillouin optical time domain reflectometry," Optics Lett., vol. 20, pp. 507-509, 1995.

[50] H. G. Shiraz and T. Okashi, "Fault Location in Optical Fibers Using Optical Frequency Domain Reflectometry," J. of Lightwave Technology, vol. LT-4, pp. 316-322, 1986.

[51] D. Garus, K. Krebber, F. Schliep, and T. Gogolla, "Distributed sensing technique based on Brillouin Optical-fiber Frequency-domain analysis," Optics Lett., vol. 21, pp. 1402-1404, 1996.

[52] S. M. Foaleng and L. Thévenaz, "Impact of Raman scattering and modulation instability on the performances of Brillouin sensors," in 21st International Conference on Optical Fiber Sensors, 77539V-77539V, May 2011

[53] Y. Peled, A. Motil, and M. Tur, "Fast Brillouin optical time domain analysis for dynamic sensing," Opt. Express, vol. 20, pp. 8584–8591, 2012.

[54] Cisco Visual Networking Index: Forecast and Methodology, 2016–2021 (Cisco, September 2017);

[55] Damage to Telecommunication Cables - Infocomm Media Development Authority. [online] Available at: https://www.imda.gov.sg/regulations-licensing-and-consultations/frameworks-and-policies/competition-management/enforcement-decisions/damage-to-telecommunication-cables [Accessed 21 Mar. 2019].

[56] Ultra-map.org. (2019). 70% of subsea cable damage can be prevented. [online] Available at: http://www.ultra-map.org/news/the-various-threats-to-subsea-cables [Accessed 21 Mar. 2019].

[57] A. Masoudi and T. Newson, "Contributed review: Distributed optical fiber dynamic strain sensing," Rev. Sci. Instrum., vol. 87, 2016.

[58] D. P. Zhou, Z. Qin, W. Li, L. Chen, and X. Bao, "Distributed vibration sensing with

time-resolved optical frequency-domain reflectometry," Opt. Express, vol. 20, pp. 13138–13145, 2012.

[59] Y. Lu, T. Zhu, L. Chen, and X. Bao, "Distributed vibration sensor based on coherent detection of phase-OTDR," J. Lightw. Technol., vol. 28, pp. 3243–3249, 2010.

[60] C. A. Galindez-Jamioy and J. M. Lopez-Higuera, "Brillouin Distributed Fiber Sensors: An Overview and Applications," J. of Sensors, vol. 17, pp. 204121, 2012.

[61] A. E. Alekseev, V. S. Vdovenko, B. G. Gorshkov, V. T. Potapov, and D. E. Simikin, "A phase-sensitive optical time-domain reflectometer with dual-pulse diverse frequency probe signal," Laser Phys., vol. 25, pp. 065101, 2015.

[62] B. Luet al., "High spatial resolution phase-sensitive optical time domain reflectometer with a frequency-swept pulse," Opt. Lett., vol. 42, no. 3, pp. 391–394, 2017.

[63] F. Peng, H. Wu, X. H. Jia, Y. J. Rao, Z. N. Wang, and Z. P. Peng, "Ultra-long high-sensitivity Φ-OTDR for high spatial resolution intrusion detection of pipelines," Opt. Express, vol. 22, pp. 13804–13810, 2014.

[64] J. Armstrong and A. J. Lowery, "Power efficient optical OFDM," Electron. Lett., vol. 42, pp. 370–371, 2006.

[65] J. Armstrong, "OFDM for optical communications," J. Ligthw. Technol., vol. 27, pp. 189-204, 2009.

[66] Z. Wang, L. Zhang, S. Wang, N. Xue, F. Peng, M. Fan, W. Sun, X. Qian, J. Rao, and Y. Rao, "Coherent Φ-OTDR based on I/Q demodulation and homodyne detection," Opt. Express, vol. 24, pp. 853–858, 2016.

[67] X. Yi, W. Shieh, and Y. Tang, "Phase Estimation for Coherent Optical OFDM," IEEE Photon. Technol. Lett., vol. 19, pp. 919 – 921, 2007.

[68] W. Shieh, H. Bao, and Y. Tang, "Coherent optical OFDM: theory and design," Opt.

Express, vol. 16, pp. 841–859, 2008.

[69] L. Thevenaz, M. Nikles, A. Fellay, M. Facchini, and P. A. Robert, "Truly distributed strain and temperature sensing using embedded optical fibers," Proc. SPIE., vol. 3330, pp. 301-304, 1998.

[70] X. Bao, M. DeMerchant, A. Brown, and T. Bremner, "Tensile and compressive strain measurement in the lab and field with the distributed Brillouin scattering sensor," J. Lightwave Technol., vol. 19, pp. 1698-1704, 2001.

[71] R. Bernini, A. Minardo, and L. Zeni, "Dynamic strain measurement in optical fibers by stimulated Brillouin scattering," Opt. Lett., vol. 34, pp. 2613-2615, 2009.

[72] Y. Peled, Avi Motil, Lior Yaron, and Moshe Tur, ”Slope-assisted fast distributed sensing in optical fibers with arbitrary Brillouin profile,” Opt. Express, vol. 19, pp. 19845-19854, 2011.

[73] Y. Peled, Avi Motil, Iddo Kressel, and Moshe Tur, “Monitoring the propagation of mechanical waves using an optical fiber distributed and dynamic strain sensor based on BOTDA,” Opt. Express, 21, pp. 10697-10705, 2013.

[74] A. Voskoboinik, W. Jian, B. Shamee, S. R. Nuccio, L. Zhang, M. Chitgarha, A. E. Willner, and M. Tur, "SBS-Based Fiber Optical Sensing Using Frequency-Domain Simultaneous Tone Interrogation," J. Lightwave Technol., vol. 29, pp. 1729-1735, 2011.

[75] A. Voskoboinik, O. F. Yilmaz, A. W. Willner, and M. Tur, "Sweep-free distributed Brillouin time-domain analyzer (SF-BOTDA)," Opt. Express, vol.19, pp. B842-B847, 2011.

[76] A. Voskoboinik, D. Rogawski,H. Huang, Y. Peled, A. E. Willner, and M. Tur “Frequency-domain analysis of dynamically applied strain using sweep-free Brillouin time domain analyzer and sloped-assisted FBG sensing” Opt. Express, vol.

20, pp. B581-B586, 2012.

[77] Y.Peled, A.Motil, M.Tur, “F ast Brillouin optical time domain analysis for dynamic sensing, “Opt. Express, vol. 20, pp. 8584-8591, 2012.

[78] Sovran, A.Motil, M.Tur, M.Sovran, I.Motil, A.Tur, “Frequency-scanning botda with ultimately fast acquisition speed,” Photon. Technol .Lett., vol. 27, pp. 1426–1429, 2015.

[79] I. Sovran, A. Motil, O. Danon, and M. Tur, “An ultimately fast frequency-scanning Brillouin optical time domain analyzer,” in Proc. Opt. Fiber Commun. Conf., (Los Angeles, CA, USA, 2015), paper W2A.44.

[80] X. Bao and L. Chen, “Recent progress in optical fiber sensors based on Brillouin scattering at university of Ottawa,” Photon. Sensors, vol. 1, pp. 102–117, 2011.

[81] X. Yi, Z. Li, Y. Bao, and K. Qiu, "Characterization of Passive Optical Components by DSP-Based Optical Channel Estimation," IEEE Photon Technol. Lett., vol. 24, pp. 443-445, 2012.

[82] C. Jin, Y. Bao, Z. Li, T. Gui, H. Shang, X. Feng, J. Li, X. Yi, C. Yu, G. Li, and C. Lu, "High-resolution optical spectrum characterization using optical channel estimation and spectrum stitching technique," Opt. Lett., vol. 38, pp. 2314-2316, 2013.

[83] T. Horiguchi and M. Tateda, "Optical-fiber-attenuation investigation using stimulated Brillouin scattering between a pulse and a continuous wave," Opt. Lett., vol. 14, pp. 408, 1989.

[84] T. Horiguchi, T. Kurashima and M. Tateda, " Tensile strain dependence of Brillouin frequency shift in silica optical fibers," IEEE Photon. Technol. Lett., vol. 1, pp. 107, 1989.

[85] Y. Mizuno, N. Hayashi, H. Fukuda, K. Y. Song, and K. Nakamura, “Ultra high speed distributed Brillouin reflectometry,” Light: Sci. Appl., vol. 5, pp. e16184, 2016.

[86] E. Preter, D. Ba, Y. London, O. Shlomi, Y. Antman, and A. Zadok, "High resolution Brillouin optical correlation domain analysis with no spectral scanning," Opt. Express, vol. 24, pp. 27253, 2016.

[87] J. Fang, W. Shieh, and P. Xu, “Single-shot Brillouin optical time domain analysis for distributed fiber sensing,” Proc. IEEE Sensors, pp. 1-4, 2016.

[88] X. Bao and L. Chen, "Recent progress in optical fiber sensors based on Brillouin scattering at university of Ottawa," Photon. Sensors., vol. 1, pp. 102, 2011.

[89] T. Sperber, A. Eyal, M. Tur, and L. Thévenaz, "High spatial resolution distributed sensing in optical fibers by Brillouin gain-profile tracing," Opt. Express, vol. 18, pp. 8671, 2010.

[90] M. A. Soto, G. Bolognini, and F. Di Pasquale, “Optimization of long-range BOTDA sensors with high resolution using first-order bi-directional Raman amplification,” Opt. Express, vol. 19, pp. 4444, 2011.

[91] X. Tu, Q. Sun, W. Chen, M. Chen, and Z. Meng, “Vector Brillouin optical time-domain analysis with heterodyne detection and IQ demodulation algorithm,” IEEE Photon. J., vol. 6, pp. 1, 2014.

[92] X. Angulo-Vinuesa, A. Lopez-Gil, A. Dominguez-Lopez, J. L. Cruz, M. V. Andres, S. Martin-Lopez, and M. Gonzalez-Herraez, “Simultaneous gain and phase profile determination on an interferometric BOTDA,” Proc. SPIE 9634, pp. 963419, 2015.

[93] Z. Li, L. Yan, L. Shao, W. Pan, and B. Luo, “Coherent BOTDA sensor with intensity modulated local light and IQ demodulation,” Opt. Express, vol. 24, pp. 235040, 2015.

[94] A. Lopez-Gil, X.Angulo-Vinuesa, M. A. Soto, A. Dominguez-Lopez, S. Martin-Lopez, L. Thévenaz, and M. Gonzalez-Herraez, “Gain vs phase in BOTDA setups,” Proc. SPIE, vol. 9916, pp. 991631, 2016.

[95] A. Lopez-Gil, M. A. Soto, X. Angulo-Vinuesa, A. Dominguez-Lopez, S. Martin-

Lopez, L. Thévenaz, and M. Gonzalez-Herraez, "Evaluation of the accuracy of BOTDA systems based on the phase spectral response," Opt. Express, vol. 24, pp. 17200, 2016.

[96] J. Urricelqui, A. Zorrnoza, M. Sagues and A. Loayssa, "Dynamic BOTDA measurements based on Brillouin phase-shift and RF demodulation," Opt. Express, vol. 20, pp. 26942, 2012.

[97] S. Díaz, S. M. Foaleng, M. López-Amo and L. Thévenaz, "High performance Brillouin distributed fibre sensor," Proc. SPIE, vol. 6619, pp.661938, 2007.

[98] J. Yang, C. Yu, Z. Chen, J. Ng and X. Yang, "Suppression of polarization sensitivity in BOTDA fiber distributed sensing system"Proc. SPIE, vol. 7004, pp. 700421, 2008.

[99] J. Urricelqui, F. López-Fernandino, M. Sagues and A. Loayssa,"Polarization diversity for Brillouin distributed fiber sensors based on a double orthogonal pump," Proc. SPIE, vol. 9157, pp. 91576A, 2014.

[100] J. Urricelqui, F. López-Fernandino, M. Sagues and A. Loayssa,"Polarization diversity scheme for BOTDA sensors based on a double orthogonal pump interaction," J. Lightwave Technol., vol. 33, pp. 2633, 2015.

[101] G. Agrawal, "Nonlinear Fiber Optics," 5th ed. Academic press, 2013.

[102] P. Diament, Wave Transmission and Fiber Optics (Macmillan, New York, 1990), Chap. 3.

[103] K. M. Wolter, introduction to variance estimation (Springer Science+Business Media, 2007), Chap. 6.

[104] Songlin. Z and Kun. Z, "Approximate computation of expectation and variance of nonlinear function of continuous random variable," J. Geodesy and Geodyn 28, 107 (2008).